EXPERIMENTAL AND NUMERICAL STUDY OF THE QUASI-STATIC BEHAVIOR OF Ti–6Al–4V

by

VÍCTOR TUNINETTI VASQUEZ

A thesis submitted to the ArGEnCo department in conformity with the requirements for the degree of Doctor in Engineering Sciences

Université de Liège

Liège, Belgium

April 2014

Acknowledgments

The main acknowledgments are addressed to Dr. Anne–Marie Habraken. During my time working in the MS^2F team, she has not only guided me and assessed my work critically for the excellence but also she encouraged me to accomplish all of the goals of this thesis.

I'm very grateful to my colleagues and friends of the MSM and M&S team, especially to O. Millis for his invaluable support and practical help.

I would also like to thanks to my co–workers in the appended papers: Dr. Thomas Pardoen at the IMAP UCL and Gaëtan Gilles for their collaboration.

Thanks also to the Walloon Region for the financial support.

A special thanks to all my friends in Liege, I'll always remember the great times we spent together ;)

Finally, I would like to express my deepest gratitude to my precious family and girlfriend Ling–Li for their love and unconditional support.

Vita

2014……	PhD Engineering Sciences, University of Liège, Belgium
2010……	Master of Science in Mechanical Engineering, University of Concepción, Chili
2009……	Civil Aerospace Engineer, University of Concepción, Chili
2006……	Bachelor of Engineering Sciences, University of Concepción, Chili
2003……	Liceo Los Ángeles A–59, Chili
1998……	Escuela D–934 Thomas Jefferson, Chili

Publications

Tuninetti, V., Habraken, A.M., (2014). *Impact of anisotropy and viscosity to model the mechanical behavior of Ti–6Al–4V alloy*. Materials Science and Engineering: A, 605, 39–50, (ISI).

Tuninetti, V., Gilles, G., Milis, O., Pardoen, T., Habraken, A.M. (under–revision). *Anisotropy and tension–compression asymmetry predictions of the plastic response of bulk Ti–6Al–4V alloy*. Submitted to International Journal of Plasticity, (ISI).

Tuninetti, V., Gilles, G., Milis, O., Neira, I., Habraken, A.M., 2013. *Quasi–static mechanical behaviour of Ti–6Al–4V alloy at room Temperature*. Proceedings of the XII International Conference on Computational Plasticity – Fundamentals and Applications, 51–62. Barcelona, Spain, (ISI).

Duchêne, L., ben Bettaieb, A., Tuninetti, V., Habraken, A.M., 2013. *Numerical modeling and digital image correlation strain measurements of*

coated metal sheets submitted to large bending deformation. Procedia 16th ESAFORM, (Peer reviewed).

Tuninetti, V., Gilles, G., Milis, O., Lecarme, L., Habraken, A.M., 2012. *Compression test for plastic anisotropy characterization using optical full–field displacement measurement technique*. Steel Research International. SE: 14th Int. Conf. Metal Forming 2012, 1239–1242. (ISI).

Tuninetti, V., Gilles, G., Péron–Lührs, V. Habraken, A.M., 2012. *Compression test for metal characterization using Digital Image Correlation and Inverse Modeling*, Procedia IUTAM. 4, 206–214. (Scopus)

Ben Bettaieb, A., Tuninetti, V., Duchêne, L., 2012. *Numerical simulation of T–bend of multilayer coated metal sheet using solid–shell element*. Steel Res. Int. SE: 14th Int. Conf. Metal Forming 2012, 1311–1314. (ISI).

Gilles, G., Tuninetti, V., ben Bettaieb, M., Cazacu, O., Habraken, A.M., Duchêne, L., 2011. *Experimental characterization and constitutive modeling of TA6V mechanical behavior in plane strain state at room temperature*. AIP Conf. Proc. 1383, 78–85. (Peer reviewed).

Flores, P., Tuninetti, V., Gilles, G., Gonry, P., Duchêne, L., Habraken, A.M., 2010. *Accurate stress computation in plane strain tensile tests for sheet metal using experimental data*. J. Mater. Process. Technol. 210, 1772–1779. (ISI).

Attended Conferences

– Complas XII 2013, Barcelona, Spain.
– Metal Forming 2012, Krakow, Poland.
– IUTAM Symposium 2011 (LMT), Paris (Cachan), France.
– Photomechanics 2011, Brussels, Belgium.
– IAP P6/24 meeting 2012, Antwerp, Belgium.
– IAP P6/24 meeting 2010, Blankenberge, Belgium.
– IAP P6/24 meeting 2009, Liège, Belgium.

Abstract

This thesis deals with the accurate experimental identification and modeling of the mechanical behavior of the Ti–6Al–4V alloy under multiple loading and temperature conditions. First, the experimental developments required for the proper calibration of the models are presented. A new tool is implemented in the universal testing machines in order to perform tests at a constant strain rate. This tool is essential for this study as the yield stress of the Ti–6Al–4V is strain rate sensitive. Another essential tool that is widely used to measure the full–field displacement/strain of objects is the digital image correlation (DIC). In this thesis, the 3D–DIC Limess–VIC3D system is set–up for very accurate measurements of all the experimental tests at room temperature. The main difficulties and solutions found in the handling of the 3D–DIC system are given. Besides, a reliable tool is implemented in order to post–process the data obtained with multiple 3D–DIC systems, including an improved methodology to accurately determine the evolution of the cross–section, the strain field and the true stress – true strain curves of cylindrical specimens.

A new compression test on an elliptical cross–section specimen is proposed for inverse identification of the plastic anisotropy of the alloy using DIC. The performed numerical simulations of the compression test on this new specimen show that inhomogeneous axial strain distribution is sensitive to the plastic anisotropy of the material. This observation justifies the use of the inverse modeling of this compression test for the identification of the plastic anisotropy of the alloy.

The mechanical behavior of the Ti–6Al–4V alloy is experimentally investigated at room temperature by using compression, tension, simple shear and plane strain tests performed in the three orthogonal directions of the material. In addition, the evolution of the tensile and compressive behavior with the temperature and strain rate in one direction of the material is also presented. Two approaches to plasticity models are considered in order to capture the experimentally observed features of the alloy:

Abstract

- The plastic anisotropy and strength differential effect are well captured by the CPB06 orthotropic yield criterion at three identification temperatures (RT, 150 °C and 400 °C), at one strain rate (equal to 10^{-3} s^{-1}) and at the three orthogonal directions of the material. The main advantage of this model is that it uses directional hardening and tension/compression asymmetry yielding. However, this elasto-plastic version neglects the viscosity effects observed on the behavior of the alloy.

- The second approach is a thermo–elasto–viscoplastic model which is identified by using tensile tests performed at several constant strain rates and at temperatures up to 400 °C. Here, the viscosity effects are well captured by the Norton–Hoff constitutive model. However, the yield surface of this approach is described by the von Mises criterion which neglects the observed anisotropy response of the alloy.

The two approaches are assessed. The load and shape predictions of the identified Norton–Hoff and CPB06 models are compared with experimental results obtained on tensile tests on round bars with various u–notch, v–notch, and central hole as well as on compression tests at several temperatures and strain rates. This evaluation of errors allows concluding that even though the strain rate hardening behavior is well predicted by the Norton–Hoff model, the anisotropy and SD effects seems to be more pronounced than the former. Therefore, the CPB06 model leads to lower errors than those produced by the Norton–Hoff model.

Finally, this comprehensive research with the main results and conclusions presented in this thesis are essential information that should be considered for designers and manufacturers of components and parts of the Ti–6Al–4V alloy. A further development of an advanced model is suggested as future work in order to increase even more the FE–modeling predictions of the Ti–6Al–4V. This model could account all together the observed features of the alloy: plastic anisotropy, strength differential effect, kinematic hardening, strain rate hardening and damage.

Symbols and Abbreviations

Abbreviations

BAU	Bauschinger test
bcc	crystal structure that contains an atom in the center and one atom in each corner of a cube
BLZ3T	thermomechanical mixed solid finite element in Lagamine code
Br	Bauschinger ratio
BWD3D	8–node 3D brick element in Lagamine code
CCD	Charge–Coupled Device
CFI3D	3D contact elements
COMP	compression
CPB06	yield criterion proposed by Cazacu et al., 2006
DIC	Digital Image Correlation
EDM	wire Electron Discharge Machining
exp	experimental
exp()	Exponential function
FBO	Fan Blade Out test
FE	Finite Element
FEA	Finite Element Analysis
FEM	Finite Element Method
hcp	crystal structure that contains a collection of atoms that are closely packed into the shape of a hexagon
JC	Johnson–Cook viscoplastic model (Johnson and Cook, 1983)
KHL	Khan–Huang–Liang model (Khan et al., 2004)
LD	Longitudinal Direction
MSE	Weighted Mean Square Error

Symbols and Abbreviations

MTS	Mechanical Threshold Strength model
NH	Norton–Hoff model (Norton, 1929)
num	numerical
Ra	Roughness average
RT	Room Temperature
SD	Strength Differential effect (strength asymmetry between tension and compression)
SPS	Simple Plane Strain
SSH	Simple Shear
ST	Short Transverse direction
TD	Transverse Direction
TENS	Tensile
Ti	Titanium
Ti–64	Titanium alloy 6% Aluminum and 4% Vanadium
TA6V	Titanium alloy 6% Aluminum and 4% Vanadium
Ti–6Al–4V	Titanium alloy 6% Aluminum and 4% Vanadium
VM	von Mises
Za	Zerilli–Armstrong model

Latin Characters

a	major axis length of the current elliptical cross–section of the specimen
A	actual area
	initial yield strength coefficient of JC model
A_0	material parameter related to initial yield stress of the Voce hardening law
	initial cross–section of the specimen
b	minor axis length of the current elliptical cross–section of the specimen
B	strain hardening coefficient of JC model
B_0	material parameter of the Voce hardening law
C	strain rate hardening coefficient of JC model

$\mathbf{C}$	fourth–order orthotropic tensor that accounts for the plastic anisotropy of the material*
C_{ij}	anisotropy coefficients in CPB06 yield criterion
C_0	material parameter of the Voce hardening law
E	Young's Modulus
	Error function
F	axial load
F_1	yield function
H_0	initial height of the specimen
N	strain hardening exponent of JC model
P_1	NH parameter related to softening
P_2	NH parameter related to strength
P_3	NH parameter related to viscosity
P_4	NH parameter related to hardening
R	Notch radius
r_0	initial circular radius of the specimen
R_{LD}	parameter similar to the "Lankford" coefficient defined as the ratio of the strain rates in the TD direction and in the ST direction
$\mathbf{S}$	deviator of the second-order Cauchy stress tensor*
t	time
T	temperature
v	speed of the cross–head of the testing machine
W_p	plastic work per unit volume
x	cartesian coordinate
$X_{ep}(t)$	reduction of the height of the specimen
$X_{ma}(t)$	deflection of the testing machine
y	cartesian coordinate
z	cartesian coordinate

* Tensors are written with bold letters

Symbols and Abbreviations

Greek Characters

α	hcp phase of TA6V
β	bcc phase of TA6V
γ	shear strain
$\Delta r_{systemi}$	variation of the radius measured by DIC system i
ε	strain
$\dot{\varepsilon}$	strain rate
ε_p	plastic strain
$\bar{\varepsilon}_p$	equivalent plastic strain
$\dot{\bar{\varepsilon}}$	equivalent strain rate
$\bar{\varepsilon}$	equivalent total strain
$\dot{\boldsymbol{\varepsilon}}^{vp}$	viscoplastic strain tensor
η	weight parameter of the error function
θ	angle with respect to the major axis direction of the ellipse
$\boldsymbol{\sigma}$	stress tensor
σ_F	yield stress at the start of unloading in a Bauschinger test
σ_R	yield stress at the reverse loading in a Bauschinger test
$\bar{\sigma}$	equivalent stress
σ_y	yield stress (Cauchy)
σ_0	initial yield strength
Σ_i	principal values of the tensor $\boldsymbol{\Sigma}$, defined as $\boldsymbol{\Sigma} = \mathbf{C} : \mathbf{S}$ in Cazacu model
τ	shear stress
ϕ	Coulomb friction coefficient

Table of Contents

Table of Contents

List of appendices

EXPERIMENTAL AND NUMERICAL STUDY OF THE QUASI-STATIC BEHAVIOR OF Ti–6Al–4V

Chapter 1. Introduction

In engineering applications, titanium (Ti) and its alloys have replaced other alloys owing to superior strength to density ratio, giving reliable, economic and more sustainable systems and components. The most commonly used and relatively economical Ti alloy is the Ti–6Al–4V (TA6V). This two phase $\alpha+\beta$–type alloy is found in many applications principally in the aerospace industry such as fasteners, aircraft structural and engine components because of its high strength over density ratio at low to moderate operating temperatures. Offshore petroleum industry has also taken advantages of using TA6V, for instance, in applications as drilling risers because of its high flexibility (low modulus), excellent corrosion and fatigue resistance (Deyuan et al., 2001, Gurrappa, 2003, Lütjering and Williams, 2007). These high mechanical performances combined with a good biocompatibility, are the reasons for the use of TA6V in the medical industry such as orthopedic and dental implants (Elias et al., 2008, Long and Rack, 2006, Rack and Qazi, 2006). The high strength to weight ratio and its good ballistic capability have attracted the interest of the defense industry for its use in armor for military vehicles (Burkings et al., 2000, 2001, Montgomery and Wells, 2001, Sukumar et al., 2013). The wide range of applications of TA6V alloy is the main motivation to understand and to model its mechanical behavior.

1.1. Motivation and context of the thesis

For manufacturers, reliable finite elements (FE) simulations of forming processes and components in operation conditions of TA6V alloy are highly relevant, if not essential. The reliability of the simulations depends on constitutive laws capable of accurately predicting the mechanical behavior of the alloy. Moreover, these constitutive laws require a proper calibration of material parameters which depends on the mechanical tests and the identification procedures.

1.1. Motivation and context of the thesis

This thesis is developed in the context of the Walloon Region project Winnomat 2 FABULOUS. Two industrial partners and three academic research units are involved in this project:

1. Techspace Aero (Safran group),
2. GDTech Engineering,
3. Institute of Materials, Mechanics and Civil Engineering (iMMC) from Université catholique de Louvain,
4. Department of Aerospace and Mechanical Engineering (LTAS) from University of Liege, and
5. MS^2F division – Structures, Fluids and Solid Mechanics of the ArGEnCO department from University of Liege.

The main aim of the project is to reduce 10% of the mass of the outer ring (engine casing) in a low pressure compressor of an aircraft engine manufactured by Techspace Aero. In order to certificate the resistance of the full engine, a fan blade out (FBO) test should be carried out. This test involves the failure of a whole blade at the root with the engine running at full speed. The blades impact the outer ring and the imminent explosion takes place. No fragment due to the explosion must be ejected to the fuselage and the wings to guarantee the safety of the passengers. In other words, the outer ring must be capable of resisting the internal explosion, ensuring that the structural integrity of the aircraft is maintained. Trial and error design method for the dimensioning of the engine parts is costly and time consuming. A cost effective alternative for the design is the FE analysis, which is applied in order to determine both, the maximum impact load during the FBO test and the final dimensions of the outer ring. As the outer ring and the compressor blades are made out of TA6V alloy, accurate FE prediction of the mechanical behavior of the alloy is essential.

1.2. State of the art – TA6V models

The primary phase α in TA6V is a hexagonal closed packed (hcp) structure. As for other hcp alloys, the flow stress is strongly dependent on both temperature and strain rate (Khan et al., 2004, 2007, Lee and Lin, 1998, Majorell et al., 2002, Peirs et al., 2010, Tuninetti et al., 2012b). Many different constitutive models are currently available to describe the strain

hardening, strain–rate hardening, and thermal softening of materials with specific material constants. Two categories can be distinguished: in the first category there are the physically based models, which consist in models that account for the deformation mechanism on the scale of dislocations, e.g., Mechanical Threshold Strength (MTS) model (Follansbee and Kocks, 1988), Zerilli–Armstrong (Za) model (Zerilli and Armstrong, 1987), etc., and in the second category, there are the purely phenomenological models, e.g., Johnson–Cook (JC) (Johnson and Cook, 1983), Norton–Hoff (NH) (Norton, 1929), Khan–Huang–Liang (KHL) (Khan et al., 2004) models, etc.

In addition to strain rate and temperature dependence, experimental results published by several researchers (Khan et al., 2012a, 2012b, Hammami et al., 2011, Gilles et al., 2011, Tuninetti et al., 2012b, Odenberger et al., 2012) show that TA6V also exhibits a strength differential (SD) effect, and distortion of the yield surface with the accumulated plastic deformation. Plunkett et al. 2006 explains that because of twinning and texture evolution, the yield surface for hexagonal close–packed (hcp) metals significantly changes shape with the accumulated plastic deformation and therefore traditional hardening laws cannot accurately model this phenomenon. The above mentioned features which are the anisotropy due to the texture evolution and the SD effect are captured by the macroscopic orthotropic yield criterion CPB06 proposed by Cazacu et al., 2006.

Many of the previous studies on quasi–static mechanical behavior of TA6V focus on identifying constitutive models that capture the SD effect and the anisotropy (Hammami et al., 2011, Gilles et al., 2011, Khan et al., 2012a, 2012b), other works focus on capturing the softening, workability and work hardening of TA6V in one loading direction (e.g. in compression: Lee and Lin, 1998, Khan et al., 2004; in tensile: Vanderhasten et al., 2008, ZHANG et al., 2012) and the validation of the models is essentially based on true stress–strain curve prediction of monotonic tests.

Some authors have focused on damage prediction of TA6V assuming an isotropic behavior but unfortunately with a mitigated success. For instance Peirs, 2012 has investigated the fracture prediction of TA6V using either a Johnson–Cook damage initiation criterion combined with a progressive isotropic damage law or the Gurson model. Lecarme, 2013 exactly focused on the same material as the one studied in this thesis (same batch) and

developed her own ductile damage model based. First, the Gologanu model for void growth and two versions of the Thomason criterion for coalescence were used, coupled to a Kocks–Mecking type hardening law.

1.3. Aims and objectives of the thesis

The aim of this thesis is to identify the mechanical behavior of a bulk TA6V alloy under multiple loading and temperature conditions (SD effect, anisotropy, work hardening, strain rate hardening). The main objectives are the following ones:

1. The development of the experimental tests with digital image correlation and the procedures needed to accurately identify the mechanical behavior of the TA6V alloy.

2. The generation of a comprehensive set of experimental data on TA6V.

3. The identification of the constitutive laws able to capture the observed mechanical behavior of the alloy.

4. The validations of these laws based on the verification of the accuracy of the FE simulations to reproduce the load and the evolution of strain/displacement fields on specimens subjected to multiaxial loadings and large plastic strains.

1.4. Contributions of the thesis

The main developments and original contributions obtained in this thesis applied to material characterization and mechanical behavior of TA6V are listed:

1. Development of a new compression test on an elliptical cross–section specimen for the inverse identification of the plastic anisotropy. The numerical results of compression tests presented in the Chapter 3 reveal a sensitivity of the axial strain field to the plastic anisotropy of the material. This key information was

essential for the implementation of an inverse method for the calibration of the material parameters. However, accurate measurements of the strain field are required for the proper calibration. The digital image correlation (DIC) is selected for this purpose, thus, the development of an experimental procedure with this new technique was necessary.

2. DIC set–up for the measurements of displacement fields on compression and tensile specimens. A step by step experimental procedure was developed in order to accurately measure the evolution of the geometry and the strain field of the compression and tension specimens by using 6 CCD–Cameras. A high expertise and a meticulous work were needed in order to achieve accurate results. For this reason, an in–depth study was performed regarding the requirements of the dimensions and the tolerances of the specimens, speckle size of the patterns, brightness and viscosity of the paint, optimum positions of the cameras, calibration procedures, lighting of the specimens, frequency of the acquisition of the images, optimum size of the subset for the correlation, etc.

3. Implementation of an automated Matlab procedure for the post–processing of the DIC data. An important constraint was found in the DIC software for the post–processing of the data when more than one system was used. Also, the available tools of the software did not allow obtaining the cross–section of the specimens required for the stress computation. As a result, a Matlab script including a stable method for the fitting of ellipses was programmed. Among the automatic data that the script allows to obtain are: the evolution of the cross–section, the strain field distribution, the stress–strain curves and barreling (compression tests) or notch shape (tensile tests). These data being essential for the correlation of the material parameters and the validation of the constitutive models have been completely obtained in the context of this thesis. In addition, the implemented procedure is now available to be applied to any further material investigations.

4. Experimental procedure for tension and compression tests at constant strain rate. The TA6V alloy is strain rate sensitive and the

1.4. Contributions of the thesis

universal testing machine available in the Laboratory of Mechanics and Structures (ArGEnCo department, ULg) were not designed for controlled tests at a constant strain rate. As a result, a methodology was implemented in order to compute the user–defined input displacement required to performed constant strain rate tests with the available machines.

5. A validated set of material parameters of an anisotropic thermo–elastoplastic model based on the macroscopic orthotropic yield criterion CPB06 for three temperatures (RT, 150 °C and 400 °C) and low strain rates (10^{-3} to 10^{-1} s^{-1}).

6. A validated set of material parameters of an isotropic thermo–elasto–viscoplastic model based on the Norton–Hoff constitutive law with the isotropic von Mises yield locus for low strain rates (10^{-3} to 10^{-1} s^{-1}) and moderate temperatures (from RT to 400 °C).

7. A comparative study of the predictions of the isotropic–thermo–elasto–viscoplastic approach and of an anisotropic thermo–elastoplastic one with experimental results representative of the mechanical behavior of TA6V at moderate temperatures and low strain rates for different strain paths. Main conclusions of this study help designers to make the right decision in choosing the constitutive law for the simulations of the mechanical behavior of the TA6V alloy with similar microstructure as the one studied here.

1.5. Organization of the thesis

The thesis contains an introduction chapter that discusses the state of the art, the context, the motivations and the contributions of the thesis research.

In Chapter 2, the implemented methods for the experimental campaign are described. First, the implementation of a procedure for tests at constant strain rates with universal testing machines is presented. The importance of performing the tests at constant strain rate is also highlighted with comparative results of two tests: with constant and not–constant strain rates. Second, the main difficulties found in the manipulation of the CCD cameras

are listed, together with advices in order to obtain reliable measurements of displacement fields by using digital image correlation (DIC).

In Chapter 3 [†], a reliable methodology is implemented in order to accurately determine the evolution of the cross–section of cylindrical specimen by using a 3D DIC system. In addition, the bulk compression test of an elliptic cylinder is proposed for characterization purposes. The main outcome of this chapter is that the numerical simulations of compression test of the proposed specimens including friction show inhomogeneous axial strain distribution affected by the plastic anisotropy of the material. This observation allows proposing and justifying the use of the inverse modeling of compression tests for the identification of the strength differential (SD) effect and the plastic anisotropy of TA6V, which is applied in the next chapter.

In Chapter 4[‡], the anisotropic behavior of the TA6V alloy is investigated at room temperature (RT). The well–known macroscopic orthotropic yield criterion CPB06 developed by Cazacu et al., 2006 is selected, as it captures both the anisotropy and the SD effect. This criterion is identified from a set of monotonic tests: uniaxial tensile, uniaxial compression, simple shear and

---

[†] Based on one published article:

- Tuninetti, V., Gilles, G., Péron–Lührs, V. Habraken, A.M., 2012. *Compression test for metal characterization using Digital Image Correlation and Inverse Modeling*, Procedia IUTAM. 4, 206–214.

[‡] Based on two published papers and one submitted article:

- Tuninetti, V., Gilles, G., Milis, O., Pardoen, T., Habraken, A.M. *Anisotropy and tension–compression asymmetry predictions of the plastic response of bulk Ti–6Al–4V alloy*. Submitted to International Journal of Plasticity.
- Tuninetti, V., Gilles, G., Milis, O., Neira, I., Habraken, A.M., 2013. *Quasi–static mechanical behaviour of Ti–6Al–4V alloy at room Temperature*. Proceedings of the XII International Conference on Computational Plasticity – Fundamentals and Applications, 51–62. Barcelona, Spain. (ISI).
- Tuninetti, V., Gilles, G., Milis, O., Lecarme, L., Habraken, A.M., 2012. *Compression test for plastic anisotropy characterization using optical full–field displacement measurement technique*. Steel Research International, Special Edition: 14th Int. Conf. Metal Forming 2012, 1239–1242.

1.5. Organization of the thesis

plane strain states performed on the TA6V at RT and at a low strain rate equal to 10^{-3} s^{-1}. The anisotropic hardening behavior is described by linear interpolation of continuous CPB06 yield surfaces identified at several plastic work levels, which makes it possible to describe the different hardening rates in tension, compression and shear. Inverse modeling including uniaxial stress–strain curves in tension, plane strain, shear as well as Finite Element (FE) analyses of compression tests are used to adjust the material parameters. Finally, the sensitivity of different sets of computed material parameters to the identification method as well as the capacity of the model to accurately predict forces and displacement fields are discussed.

Chapter 5[§] presents the evolution of the tensile and compressive behavior of the TA6V with the temperature and strain rate in one direction of the material. The identification of the CPB06 model is conducted here at 150 °C and 400 °C at one strain rate (equal to 10^{-3} s^{-1}). The Simulated Annealing (SA) algorithm (Metropolis *et al.,* 1953, Hastings, 1970) is selected in order to fit the material parameters on the experimental yield stress ratios. The inverse modelling is not used in this identification as DIC system is not applicable to high temperature tests. Furthermore, an isotropic thermo–elasto–viscoplastic Norton–Hoff model is also identified at 150 °C and 400 °C in order to compare and quantify the accuracy of CPB06 and Norton-Hoff model predictions versus experiments. Both approaches are assessed by comparing the error on the load predictions in tensile tests on round bars with u–notch, v–notch, and central hole as well as on compression tests at several temperatures and strain rates.

Finally, the overall conclusions of the research discussed in this thesis are given in Chapter 6, together with proposed further topics for future research.

[§] Based on the published article:

- Tuninetti, V., Habraken, A.M., (2014). *Impact of anisotropy and viscosity to model the mechanical behavior of Ti–6Al–4V alloy*. Material Science and Engineering: A, 605, 39–50.

1.6. References

Burkins, M., Hansen, J., Paige, J., Turner, P., 2000. The effect of thermomechanical processing on the ballistic limit velocity of extra low interstitial titanium alloy Ti–6Al–4V. U.S. Army research laboratory ARL–MR–486, 1–69.

Burkins, M., Wells, M., Fanning, J., Roopchand, B., 2001. The Mechanical and Ballistic Properties of an Electron Beam Single Melt of Ti–6Al–4V Plate. U.S. Army Research Laboratory, ARL–MR–515.

Cazacu, O., Plunkett, B., Barlat, F., 2006. Orthotropic yield criterion for hexagonal close packed metals. Int. J. Plasticity 22, 1171–1194.

Deyuan, F., Fort III, W., Horvath, R., 2001. Experience with titanium heat exchangers in refinery services. Mater. Performance 40, 56–60.

Elias, C.N., Lima, J.H.C., Valiev, R., Meyers, M.A., 2008. Biomedical applications of titanium and its alloys. JOM 60, 46–49.

Follansbee, P.S., Kocks, U.F., 1988. A constitutive description of the deformation of copper based on the use of the mechanical threshold. Acta Metallurgica 36, 81–93.

Gilles, G., Hammami, W., Libertiaux, V. Cazacu, O. Yoon, J.H., Kuwabara, T., Habraken, A.M., Duchêne, L. 2011. Experimental characterization and elasto–plastic modeling of the quasi–static mechanical response of TA–6 V at room temperature. Int. J. Solids Struct. 48, 1277–1289.

Gurrappa, I., 2003. Characterization of titanium alloy Ti–6Al–4V for chemical, marine and industrial applications, Materials Characterization. Mater. Charact. 51, 131–139.

Hammami, W., Tirry, W., Coghe, F., Duchene, L., Delannay, L., Habraken, A.M., 2011. Ti6A14V anisotropy and texture evolution predictions using Multisite and self consistent crystal plasticity models. The 12th World Conference on Titanium Ti–2011.

1.6. References

Hastings, W.K., 1970. Monte Carlo sampling methods using Markov chains and their applications. Biometrika 57, 97–109.

Johnson, G.R., Cook, W.H, 1983. A constitutive model and data for metals subjected to large strains, high strain rates and high temperatures. Proceedings of the 7th International Symposium on Ballistics: 541–547.

Khan, A.S., Kazmi, R., Farroch, B., 2007. Multiaxial and non–proportional loading responses, anisotropy and modeling of Ti–6Al–4V titanium alloy over wide ranges of strain rates and temperatures. Int. J. Plasticity 23, 931–950.

Khan, A.S., Suh, Y.S., Kazmi, R., 2004. Quasi–static and dynamic loading responses and constitutive modeling of titanium alloys. Int. J. Plasticity 20, 2233–2248.

Khan, A.S., Yu, S., 2012a. Deformation induced anisotropic responses of Ti–6Al–4V alloy. Part I: Experiments. Int. J. Plasticity 38, 1–13.

Khan, A.S., Yu, S. Liu, H., 2012b. Deformation induced anisotropic responses of Ti–6Al–4V alloy Part II: A strain rate and temperature dependent anisotropic yield criterion, . Int. J. Plasticity 38, 14–26.

Lecarme, L., 2013. Viscoplasticity, Damage and Fracture of Ti–6Al–4V. PhD thesis, Université Catholique de Louvain, Belgium.

Lee, W.S., Lin, C.F., 1998. Plastic deformation and fracture behaviour of TA6V alloy loaded with high strain rate under various temperatures. Mater. Sci. Eng. A 241, 48–59.

Long, M., Rack, H.J., 2006. Titanium alloys in total joint replacement—a materials science perspective. Biomater 19, 1621–1639.

Lütjering, G., Williams, J.C., 2007. Titanium: Engineering Materials and Processes, Second ed. Springer–Verlag, Berlin.

Majorell, A., Srivatsa, S., Picu, R.C, 2002. Mechanical behavior of TA6V at high and moderate temperatures – Part I: Experimental results. Mater. Sci. Eng. A 326, 297–305.

Montgomery, J.S., Wells, M.G.H., 2001. Titanium armor applications in combat vehicles. JOM 53, 29–32.

Metropolis, N., Rosenbluth, A.W., Rosenbluth, M.N., Teller, A.H., Teller, E., 1953. Equation of state calculations by fast computing machines. J. chem. Phys 21, 1087–1092.

Norton, F. H., 1929. The Creep of Steel at Hight Temperature, The McGraw–Hill, New York, USA.

Odenberger, E.L., Hertzman, J., Thilderkvist, P., Merklein, M., Kuppert, A., Stöhr, T., Lechler, J., Oldenburg, M., 2012. Thermo–mechanical sheet metal forming of aero engine components in Ti–6Al–4V – PART 1: Material characterisation. Int. J. Mater. Form., 1–12.

Peirs, J., 2012. Experimental characterisation and modelling of the dynamic behaviour of the titanium alloy Ti6Al4V. PhD thesis, Ghent University, Belgium.

Peirs, J., Verleysen, P., Degrieck, J., Coghe, F., 2010. The use of hat–shaped specimens to study the high strain rate shear behaviour of Ti–6Al 4V Int. J. Impact Eng. 37, 703–714.

Rack, H.J., Qazi J.I, 2006. Titanium alloys for biomedical applications. Mater. Sci. Eng. C 26, 1269–1277.

Sukumar, G., Bhav Singh, B., Bhattacharjee, A., Siva Kumar, K., Gogia, A.K., 2013. Ballistic impact behaviour of β–CEZ Ti alloy against 7.62 mm armour piercing projectiles. Int. J. Impact Eng. 54, 149–160.

Tuninetti, V., Gilles, G., Péron–Lührs, V. Habraken, A.M., 2012a. Compression Test for Metal Characterization using Digital Image Correlation and Inverse Modeling, Procedia IUTAM. 4, 206–214.

Tuninetti, V., Gilles, G., Milis, O., Lecarme, L., Habraken, A.M., 2012b. Compression test for plastic anisotropy characterization using optical full–field displacement measurement technique. Steel Res. Int. SE: 14th Int. Conf. Metal Forming 2012, 1239–1242.

1.6. References

Vanderhasten, M., Rabet, L., Verlinden, B., 2008. Ti–6Al–4V: Deformation map and modelisation of tensile behaviour. Materials & Design 29, 1090–1098.

Zerilli, F.J., Armstrong, R.W., 1987. Dislocation–mechanics–based constitutive relations for material dynamics calculations. Journal of Applied Physics 61, 1816–1825.

Zhang, C., Li, X.–q., Li, D.–s., Jin, C.–h., Xiao, J.–j., 2012. Modelization and comparison of Norton–Hoff and Arrhenius constitutive laws to predict hot tensile behavior of Ti–6Al–4V alloy. Transactions of Nonferrous Metals Society of China 22, s457–s464.

Chapter 2. Experimental developments

The experimental developments required for the proper calibration of the constitutive laws representing the plastic behavior of TA6V are presented. The chapter is divided into two sections. Section 1 describes the procedure implemented to obtain constant strain rate tests with universal testing machine. Section 2 presents the methodology developed to accurately measure displacement fields with digital image correlation (DIC) and to post–process the data.

2.1. Development of a procedure to perform compression tests at constant strain rate

The first stage of the plastic characterization of the TA6V alloy supposes the identification of an initial yield locus, then its evolution with the plastic work, the temperature and the strain rate. In this thesis, this initial yield locus is defined at a plastic work equal to 1.86 J/cm^3 (0.2% tensile offset strain in LD direction), at RT and at a strain rate equal to 10^{-3} s^{-1}. The mechanical tests and specifically here the compression tests must therefore be performed at a constant strain rate equal to 10^{-3} s^{-1} for each of the identification temperatures. Universal testing machines are not always adapted for constant strain rate tests. In that case, the tests are performed at a constant die speed involving a non–constant strain rate response on the specimen. The data generated by these tests may be used either for validation purposes, or inverse identification of the strain rate sensitive material parameters. Nevertheless, when the material is also anisotropic, the inverse identification is not straightforward, it could be very time consuming and an accurate solution is not guaranteed.

The universal testing machines equipped with a closed–loop control system are used for constant strain rate tests. Nowadays, this feature is not available in the machines of the Laboratory of Mechanics and Structures (ArGEnCo, ULg). They only have the capability to be configured for ramping, sinusoidal or user–defined displacements of the cross–head before performing the test. The latter capability is used to develop a procedure for constant strain rate tests, by computing the proper user–defined

displacements using a Matlab script. The methodology is applied to both the compression tests and tensile tests for several temperatures. In the next subsection, the compression test at RT has been selected for the presentation of the procedure.

2.1.1. Theoretical basis

The average true axial compression strain in the sample as a function of time is defined by Eq. 2.1

$$\varepsilon(t) = \ln\left(\frac{H_0 + X_{ep}(t)}{H_0}\right) \tag{2.1}$$

H_0 is the initial height of the specimen and $X_{ep}(t)$ (negative for compression) the specimen displacement or height reduction.

Applying the derivative $\left(\frac{d(\ )}{dt}\right)$ to the Eq. 2.1, the expression becomes

$$\dot{\varepsilon} = \frac{1}{H_0 + X_{ep}(t)} \frac{d\left(X_{ep}(t)\right)}{dt} \tag{2.2}$$

Reordering Eq. 2.2, one may obtain the differential equation Eq. 2.3 and its solution Eq. 2.4.

$$-\frac{d\left(X_{ep}(t)\right)}{dt} + \dot{\varepsilon}\, X_{ep}(t) + \dot{\varepsilon}\, H_0 = 0 \tag{2.3}$$

$$X_{ep}(t) = H_0\left(\exp(\dot{\varepsilon}\, t) - 1\right) \tag{2.4}$$

From Eq. 2.4, on may compute the time t as a function of the known value of the specimen displacement $X_{ep}(t)$.

$$t = \frac{1}{\dot{\varepsilon}} \ln\left(\frac{H_0 + X_{ep}(t)}{H_0}\right) \tag{2.5}$$

Eq. 2.4 allows computing the sample displacement as a function of time $X_{ep}(t)$, for a required test at a constant strain rate $\dot{\varepsilon}$. This $X_{ep}(t)$ could be used as the user–defined displacement of the actuator only if the displacement is imposed according to an extensometer directly applied on the specimen. This is the case for the tests performed with the tensile testing machine at RT, where imposing the user–defined displacement computed with Eq. 2.4, one can reach a constant strain rate test. However, high temperature extensometers for tensile tests are not currently available in MS^{2}F. Besides, in the testing machine used for compression tests, the sensor associated to the user–defined displacement is connected in the actuator (cross–die). In these two cases (compression tests and high temperature tensile), the rigidity of the machine should be first identified and considered in order to impose the proper displacement or deformation of the specimen for the constant strain rate tests.

The load depending on the cross–section of the tested sample may attain high values especially on alloys with high yield strength as the TA6V. Consequently, this high load produces a non–negligible deflection of the parts of the testing machine, which must be considered for the computation of the user–defined displacement of the actuator. Note that the rigidity of the machine relies on the configuration of the dies, the position of the actuator and the testing temperature. Thus, it should be obtained when any change on the initial configuration of the machine or testing environment takes place.

Imposing a cross–head global displacement $X_{gl}(t)$ with the purpose of reaching a specific specimen displacement $X_{ep}(t)$ needs a previous knowledge of the machine deflection $X_{ma}(t)$. This deflection could be measured during the test of a sample with a specific material, however $X_{ma}(t)$ depends on the load supported by the machine, and this load also depends on the strain rate sensitivity of the material.

The only solution to reach a constant strain rate test without knowing the material behavior during only one test is by using the closed–loop control feature.

A second option, which is explained in the next section, is to perform a consecutive series of tests. The number of tests before reaching a constant

strain rate test will vary according to the sensitivity of the specimen–actuator system (machine rigidity and the strain rate sensitivity of the tested material). For the TA6V studied here and the rigidity of the available machine, the constant strain rate is reached at the second test.

2.1.2. Procedure for a test at a constant strain rate

Firstly, the rigidity of the machine is identified. In a second step, a material sample is tested at a constant cross–head speed in order to determine the behavior of the system machine–specimen. These two sets of data allow computing the proper global displacement of the actuator (cross–head) for a test at a constant strain rate both in elastic and plastic strain ranges..

2.1.2.1. Load–deflection curve of the testing machine

The load–deflection curve of the testing machine at a specific cross–head position and testing temperature is obtain with a compression test of the dies (test without specimen). Fig. 2.1 shows the characteristic shape of the load–deflection curve at RT.

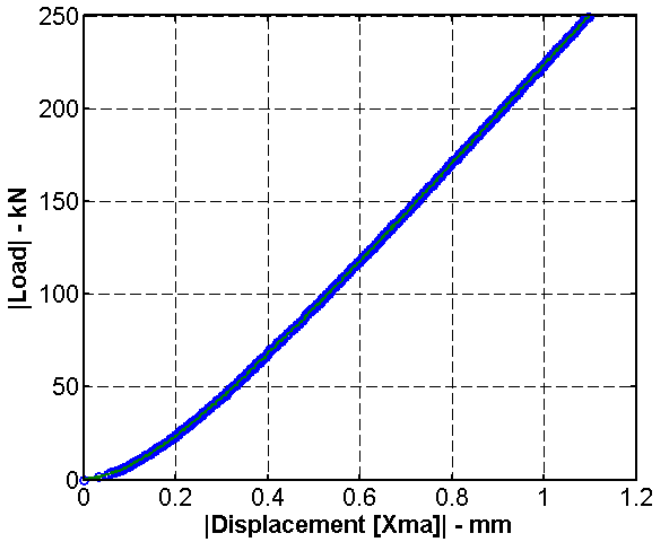

Figure 2.1. Example of a load–deflection curve of the testing machine (SCHENCK Hydropuls 400 kN press) for a specific configuration at RT.

2.1.2.2. Compression test 1 at constant cross–head speed

The sample is tested at a constant cross–head speed (test 1) in order to obtain the deflection response of the system machine–sample. The value of the constant die speed for this test must be defined in such a way that the strain rate obtained on the sample is as close as possible to the targeted constant strain rate. This die speed is computed, without neglecting the expected machine deflection X_{ma} , as the rate between the final global displacement of the cross–head and the time of the test (Eq. 2.8).

$$v = \frac{X_{gl}}{\Delta t} = \frac{X_{ep} + X_{ma}}{\Delta t} \tag{2.6}$$

Considering that the average targeted strain rate $\dot{\varepsilon}$ is defined as the variation of the strain $\Delta\varepsilon$ ($\Delta\varepsilon = \varepsilon_F$ considering that the initial strain $\varepsilon_0 = 0$) for a certain interval of time Δt (Eq. 2.7), one may obtain Δt with Eq. 2.8.

$$\dot{\varepsilon} = \frac{\Delta\varepsilon}{\Delta t} \tag{2.7}$$

$$\Delta t = \frac{\Delta\varepsilon}{\dot{\varepsilon}} = \frac{\varepsilon_F}{\dot{\varepsilon}} \tag{2.8}$$

Replacing X_{ep} from Eq. 2.4 and Δt from Eq. 2.8 into Eq. 2.6, the expression for the average die speed becomes,

$$v = \dot{\varepsilon}\,\frac{H_0\left(\exp\left(\varepsilon_F\right)-1\right)+X_{ma}}{\varepsilon_F} \tag{2.9}$$

X_{ma} corresponds to the total deflection of the machine and must be guessed a priori from the expected average load during the test (expected material properties) and the machine rigidity (Fig. 2.1). The load displacement curve obtained from a constant cross–head test (test 1) by using Eq. 2.9 is shown in Fig. 2.2. In order to compute the specimen deformation X_{ep}, the load–deflection curve of the testing machine and the load vs. displacement curve of the test 1 must be set at identical load sampling frequency (Fig. 2.3).

2.1. Development of a procedure to perform compression tests at constant strain rate

Once X_{ep} is known, the strain is obtained by using Eq. 2.1 and the stress is automatically computed by assuming volume conservation and no barreling (Eq. 2.10).

$$\sigma = \frac{F}{A_0 \cdot \exp(-\varepsilon)} \tag{2.10}$$

where F is the measured load, A_0 the initial cross-sectional area of the sample.

This procedure has been implemented in an independent Matlab script in order to automatically obtain the stress–strain curves from the data generated by the universal testing machine.

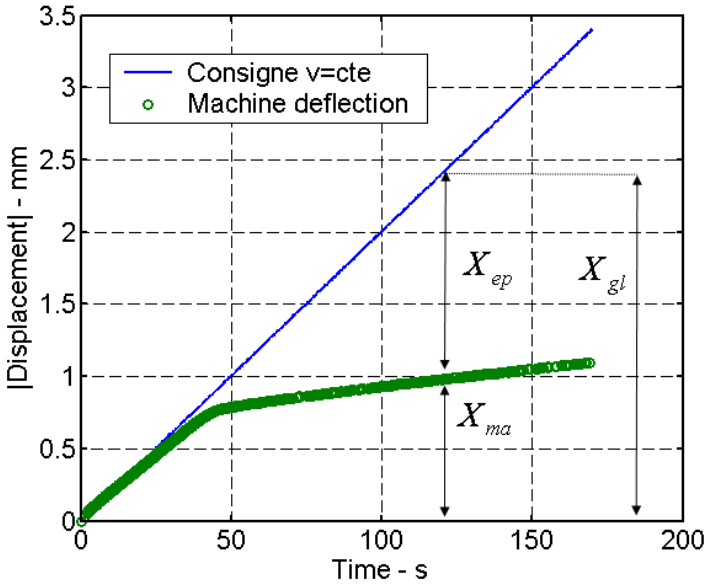

Figure 2.2. Deflection of the machine (SCHENCK Hydropuls 400 kN press) and TA6V specimen deformation in a constant cross–head speed test (test 1) at $v = 0.021$ mm/s.

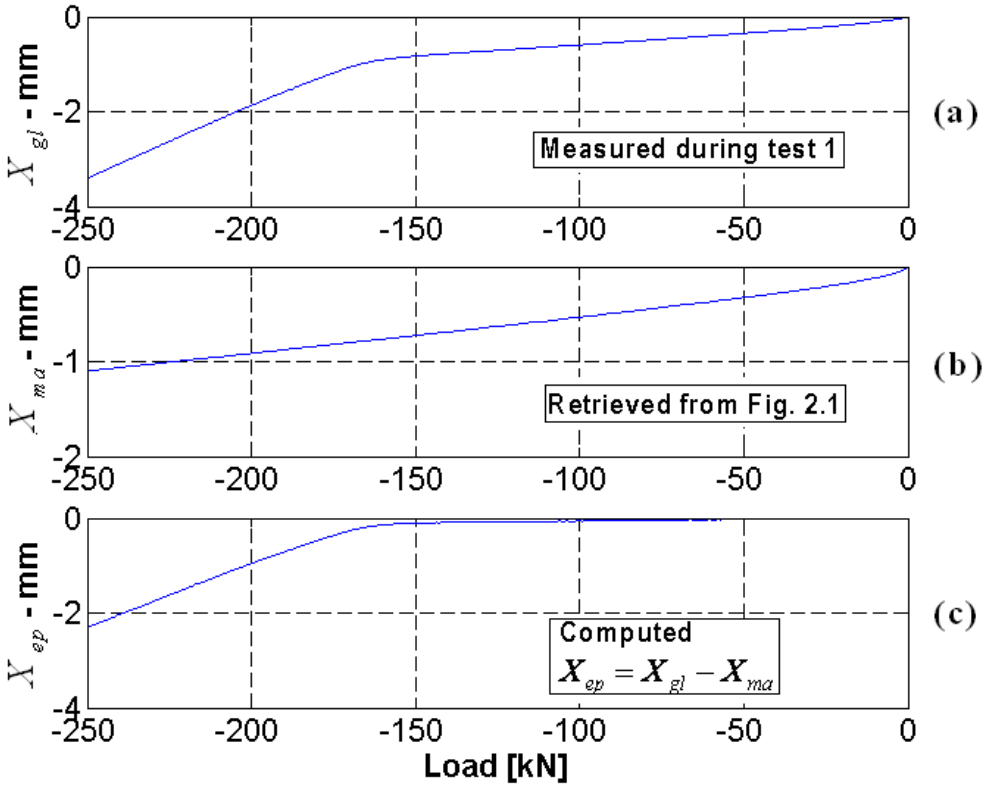

Figure 2.3. Displacement vs. load curves at identical sampling frequency of the load. (a) Constant cross–head speed test (test 1), (b) deflection vs. load curve of the machine and (c) computed specimen deformation $X_{ep} = X_{gl} - X_{ma}$.

($v = 0.021$ mm/s, targeted $\dot{\varepsilon} = 0.001 s^{-1}$, TA6V sample).

The stress–strain and strain–time curves obtained in the test 1 are shown in Fig. 2.4. It can be seen from Fig. 2.4b that the reached strain rate during the test 1 is not constant. The elastic strain rate is very far from the targeted one (10^{-4} s^{-1} instead of 10^{-3} s^{-1}), because in this domain the load increases at a very high rate which produces high machine deflections. However, when the sample becomes plastic, the load increases at a low rate due to the hardening behavior of the TA6V alloy. This low load rate induces less machine deflections and therefore, a strain rate closer to the targeted one, but still not constant, particularly at the onset of plasticity.

2.1. Development of a procedure to perform compression tests at constant strain rate

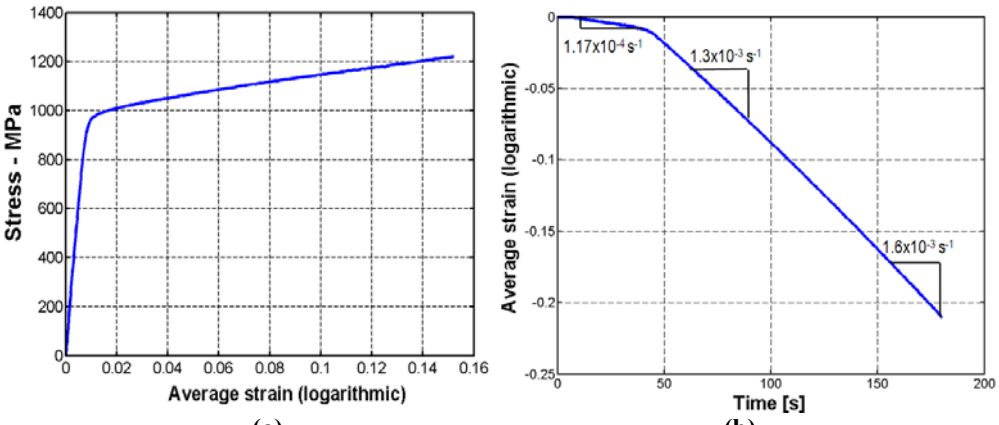

(a) (b)

Figure 2.4. (a) Axial true stress – axial true strain curve and (b) axial true strain time curve at constant cross–head speed. ($v = 0.021$ mm/s, targeted $\dot{\varepsilon} = 0.001 s^{-1}$, TA6V sample).

2.1.2.3. The user-defined displacement for the test 2 at constant strain rate

The objective is to determine the *user–define displacement* $\left(X_{gl}\right)$ in such a way that the height reduction of the specimen $\left(X_{ep}\right)$ follows the theoretical Eq. 2.11 (for a constant strain rate test, e.g. equal to 10^{-3} s^{-1}).

$$X_{ep\_TEST2}(t) = H_0\left(\exp\left(\dot{\varepsilon}\, t\right) - 1\right) \quad \text{(Theoretical)} \tag{2.11}$$

First, the behavior of system machine–specimen $X_{ma}\left(X_{ep}, \dot{\varepsilon}\right)$ at the constant strain rate equal to $10^{-3} s^{-1}$ must be known in order to impose the proper user–defined displacement $X_{gl\_TEST2}(t)$ for the constant strain rate test. This behavior is not accurately known due to that the compression test is not yet performed at the targeted constant strain rate. However, the behavior of the system–machine at a constant cross–head speed is assumed to be similar to the one on the targeted constant strain rate test. This assumption is valid while the system behavior is very similar in both cases.

$$X_{ma}\left(X_{gl\_TEST2}\right) = X_{ma}\left(X_{gl\_TEST1}\right) \tag{2.12}$$

X_{gl_TEST2} should be determined as a function of time that we called here t_2. The time t_2 is computed by shifting of the curve X_{gl_TEST1} (for a certain point at the time t^*) over the time difference between the curves X_{ep_TEST1} and the $X_{ep\_TEST2(THEORETICAL)}$ (t^*_2–t^*) assuming Eq. 2.12. A similar estimated shift is applied to other points as observed for t^+ and t^o (Fig. 2.6) by using the Eq. 2.11 rearranged as shown in Eq. 2.13.

$$t_2 = -\frac{1}{\dot{\varepsilon}} \ln\left(\left(\frac{X_{ep\_TEST1}(t)}{H_0}\right)+1\right) \tag{2.13}$$

As observed in Fig. 2.6b, imposing the user–defined displacement $X_{gl\_TEST2}(t_2)$ in the test 2, the constant strain rate is reached. The methodology is similarly applied to tensile tests and both have been implemented as Matlab scripts.

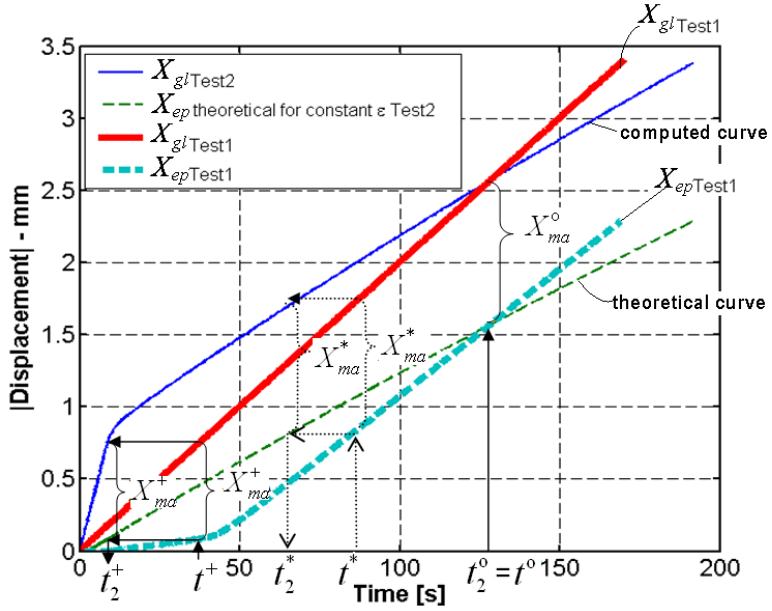

Figure 2.5. Schematic representation of the user–defined displacement computation by the shifting of the X_{gl_TEST1} over the time difference between the X_{ep_TEST1} and the $X_{ep(THEORETICAL)}$.

2.1. Development of a procedure to perform compression tests at constant strain rate

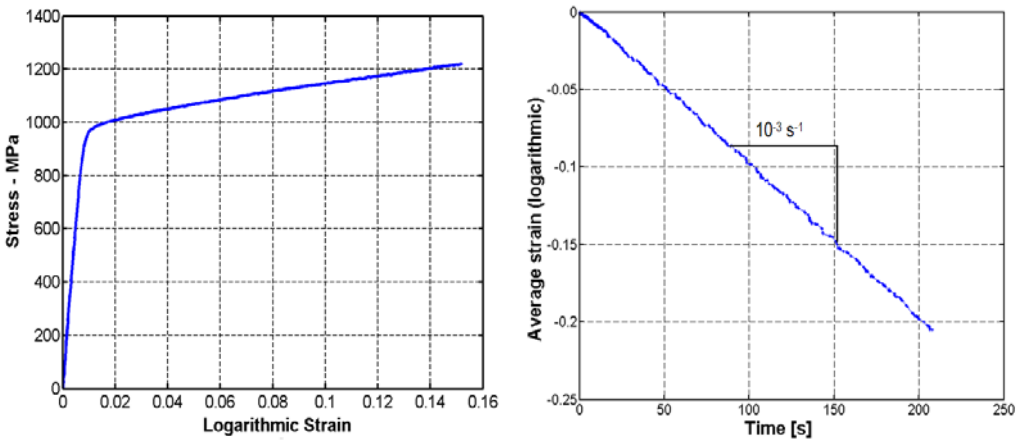

(a) (b)

Figure 2.6. (a) Axial true stress – axial true strain curve and (b) axial true strain time curve at constant strain rate $\dot{\varepsilon} = 0.001 s^{-1}$ for a TA6V sample.

2.1.3. An assessment of the strain rate sensitivity of TA6V

The stress–strain responses of two types of tests performed on TA6V at several temperatures (RT, 150°C, 400 °C, 600 °C) are compared (Fig. 2.7):

1. The first type of test is performed at constant die (cross–head) speed by using Eq. 2.9 and the targeted strain rate equal to 10^{-3} s^{-1}. Two merely constant strain rates for the plastic (around to $1.2x10^{-3}$ s^{-1}) and the elastic (around to 10^{-4} s^{-1}) response can be observed for all the temperatures (Fig. 2.7)

2. The second type of test is performed at a constant strain rate equal to 10^{-3} s^{-1} by using the methodology presented in Section 2.1.2.

The difference between the yield stress level for a test at a constant strain rate and at a constant cross–head speed increases with the temperature. As observed in Fig. 2.7(c-d) and Fig. 2.8, the variation in the strain rate can lead to a large inaccuracy in the estimation of the proper yield stress of the alloy for a targeted strain rate. However, no influence at RT for the TA6V alloy has been found in the stress–strain response. This observation is expected due to the low initial strain hardening of the TA6V observed at RT. The low loading rate immediately after the onset of plasticity produces a

negligible deflection of the machine. In this way, the imposed ramping displacement computed for a targeted strain rate is completely absorbed by the specimen. Therefore, the strain rate level targeted is immediately reached.

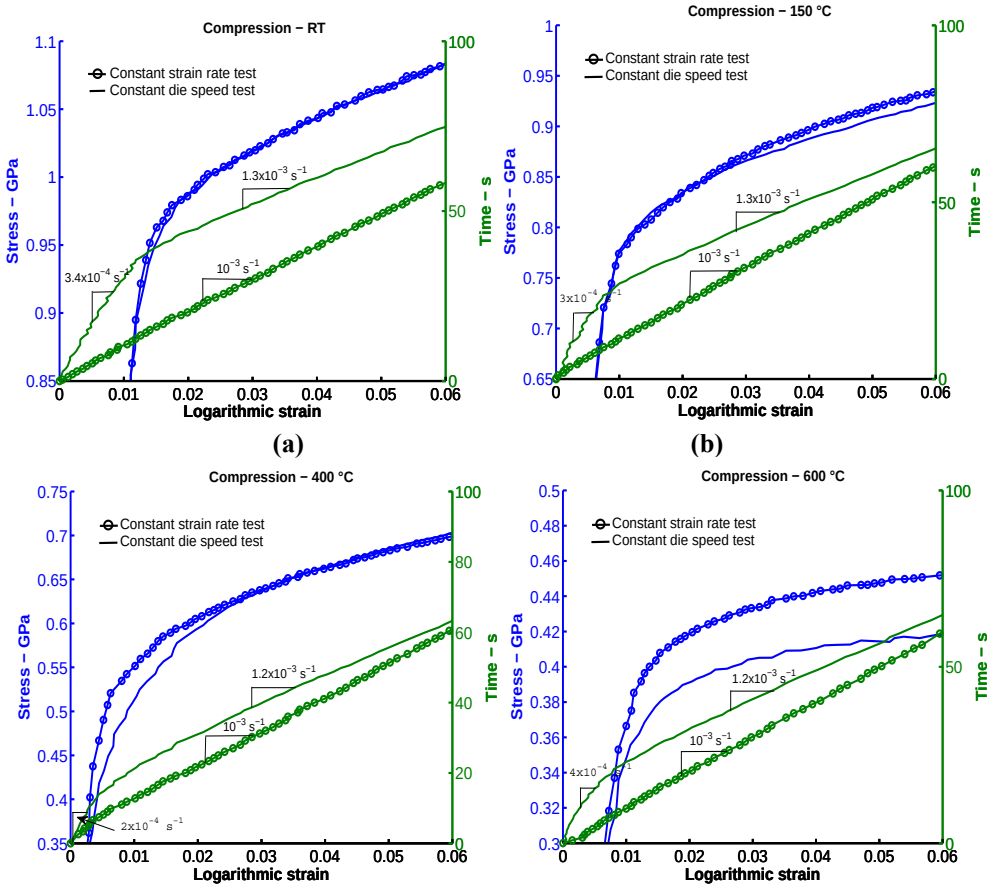

Figure 2.7. Comparison between stress–strain curves of compression tests at constant die speed and constant strain rate at (a) RT, (b) 150 °C, (c) 400 °C , (d) 600 °C.

2.1. Development of a procedure to perform compression tests at constant strain rate

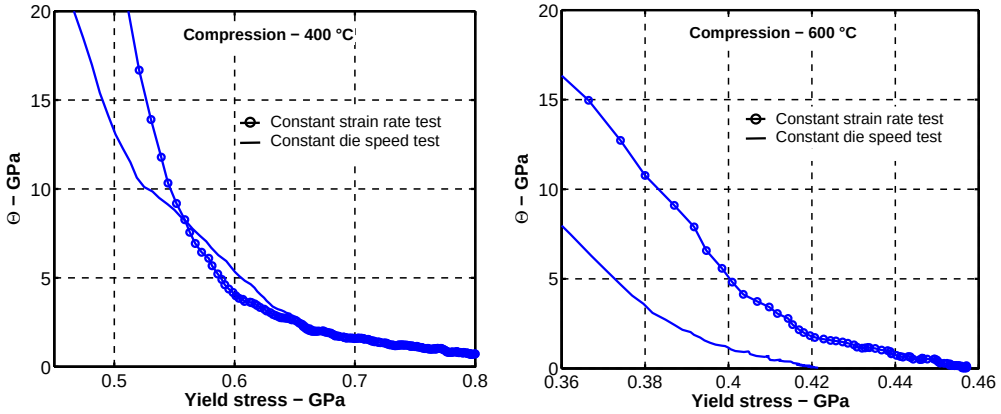

(a) **(b)**

Figure 2.8. Comparison between the evolution of the strain hardening rate $\left(\theta = \partial\sigma_y \big/ \partial\varepsilon_y^p\right)$ with the yield stress σ_y of compression tests at constant die speed and constant strain rate at (c) 400 °C and (d) 600 °C. ε_y^p is the accumulated plastic strain.

2.2. Development of tests with Digital Image Correlation (DIC)

The development of digital image correlation (DIC) with the stereo–vision principles allows measuring the strain and displacement field evolution of the tested specimens. These data are very useful not only for model validation purposes but also to identify material parameters through inverse identification method. A complete review of the essential concepts underlying the use of the 3D–DIC can be found in Sutton, 2008, IUTAM 2012.

In this thesis, the commercial Vic3D DIC software from Correlated Solutions (http://www.correlatedsolutions.com/) and the Limess (www.limess.com) system are used to measure the displacement/strain fields of the tensile and compression tests. An experimental methodology is developed and successfully applied to accurately determine the cross–sections, the displacement/strain field evolution of the samples and the true stress–strain curves. The procedure for the post–processing of the DIC data implemented as a Matlab scripts is explained in detail in Chapter 3.

Chapter 2. Experimental development

Accurate results from DIC are hard to obtain because a deep knowledge, experience and high levels of technical and practical skills are required. The main difficulties dealing with the manipulation of the CCD cameras, the speckles, the paint and the DIC software are listed hereafter.

1. *Adequate ductility of the paint.* Various brands and types of spray paint were tested before finding the optimal one. The proper ductility of the paint is needed in order to follow large displacements and strains of specimens until the onset of fracture. Many of the spray paints available in the market were not suitable due to the appearance of paint cracks during the test much earlier than the fracture of the specimens. The ductility was found influenced by the moment when the paint was applied. The later the tests is performed the lower the ductility. Today, the MoTip Heat-resistant Spray paint brand is used shown excellent adhesion and ductitlity.

2. *Proper subset size and optimal size of black dots for the speckle pattern*. The optimal speckle coverage lies between 40% and 70% (Lecomte et al., 2006). Stickers developed in the Mechanics of Materials and Constructions (Vrije Universiteit Brussel) with optimized speckle pattern were tested in the studied specimens with no accurate result due to its lack of ductility. However, the optimal size with spray paint was applied and the subset was selected as smaller as possible in the size range between 3x3 to 10x10 pixels.

3. *Tolerances of the dimensions of the specimens required for the reproducibility of the tests*. The study of the sensitivity of experimental results to the initial dimension of the samples was done and the required tolerances for the compression tests were computed (Tuninetti and Habraken, 2011).

4. *Fixing of cables and supports of the cameras*. For any relative movement of the cameras, the calibration parameters change and inaccuracies on the reconstructed 3D–shape appear. The vibrations or the relative movements between two cameras of the same system were removed by the fabrication of dedicated supports.

5. *Adequate lighting*. In order to avoid high errors in the correlation and the computation of the strain fields, several lamps were tested at

different positions. A cold light was obtained with FotoQuantum StudioMax Daylight Kit with Softboxe and 30 Watts bulbs eqauivalent to 150 Watts (Fig. 2.8). No strong light reflections on the image appeared. The environment of the testing was also isolated to avoid changes in the brightness of the image and the loss of the image correlation sequence.

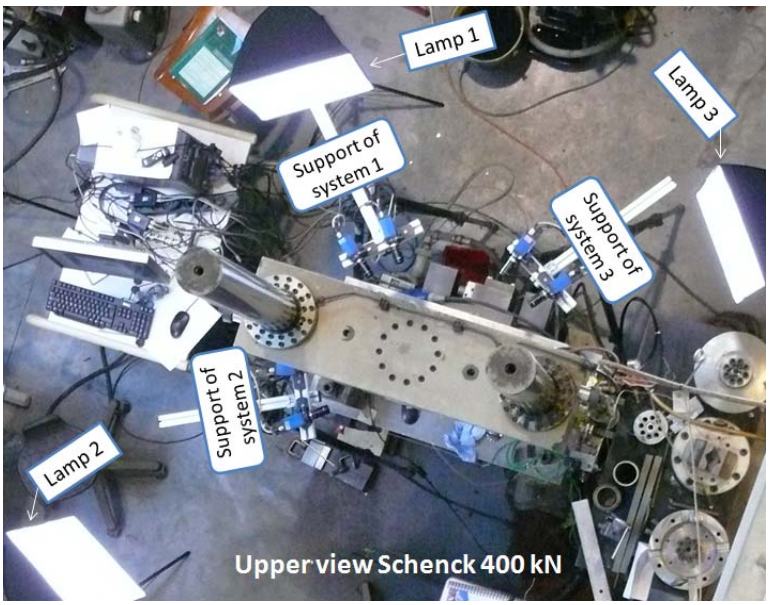

Figure 2.9. Position of supports and lamps.

6. *Highest experimental resolution*. The experimental resolution is defined as the measured distance along one pixel. It varies with the distance between the cameras and the specimen as well the focus of the lenses. CCD-Limess cameras with 50 mm lenses were used. Extension tubes were added between the lens and the camera body. These acquired extension tubes of 10 mm allowed to bring closer the sample to the cameras, improving the resolution of the images (30 µm/pixel) and therefore the accuracy of the results.

7. *Aperture, exposure time and focus*. The aperture or size of the lens opening allows more light to fall on the sensor of the camera. The focal length of the lenses is used to achieve a sharp focus of the specimen. A larger aperture makes the image brighter. However, it

also decreases the depth of field (the range over which the focus is sharp). Exposure time is the amount of time the camera sensor collects light before reading a new image. Longer exposure times make the image brighter but can also create blur, if significant motion happens during the exposure times. Several focus, exposure time and aperture were tested in order to obtain sharp images, and therefore accurate correlations. The optimal values found for the configuration of compression and tension tests with the Limess CCD cameras, extension tubes of 10mm and 50mm lenses were 5.6 for the aperture, 15 ms for exposure time and focus for a depth of field varying from 5 to 10 mm depending on the targeted point of the specimen.

8. *Scripts for automatic post–processing of the DIC data*. An important constrain of the VIC–3D software was found when using more than two CCD cameras. A Matlab scripts was developed with the following capabilities: the generation of export files and graphs of the measurements of the cross–section of the samples including the standard deviation, the strain field distribution at certain stages of test, the average strain–time response, the stress–strain curves and the barreling in compression tests or the notch shape in tensile tests.

Finally, this new knowledge developed in the context of this thesis about DIC measurements was transferred to the technicians of the Laboratory of Mechanics and Structures (ArGEnCo department, Université de Liège), as practical training, detailed manual, procedure reports and Matlab scripts. In addition, the technique has been applied to several academic research projects (e.g. Conthedas, DINOSAURE RW and PAI Belspo P6/24 FRIA grant G. Gilles) and industrial consultancy with successful results.

2.3. Conclusion

A procedure for compression and tension tests at constant strain rate was presented. The importance of implementing this capability for the characterization of the TA6V alloy was also highlighted. Besides, the main difficulties found in the manipulation of the CCD cameras were listed, together with advices in order to obtain reliable measurements of displacement fields by using the DIC technique.

2.4. Appendix A. Automatic results obtained with Matlab scripts

The interested reader may refer the report RWI 15 (Tuninetti and Habraken, 2012) for a detailed description of the DIC post-proccesing procedure. The Matlab scripts are available in the harddrive of Limess-PC (Laboratory of MS^{2}F) or in the MS^{2}F server: Z:\Fabulous\Résultats d'essais\Matlab Scripts.

1. LIMESS_POST_PROCESSING_TENSILE.m for tensile tests.
2. LIMESS_POST_PROCESSING_COMPRESSION_V3.m for compression tests.

Next sections A.1 and A.2 are cut and paste from the automatic reports generated by the Matlab scripts. These figures are discussed in next chapters. Appendix A is here used to keep detailed information for the next script users.

A.1. Results of tensile tests of round bar with notch R4 aligned with the LD direction

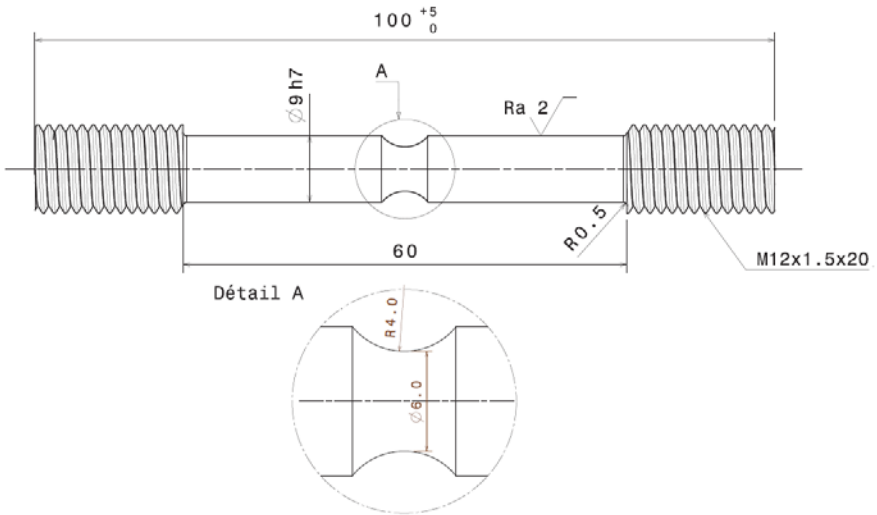

Figure A.1. Geometry and dimension of the TA6V notch tensile specimen R4.

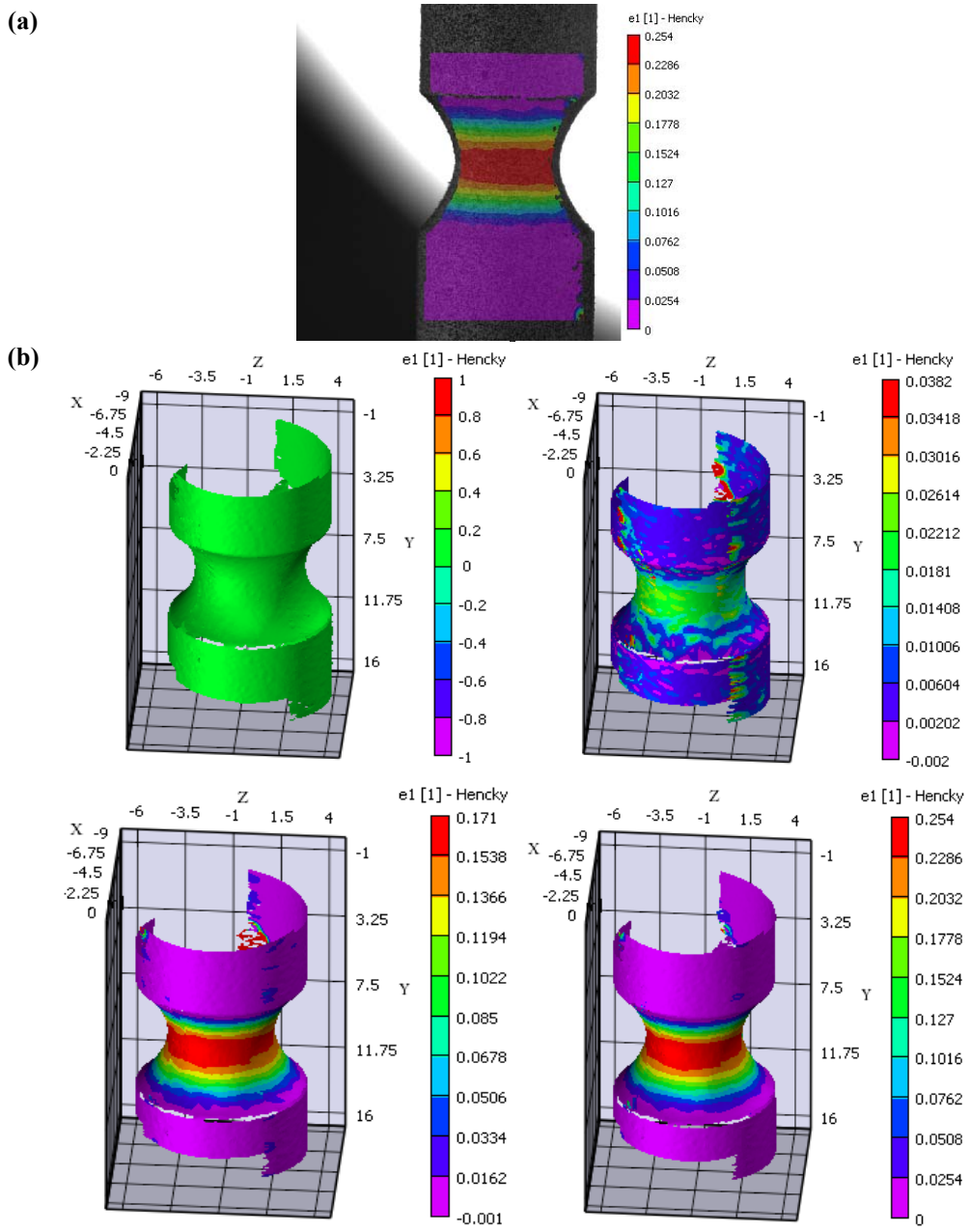

Figure A.2. (a) 2D image of the sample with the strain field just before fracture. (b) Axial strain and 3D geometry evolution of the sample (aligned with the LD direction of the material (Fig. 4.1)) obtained with VIC3D Limess software at different stages during testing.

Appendix A. Automatic results obtained with Matlab scripts

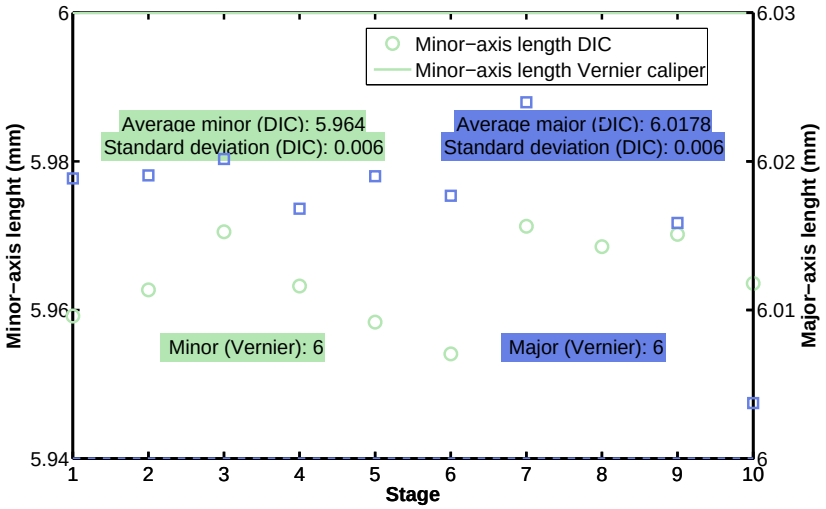

Figure A.3. Initial minor and major axis length (of the fitted ellipse) for the first ten stages[**] (images) of the initial geometry without deformation.

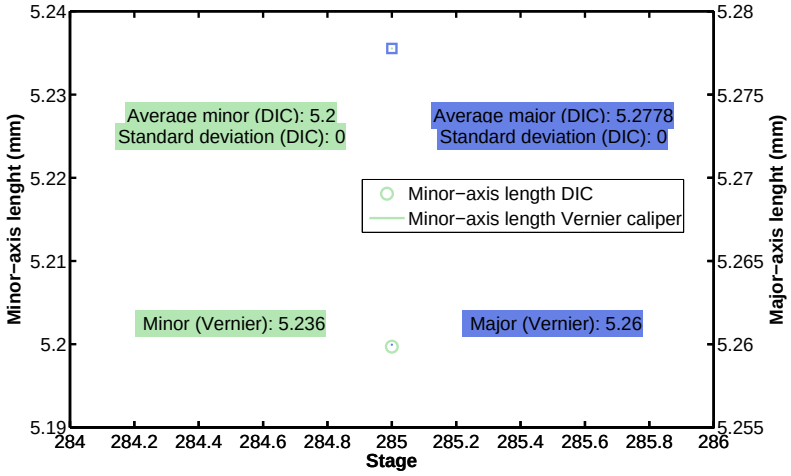

Figure A.4. Final minor and major axis length of the fitted ellipse of the last stage.

[**] A stage is related to the time when the image is registered during the test. Note that for the first ten stages no loading is applied. Besides, the total number of the stages is related to the acquisition frequency of images. Generally higher frequency is required for the elastic range than the plastic one.

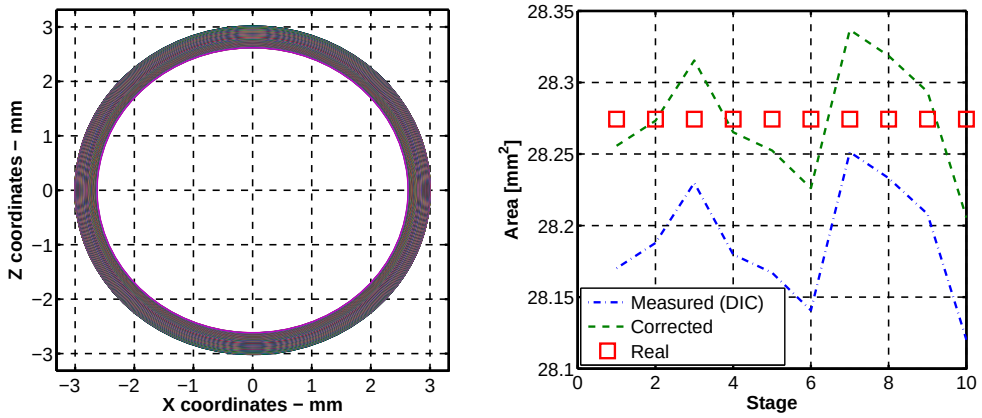

(a) (b)

Figure A.5. (a) Evolution of the measured cross-section (b) Correction of the measured cross-sectional area by fitting the minor and major axis length measured with the Vernier caliper (Real)[††].

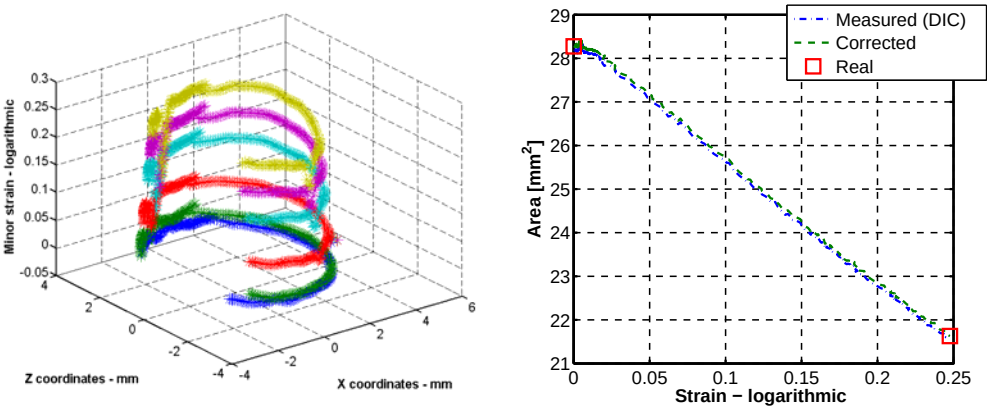

(a) (b)

Figure A.6. (a) Evolution of the axial strain field in the surface of the middle cross-section (b) Evolution of the measured cross-sectional area with the axial strain. Axial strain is computed by averaging the axial strain distribution in the surface of the middle cross-section

[††] Applied correction is described in report RWI 15 (Tuninetti and Habraken, 2012). The report RWI 15 only describes the post-processing of the compression tests. The tensile test results are presented here as additional information

Appendix A. Automatic results obtained with Matlab scripts

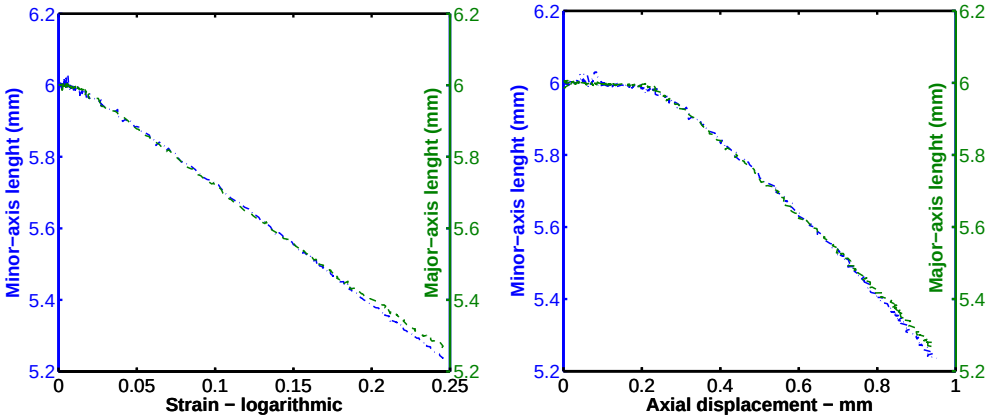

(a) (b)

Figure A.7. Evolution of the minor and major axis length with (a) the axial strain and (b) the axial gauge displacement.

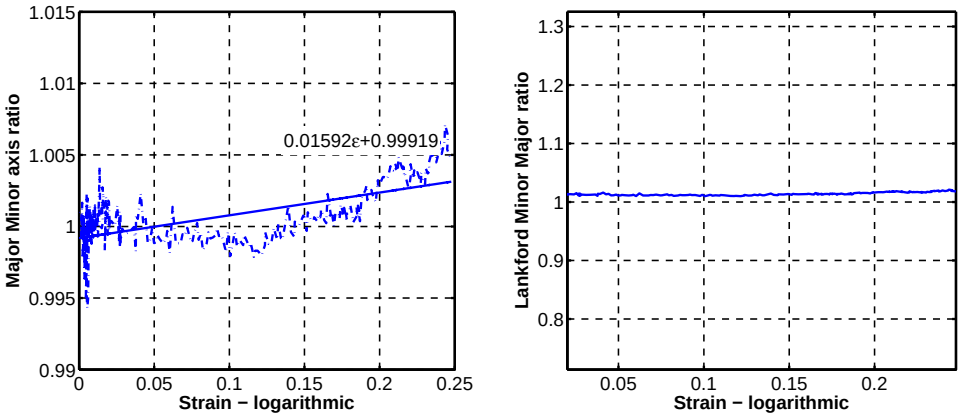

(a) (b)

Figure A.8. (a) Evolution of the major minor axis ratio with the axial strain. (b) Evolution of the Lankford (R-value) with the axial strain. The definition of the R-value is given in section 4.2.3.

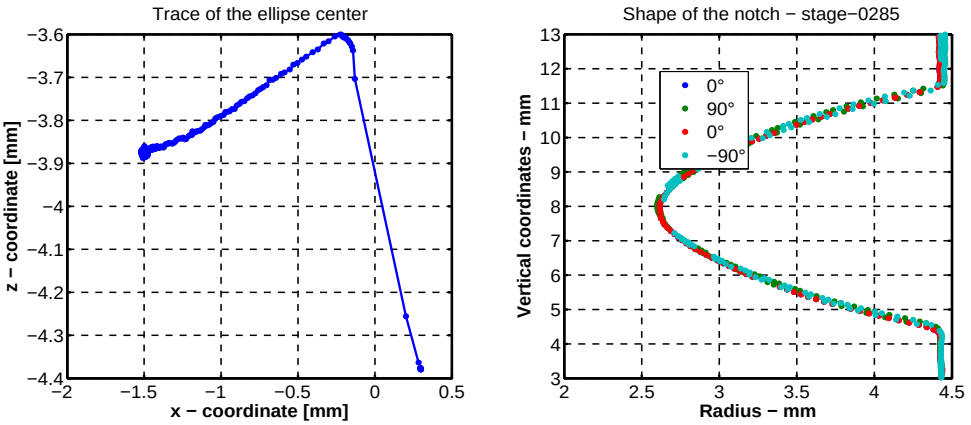

(a) (b)

Figure A.9. (a) Displacement of the center of the cross-section during the test. (b) Notch shape at the minor (90°) and at the major (0°) axis.

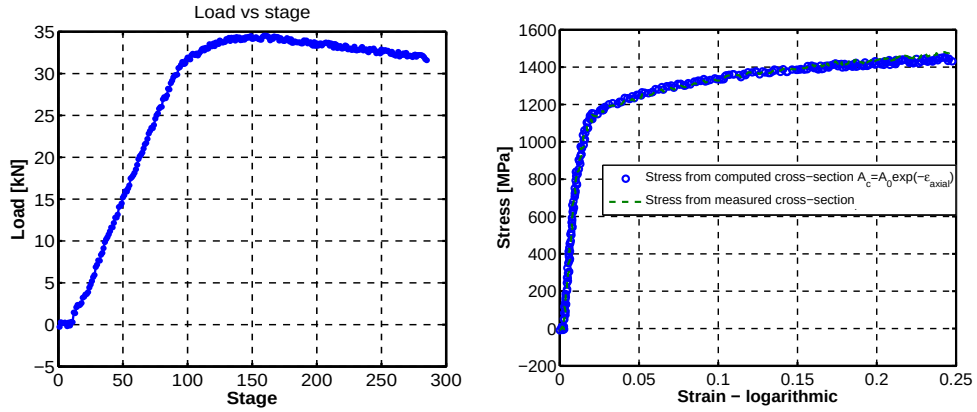

(a) (b)

Figure A.10. (a) Axial load vs. stage. (b) Stress vs. axial strain.

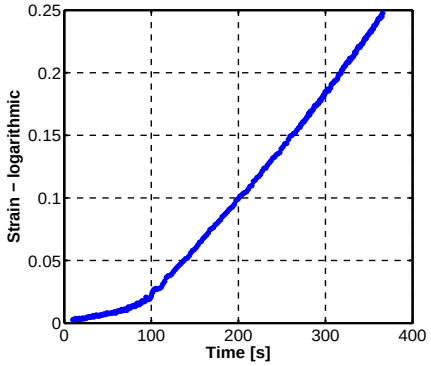

Figure A.11. Evolution of the axial strain with the time.

A.2. Results of compression tests LD direction

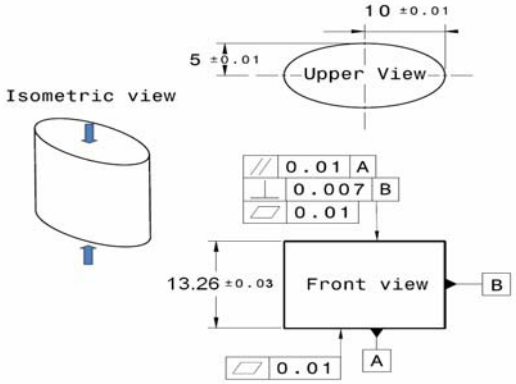

Figure A.12. Geometry and dimension of the compression specimen.

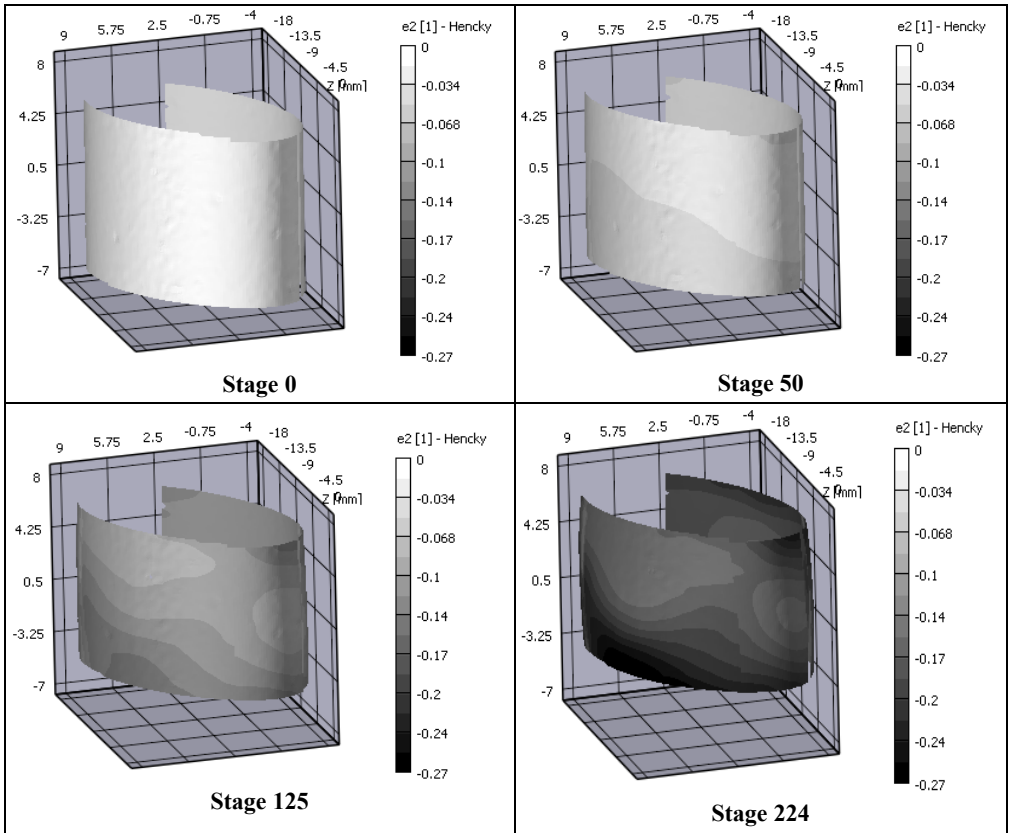

Figure A.13. Axial strain field and 3D geometry evolution (LD direction).

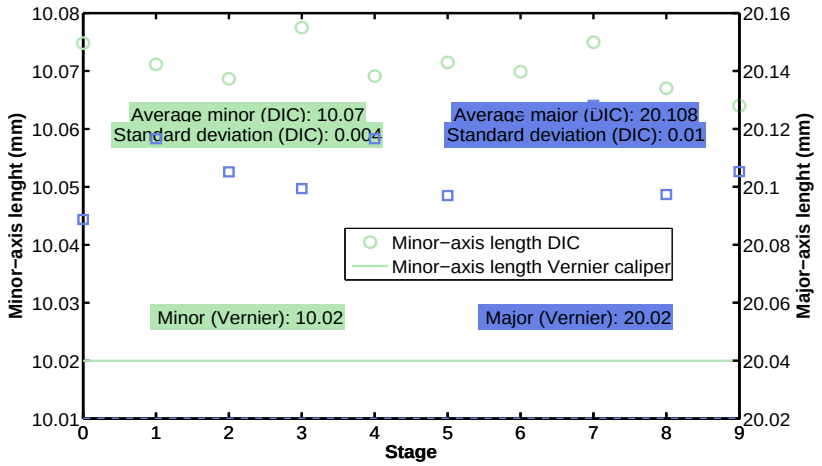

Figure A.14. . Initial minor and major axis length (of the fitted ellipse) for the first ten stages (images) of the initial geometry without deformation.

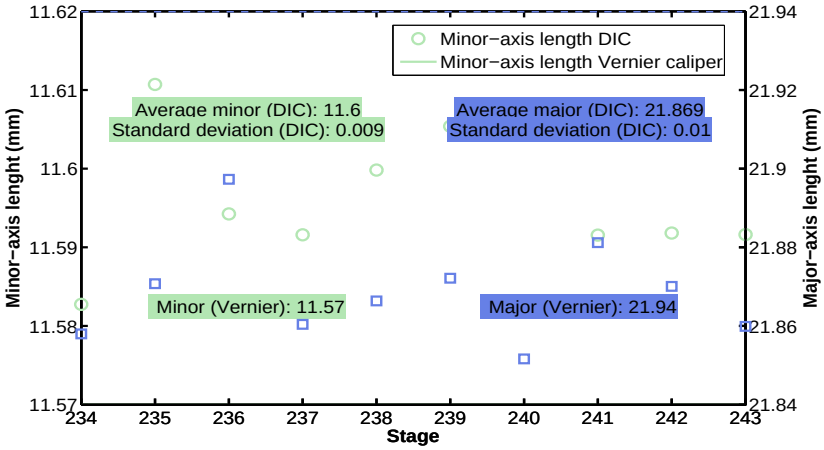

Figure A.15. Final minor and major axis length of the fitted ellipse for the last stage.

Appendix A. Automatic results obtained with Matlab scripts

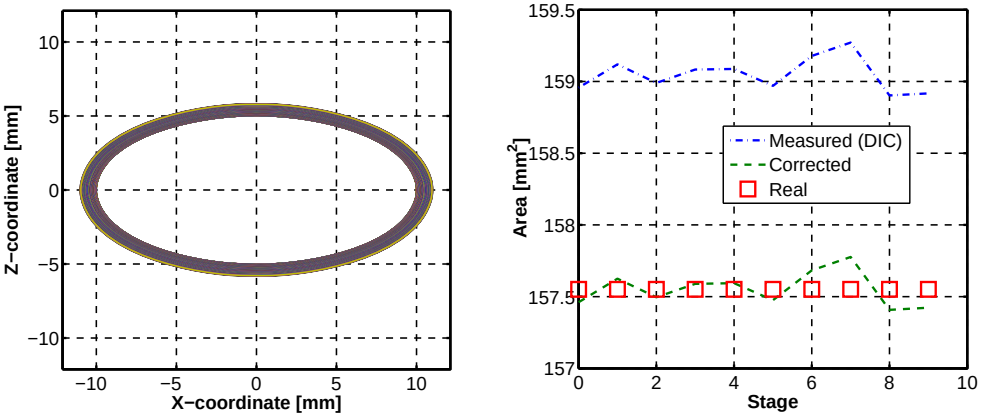

(a) (b)

Figure A.16. (a) Evolution of the measured cross-section (b) Correction of the measured cross-sectional area The cross-sectional area by fitting the minor and major axis length measured with the Vernier caliper (Real)[‡‡].

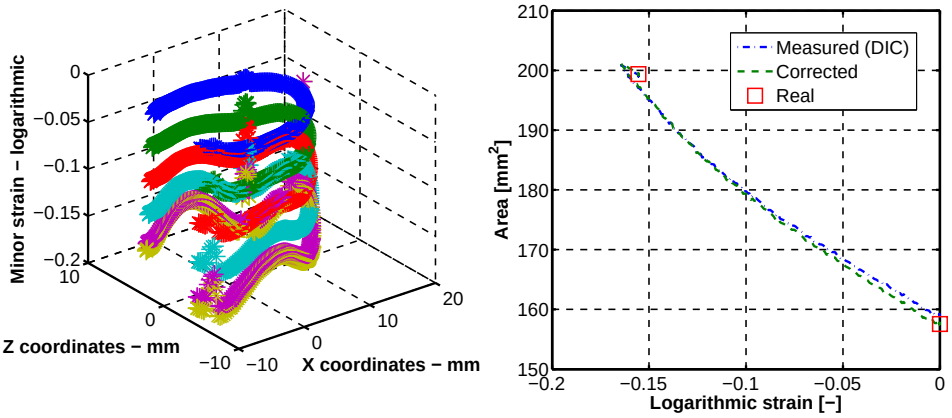

(a) (b)

Figure A.17. (a) Evolution of the axial strain field in the surface of the middle cross-section (b) Evolution of the measured cross-sectional area with the axial strain.

[‡‡] Applied correction is described in report RWI 15 (Tuninetti and Habraken, 2012).

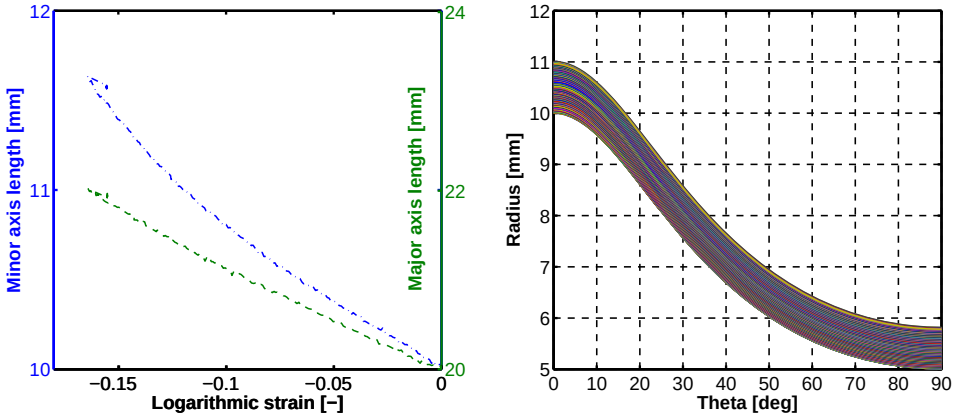

(a) (b)

Figure A.18. (a) Evolution of the major minor axis ratio with the axial strain. (b) Evolution of the radius vs. theta.

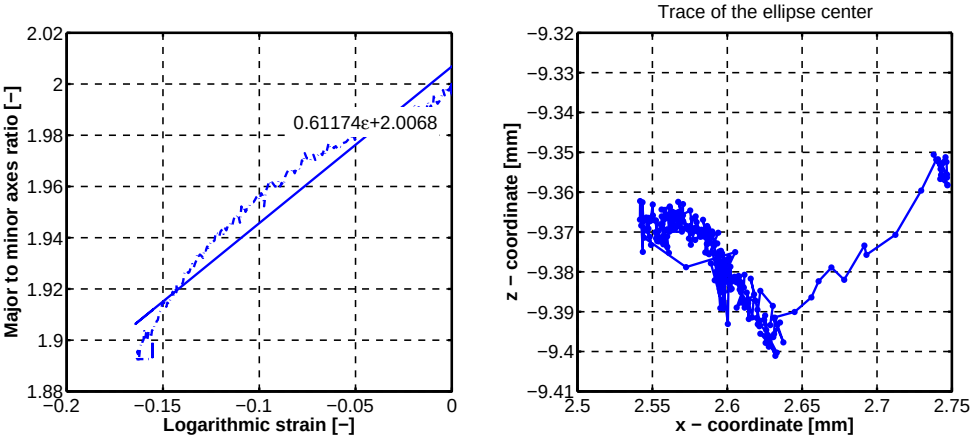

(a) (b)

Figure A.19. (a) Evolution of the major to minor axis ratio with the axial strain (b) Displacement of the center of the cross-section during the test.

Appendix A. Automatic results obtained with Matlab scripts

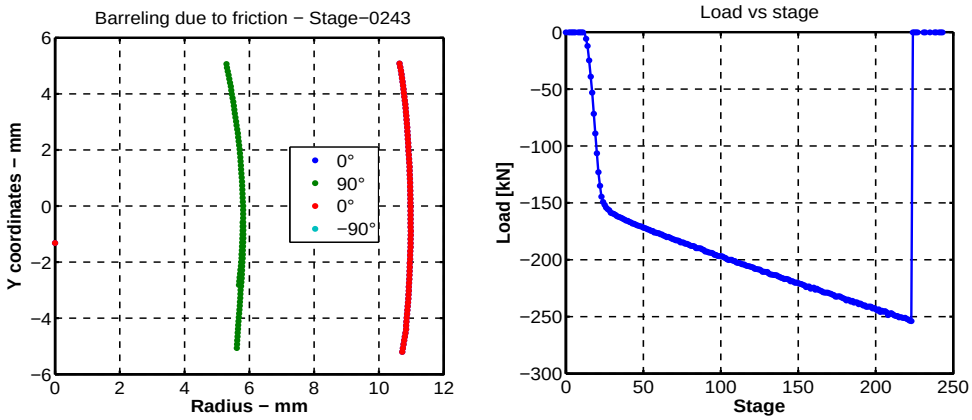

(a) (b)

Figure A.20. (a) Barreling at the minor (90°) and at the major (0°) axis. (b) Load vs. stage.

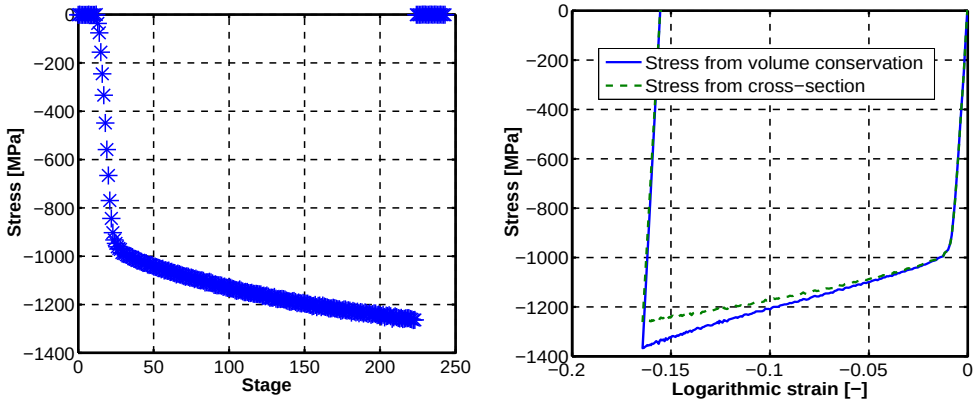

(a) (b)

Figure A.21. (a) Stress vs. stage. (a) Stress vs. average axial strain.

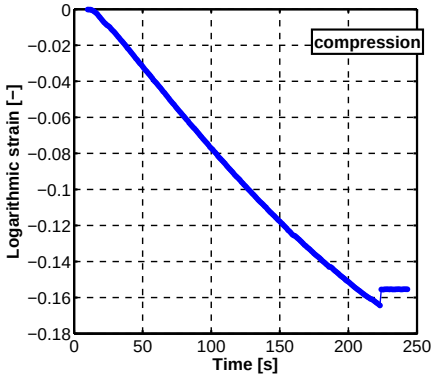

Figure A.22. (a) Average axial strain vs. time.

2.5. References

Halir, R., Flusser, J., 1998. Numerically Stable Least Squares Fitting of Ellipses. Proceedings of the International Conference in Central Europe on Computer Graphics and Visualization. WSCG '98. Plzen, Czech Republic, 125–132.

IUTAM 2012, Symposium on full-field measurements and identification in solid mechanics 4, 1–226 (Cachan, France 4–8 July 2011).

http://www.correlatedsolutions.com

http://www.Limess.com

Lecompte, D., Sol, H., Vantomme, J., Habraken, A., 2006. Analysis of speckle patterns for deformation measurements by digital image correlation. Proc. SPIE 6341, Speckle06: Speckles, From Grains to Flowers, 63410E.

Sutton, M.A., 2008. Digital image correlation for shape and deformation measurements. In: Sharpe, W.N. (Ed.), Handbook of Experimental Mechanics, Springer, 565–600.

Tuninetti, V., Habraken, A.M., 2011. Analysis of fabrication tolerances required for the elliptic cylinder sample. 11th internal report of Fabulous project, Intermediary report semester 3rd and 4th (convention RWI N° 716670).

Chapter 3. Compression test for plastic anisotropy characterization using digital image correlation and inverse modeling

This chapter is based on the published article: *Compression test for metal characterization using digital image correlation and inverse modeling*

Authors: V. Tuninetti, G. Gilles, V. Péron–Lührs, A.M. Habraken

Journal: Procedia IUTAM 4 (2012) 206 – 214 © 2010 Published by Elsevier Ltd

In this chapter, an elliptical cylinder specimen is proposed and tested for bulk TA6V alloy. The full–field optical technique (3D digital image correlation) with three camera systems (Limess) allows out–of–plane displacement/strain fields on around 300° of the specimen. The use of this technique easily provides the barreling profile used to compute Coulomb's friction coefficient by using the inverse method. A reliable methodology is also implemented in order to determine the evolution of the cross–section of cylindrical specimen. This methodology allows computing stress–strain curves more accurately than conventional methods.

Furthermore, numerical simulations of compression test on the elliptical cross–section specimens including friction are performed in order to study the influence of the plastic anisotropy to the axial strain field. The simulation results allow justifying and proposing the use of the inverse modeling of compression tests for the identification of the plastic anisotropy of material. Note that this chapter is more detailed than the IUTAM 2012 article.

3.1. Introduction

3.1. Introduction

The accuracy of numerical simulations of forming process highly depends on the quality of the material data provided. These material data can be obtained by performing a set of mechanical tests, as tensile, shear, plane strain and compression tests at several directions. Compression tests on circular cylindrical cross–section specimens are widely used (Poortmans et al., 2009, Merklein and Kuppert, 2009, Coppieters et al., 2011) but for sheet metal characterization, the complicated layer alignment is time consuming and may induce a wrong anisotropy characterization.

In order to compute the true stress, evolution of the actual loaded surface must be computed or measured. Merklein and Kuppert, 2009 propose 2 methods for circular cross–section specimen and plastic anisotropic materials. They use two 3D–DIC systems placed perpendicularly and one of them is aligned with the rolling direction. Very small local area information of displacement and strain are measured at the horizontal middle plane of the specimen. The first method assumes that displacements are associated to the radii variation of the minor and major axis of the deformed elliptic shape. The actual area is computed by the simple formula $A=\pi\ (r_0+\Delta r_{system1})\ (r_0+\Delta r_{system2})$, where r_0 is the initial circular radius of the specimen. However, the author could not guarantee that the specimen stays in the center of the testing area (rolling direction and perpendicular one are indeed principal axes of the ellipse). Therefore the accuracy of the method is poor. The second method proposes an actual area formula ($A=0.0625\pi(r_0\ (\exp(\varepsilon_1)+\exp(\varepsilon_2)))^2$) as a function of the measured tangential strains by the optical system 1 and 2, respectively ($\varepsilon_1,\ \varepsilon_2$) in minor and major axis location. These tangential strain values are proportional to the change in diameter of the original geometry.

In this study, compression tests are performed on elliptical cross–section specimens for bulk titanium alloy TA6V. The specimen geometry proposed is very useful for the alignment of layers in case of sheet stack compression test. The proposed method here for the computation of the actualized area is based on fitting ellipses to the 300° of the measured cross–section data obtained from 3D–DIC at each stage of the test. The algorithm used for the ellipse fitting is proposed by Halir and Flusser, 1998. This accurate method for the area computation with the appropriate calibration parameters and the

test conditions provides a maximum relative error of 0.3% on the computed area. Compared to the second method described above it presents an advantage on accuracy, because it uses no formula depending on local values of tangential strains, but direct measurements of the cross–section of the tested specimen.

For plastic anisotropy characterization, stress strain curves and Lankford coefficients (R–values) are generally used. However, for full 3D identification of anisotropic constitutive laws by using Lankford coefficients, the number of compression tests highly increases and is time consuming. For this reason, the sensitivity of the plastic anisotropy to the axial strain field on the elliptical cylinder including friction is studied by numerical simulations. The observation found allows justifying and proposing the use of the inverse modeling of compression tests for the identification of the plastic anisotropy of materials.

3.2. Experimental setup and procedure

The compression tests are performed on elliptical cross–section samples on TA6V alloy in the Laboratory of Materials and Structures Mechanics in ArGEnCo department at the University of Liège. Specimens were machined by wire Electron Discharge Machining (EDM) with the dimensions shown in Fig. 3.1(a). The sample is compressed by a universal axial testing machine (SCHENCK Hydropuls 400 kN press). Three 3D optical measurement systems (6 CCD cameras) and the VIC–3D digital image correlation software are used to obtain the strain/displacement field (Fig. 3.2(b)). The speckle pattern is applied on the surface of the specimen by using a mat paint in order to avoid reflection (Fig. 3.2(a)). Fixed focus lens of 50 mm and extension tubes are used in order to obtain the highest experimental resolution. A subset size of 15x15 pixels is selected for speckles size of 5 pixels with around 60% optimal speckle coverage (Lecompte et al., 2006). The experimental resolution of the acquired images is 34 pixels per millimeter. Cables are fixed in order to avoid the relative movement (vibration) between 2 cameras, because the accuracy of 3D field reconstruction could be influenced. One channel of analog loading data is acquired and synchronized with the images. The relative position among the 3 camera systems and the specimen is shown in Fig. 3.2(b). This

3.2. Experimental setup and procedure

configuration allows an out–of–plane displacement/strain fields on around 300° of the specimen.

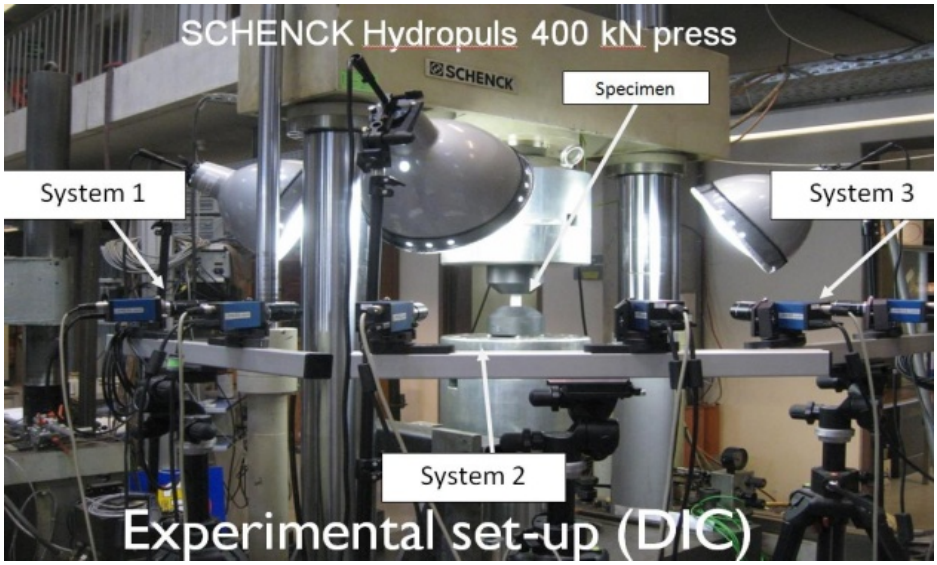

(a)

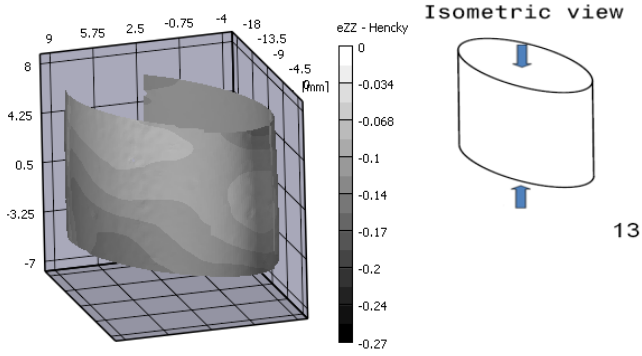

(b)

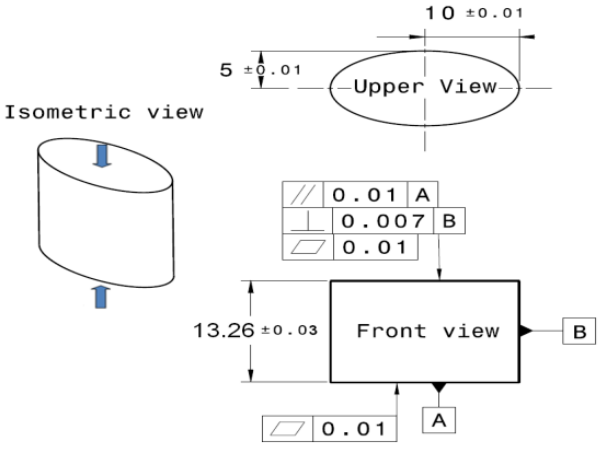

(c)

Figure 3.1. Compression tests (a) DIC system of 6 cameras providing full surface strain fields.(b) Axial strain field at 0.08 average axial strain (c) Geometry and dimensions of compression specimen (dimensions in mm).

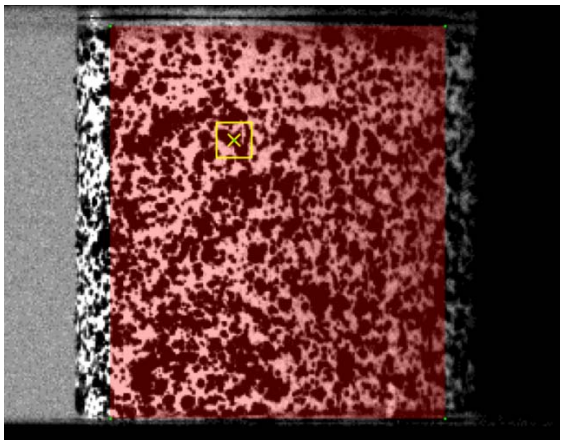

(a)

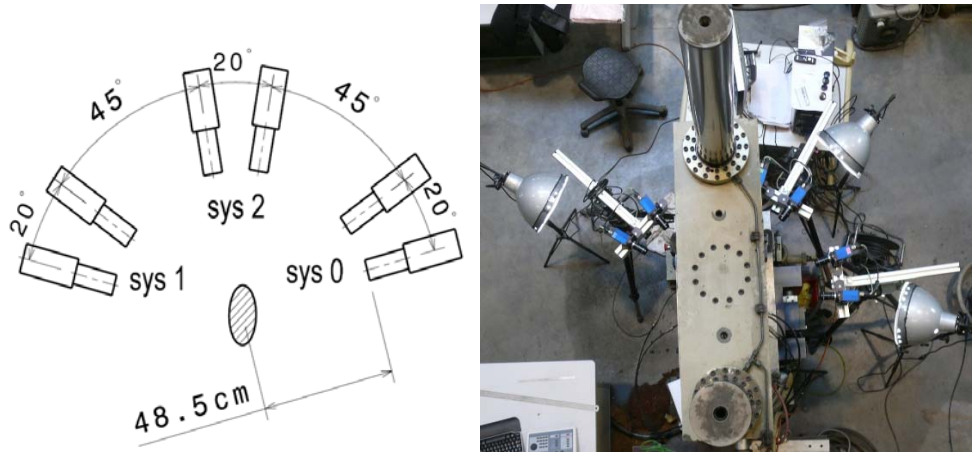

(b)

Figure 3.2. (a) Speckle pattern and (b) position of the CCD–cameras.

Friction is reduced between samples and the compression dies by using grease lubricant at each extremity of the specimen. Let us note that according to the final goal of the measurement: general shape of the yield locus defining the anisotropy features, it is not straightforward that friction should always be eliminated. In the current case, low barreling is observed during the test due to low friction and it was measured by the 3D DIC system. Coulomb's friction coefficient has been computed by inverse method by fitting the barreling from experimental and numerical results.

3.3. The new method for accurate cross–section area and true stress computation

Geometry evolution and axial logarithmic strain field are measured with the 3D optical measurement system and VIC3D 2007 software (DIC–Limess). Fig. 3.3 shows the measured geometry and strain field evolution of the specimen at 4 stages. Stage 0 corresponds to the initial specimen (before loading), stages 50 and 125 correspond to the specimen at 0.025 and 0.08 average axial strain, respectively, and the stage 224 at the end of the test at 0.16 average axial strain (unloaded condition).

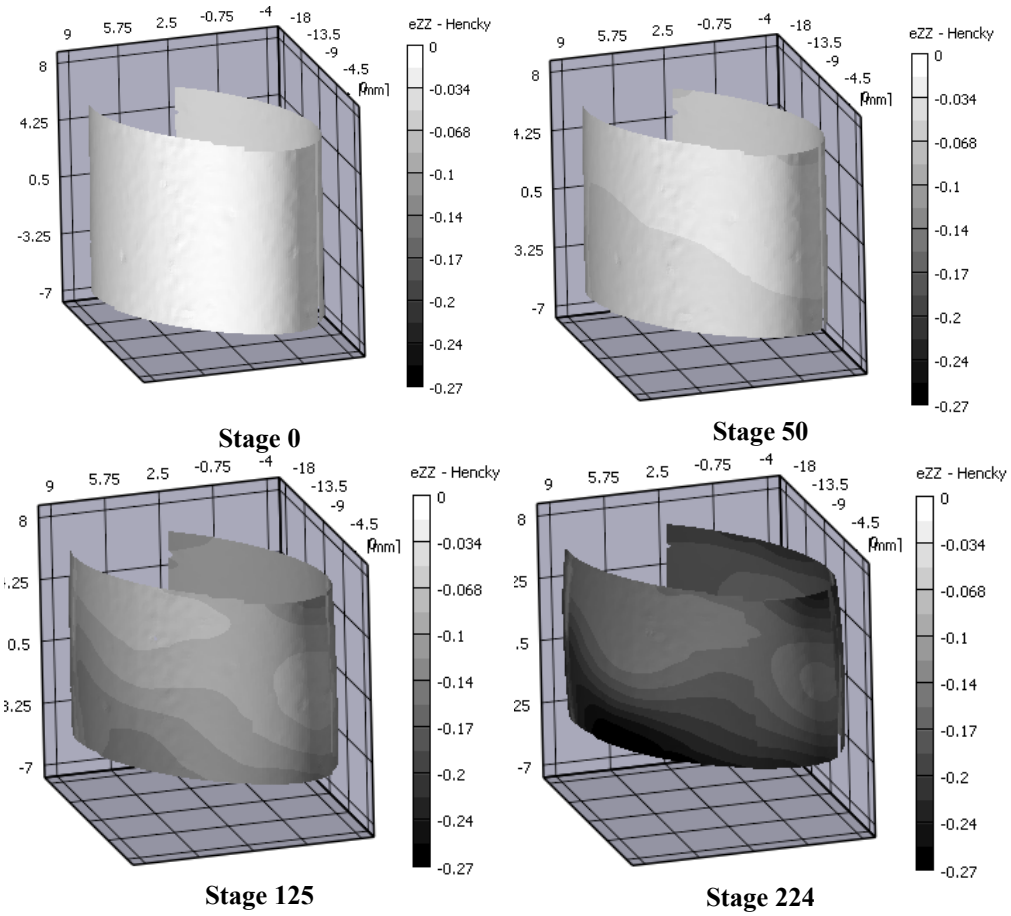

Figure 3.3. Evolution of the axial strain field on the free surface of the compression sample performed at (Cauchy or Henky strain).

The experimental points $P_i(x,z)$ obtained by DIC–Limess at the middle cross–section of the specimen and at an arbitrary stage are shown in Fig. 3.4.

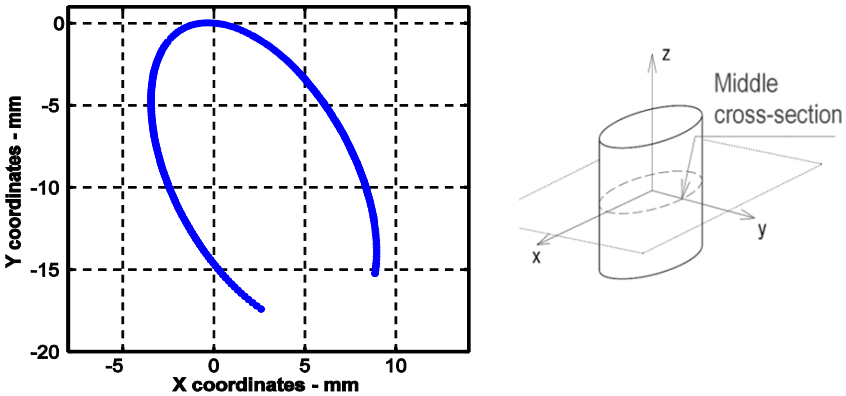

Figure 3.4. Experimental points measured with DIC at the middle cross–section of the specimen.

The general quadratic curve of an ellipse is defined by Eq. 3.1 to Eq. 3.3

$$ax^2 + 2bxz + cz^2 + 2dx + 2fz + g = 0 \tag{3.1}$$

$$M = \begin{vmatrix} a & b & d \\ b & c & f \\ d & f & g \end{vmatrix} \tag{3.2}$$

$$N = \begin{vmatrix} a & b \\ b & c \end{vmatrix} \tag{3.3}$$

with $I = a + c$, $\det(M) \neq 0$, $\det(N) > 0$ and $\det(M)/\det(N) \neq 0$ ($\det(\ )$ is the determinant).

The methodology adopted for the ellipse fitting of the experimental points is the one proposed by Halir and Flusser, 1998. The known coefficients of Eq. 3.1 for each stage are then used to identify the center (x_0, z_0) and the semi–axes lengths (A, B) of the ellipse.

$$x_0 = \frac{cd - bf}{b^2 - ac} \tag{3.4}$$

3.3. The new method for accurate cross–section area and true stress computation

$$z_0 = \frac{af - bd}{b^2 - ac} \tag{3.5}$$

$$A = \sqrt{\frac{2\left(af^2 + cd^2 + gb^2 - 2bdf - acg\right)}{\left(b^2 - ac\right)\left(\sqrt{(a-c)^2 + 4b^2} - (a-c)\right)}} - 2 \cdot t \tag{3.6}$$

$$B = \sqrt{\frac{2\left(af^2 + cd^2 + gb^2 - 2bdf - acg\right)}{\left(b^2 - ac\right)\left(-\sqrt{(a-c)^2 + 4b^2} - (a-c)\right)}} - 2 \cdot t \tag{3.7}$$

with t, the thickness of the paint applied for the speckle.

In order to verify graphically the computed major and minor axis length, the experimental points $P_i(x,z)$ are translated in such a way that the center of the fitted ellipse is coinciding to the origin of the Cartesian coordinate system (0, 0).

$$P_i'(x,z) = P_i(x,z) - (x_0, z_0) \tag{3.8}$$

The counter clockwise angle of rotation (ϕ) from the x–axis to the major axis of the ellipse is define and computed (Eq. 3.9).

$$\phi = \begin{cases} 0 & \text{for } b = 0 \text{ and a} < \text{c} \\ 0.5\pi & \text{for } b = 0 \text{ and a} > \text{c} \\ 0.5\cot^{-1}\left(\dfrac{a-c}{2b}\right) & \text{for } b \neq 0 \text{ and a} < \text{c} \\ \dfrac{\pi}{2} + 0.5\cot^{-1}\left(\dfrac{a-c}{2b}\right) & \text{for } b \neq 0 \text{ and a} > \text{c} \end{cases} \tag{3.9}$$

Then, a rotation can be applied in order to obtain the major and minor axes aligned with the axes of the coordinate system. The rotational matrix is expressed as follows

$$R = \begin{bmatrix} \cos(\phi) & -\sin(\phi) \\ \sin(\phi) & \cos(\phi) \end{bmatrix} \tag{3.10}$$

Applying the rotation, the $P_i'(x,z)$ are expressed in the new frame: $P'' = RP'$ The area computed by fitting ellipses to the measured cross–section for the first stage is shown in Fig. 3.5.

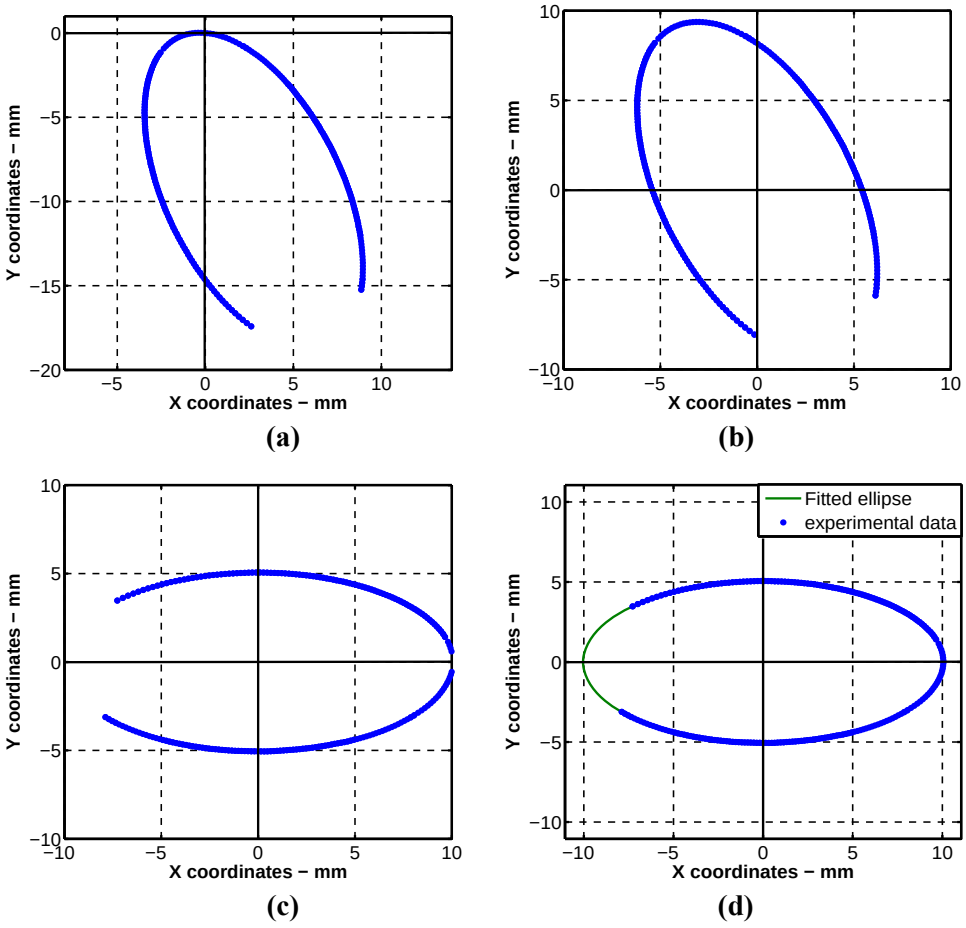

Figure 3.5. (a) The experimental points of the middle cross–section of compression specimens, (b) the translation, (c) the rotation and (d) the fitting of the ellipse for the minor and the major axis length computation.

In order to obtain stress–strain curves, strain (ε_{zz}) is computed by averaging the axial strain at the surface in the middle cross–section of the specimen (Fig. 3.6). Cauchy stress σ_{zz} is computed by using the force obtained from the load cell and the area computed by fitting ellipses at the middle cross–section of the specimen (Fig. 3.7). This Cauchy stress is

3.3. The new method for accurate cross–section area and true stress computation

compared with the stress computed by the load and the actualized area (Ac) obtained from volume conservation and neglecting barreling ($Ac=A_0$*exp(–ε_{zz})), where A_0 is the initial cross–section area.

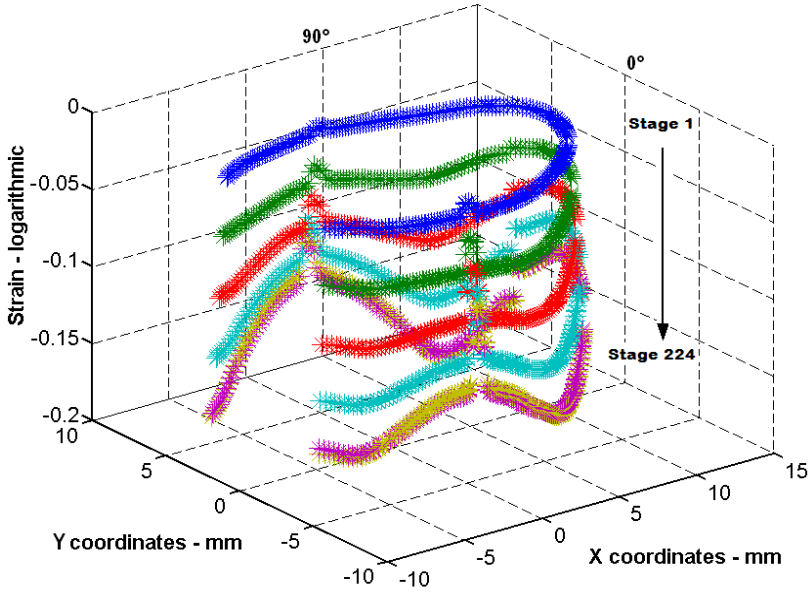

Figure 3.6. Axial strain distribution along the horizontal center line of the specimen (dashed line in Fig. 3.4).

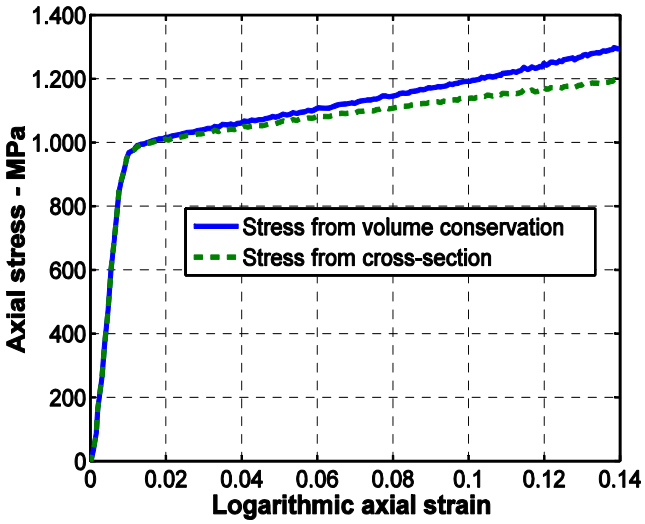

Figure 3.7. Stress strain curves for compression test performed at constant average strain rate equal to 10^{-3} s^{-1} with user-defined die displacement.

3.4. A new method for plastic anisotropy characterization of metals using the measured axial strain field

No–negligible inhomogeneous strain field on the surface of the specimen is found (experimental results obtained by 3–DIC presented in Fig. 3.3 and Fig. 3.6). This effect can be explained by the existence of variation on the measured barreling of the specimen and the plastic anisotropic of the alloy.

With the aim of understanding this behavior, numerical simulations of compression tests of elliptical cross–section specimens are performed. Two test conditions are considered: tests with and without friction for two materials, isotropic and anisotropic. The von Misses (VM) yield locus characterized from the current compression test data is used for the isotropic case. The anisotropic material is simulated by using CPB06 yield criterion proposed by Cazacu et al., 2006. The material parameters of the CPB06 model used for the simulations are the one obtained at the last stage of this research (parameter set in Table 4.3 (CPB03(4)). The description of the criterion, the identification procedure and material parameters are presented in details in Chapter 4. One–eighth of the compression specimen is modeled in the FE simulations within the updated Lagrangian FE code Lagamine developed by ArGEnCo Department of the University of Liège. The BWD3D finite element is selected. It is an 8–node 3D brick element with a mixed formulation adapted to large strains and large displacements. In order to simulate friction between the dies and the surface of the specimen for compression tests, 3D CFI3D contact elements (Habraken and Cescotto, 1998) with 4 integration points and a Coulomb friction law are chosen. The Coulomb friction coefficient Φ is considered to be constant. A value Φ = 0.08 is obtained by fitting the measured load and barreling with the prediction of the VM yield law (Fig. 3.8). The validation of the identified Φ value is done with the CPB06 model (Fig. 3.8).

The numerical and experimental axial strain distributions along the horizontal center line (dashed line) of the specimen are shown in Fig. 3.9. Simulation results show that when friction is not considered, homogeneous strain field is obtained for both, isotropic and anisotropic materials. Besides, when comparing the axial strain distribution obtained from simulated tests of isotropic and anisotropic materials including friction, it can be verified that closer inhomogeneous strain to experimental one is presented for the

anisotropic material than for the isotropic one. Therefore, it can be stated that the friction enhances the visualization of the anisotropic behavior of the material in a compression test with an elliptic cylinder.

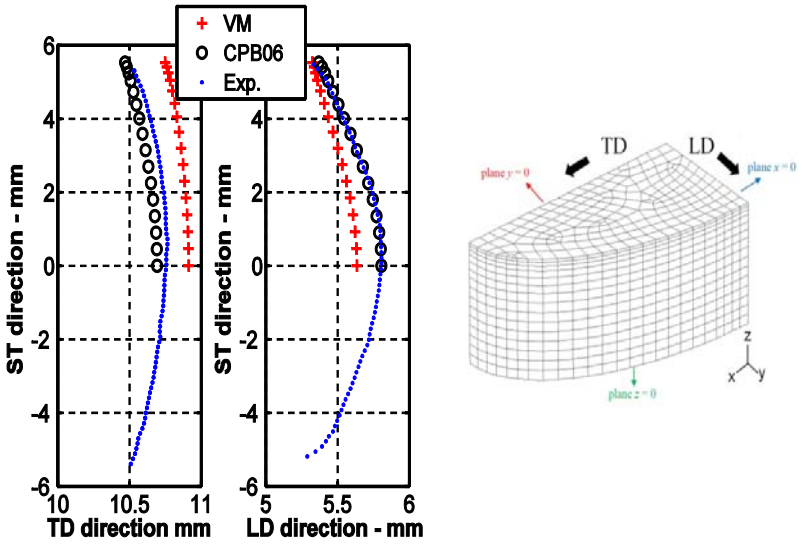

Figure 3.8. Barreling predictions by CPB06(4) and von Mises law compared to experimental measurements with optimal parameter set (Table 4.3) obtained by DIC in a compression test for the ST direction (Coulomb friction $\Phi = 0.08$).

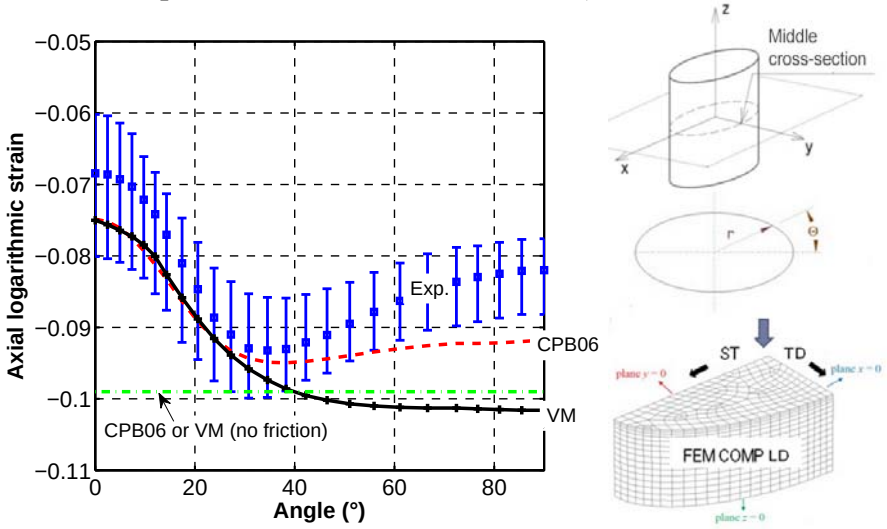

Figure 3.9. Assessment of the axial strain field predictions e_{zz} along the surface of the middle cross–section for a bulk TA6V alloy in a compression test for the LD direction.

The sensitivity of axial strain field to the plastic anisotropy is also verified by comparing numerical simulations of a strong anisotropic sheet (R_0=1.1 and R_{90}=2.2) of TA6V alloy with the bulk alloy investigated in this thesis. The set of material parameters of the sheet have been characterized by Gilles et al., 2011. From Fig. 3.10 it can be seen that the axial strain distribution of the sheet compression (CPB06 sheet) obtained by the simulation presents a very high inhomogeneous strain comparing to the bulk TA6V (CPB06)[§§]. From these results, it can be concluded that the axial strain distribution on the compression test including friction is sensitive to the plastic anisotropy of the alloys. However, this assumption should be further demonstrated with more experimental data.

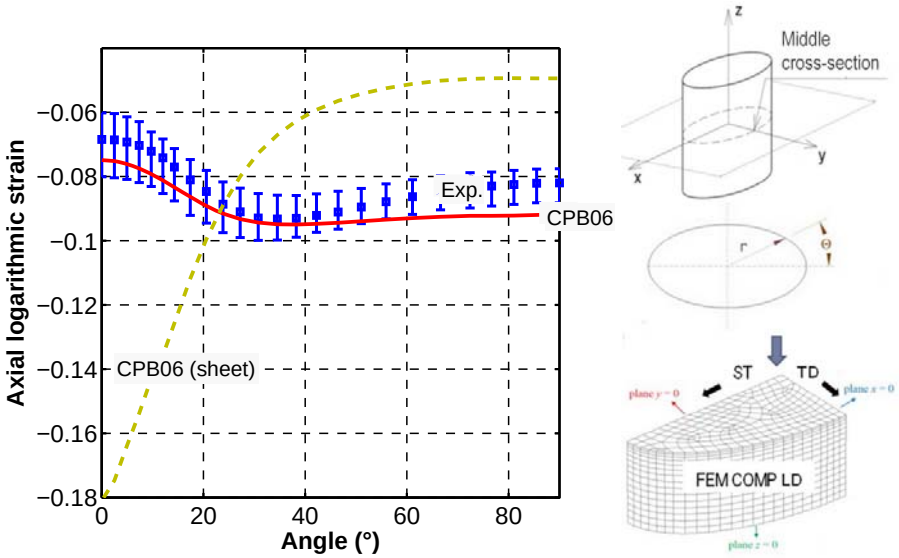

Figure 3.10. Assessment of the sensitivity of the axial strain e_{zz} to the plastic anisotropy of (along the surface of the middle cross–section) two TA6V alloys (bulk compression along LD direction and sheet compression in thickness direction).

[§§] For stack compression test of sheets the experimental results are not provided because of poor reliability due to non complete continuity between the sheet layers and strong scattering of measurement. This test is better described in Gilles, 2014.

3.4. A new method for plastic anisotropy characterization of metals using the measured axial strain field

Let us summarize the observations from previous simulations in Table 3.1 and Table 3.2.
:

Table 3.1. Effect of the friction on the axial strain distribution of compression tests.

Material	Friction	Characteristic of strain distribution
Isotropic	Yes	Inhomogeneous
	No	Homogeneous
Anisotropic	Yes	Inhomogeneous
	No	Homogeneous

Observation 1: Friction in compression tests influences the homogeneity of the axial strain field

Table 3.2. Sensitivity of the axial strain distribution to the anisotropy of the material on compression tests including friction.

Material	Strain range	Characteristic of strain distribution
Isotropic	[0.075; 0.1]	Weakly inhomogeneous
Anisotropic	[0.075; 0.095]	Weakly inhomogeneous with a different shape than isotropic case
Strongly anisotropic sheet	[0.05; 0.18]	Strongly inhomogeneous

Observation 2: Friction enhances the visualization of the plastic anisotropy through the axial strain field in compression tests.

3.5. Conclusion

In this work, an elliptic shape for bulk compression tests was used, with the main objective to apply it later on stack of sheets. The main advantage of this shape will be the simple way of alignment of the anisotropic directions of the sheet.

Besides, a reliable methodology was presented in order to accurately determine the evolution of the cross–section of cylindrical specimen by

using a 3D digital image correlation system. This methodology, leads to a more accurate stress computation than the methods available in the literature.

Experimental results revealed non–negligible inhomogeneous axial strain fields on the surface of the compression specimens including friction. The numerical investigations of bulk and sheet TA6V alloys demonstrated that this inhomogeneity is produced by a combination of the friction of the specimen with the dies and the plastic anisotropy of the material. This sensitivity of the axial strain to the plastic anisotropy is used in the Chapter 4 to improve the identification of the CPB06 material parameters. In addition, it is expected that this proposed specimen elliptical specimen is applied later to characterize the sheet metal anisotropy for layer compression tests.

3.6. References

Cazacu, O., Plunkett, B., Barlat, F., 2006. Orthotropic yield criterion for hexagonal closed packed metals. International Journal of Plasticity 22, 1171–1194.

Coppieters, S., Lava, P., Sol, H., Houtte, P., Debruyne, D., 2011. Determination of hardening behaviour and contact friction of sheet metal in a multi-layered upsetting test. Experimental and Applied Mechanics 6, Conference Proceedings of the Society for Experimental Mechanics Series, 733-739.

Gilles, G., Hammami, W., Libertiaux, V., Cazacu, O., Yoon, J.H., Kuwabara, T., Habraken, A.M, Duchêne, L., 2011. Experimental characterization and elasto–plastic modeling of the quasi–static mechanical response of TA–6V at room temperature. International Journal of Solids and Structures 48, 1277–1289.

Gilles, G., 2014. PhD thesis. Universiy of Liege, Belgium.

Halir, R., Flusser, J., 1998. Numerically Stable Least Squares Fitting of Ellipses. Proceedings of the International Conference in Central Europe on Computer Graphics and Visualization. WSCG '98: Plzen, Czech Republic, pp. 125–132.

3.6. References

Lecompte, D., Sol, H., Vantomme, J., Habraken, A.M., 2006. Analysis of speckle patterns for deformation measurements by digital image correlation. Speckle06, SPIE 6341.

Merklein, M., Kuppert, A., 2009. A method for the layer compression test considering the anisotropic material behavior. International Journal of Material Forming 2, 483–486.

Poortmans, S., Duchêne, L., Habraken, A.M., Verlinden, B., 2009. Modelling compression tests on aluminum produced by equal channel angular extrusion. Acta Materialia 57, 1821-1830.

Chapter 4. Anisotropy and tension–compression asymmetry predictions of the plastic response of bulk Ti–6Al–4V alloy at room temperature

This chapter is based on the submitted article:

Anisotropy and tension–compression asymmetry predictions of the plastic response of bulk Ti–6Al–4V alloy at room temperature

Authors: V. Tuninetti, G. Gilles, O. Milis, T. Pardoen, A.M. Habraken.

Journal: Submitted to International Journal of Plasticity (under–review)

The mechanical behavior of the Ti–6Al–4V alloy is characterized using, uniaxial compression implemented and defined in Chapter 3, uniaxial tensile, simple shear and plane strain tests in three orthogonal material directions. The experimental results reveal tension/compression asymmetry, anisotropic yielding and anisotropic hardening. These features are captured by an elasto–plastic constitutive law based on the macroscopic orthotropic yield criterion CPB06 adapted to hcp metals. The identification of the yield criterion is performed for different sets of experimental data. The sensitivity of the set of identified material parameters to the identification method is analyzed and the capacity of the model to accurately predict forces and displacement field is discussed. Lastly, a validation of the best set of identified CPB06 material parameters is performed by correlating the displacement/strain fields measured by 3D digital image correlation and computed by finite element simulations. The validation is carried out on notched round bars involving different initial stress triaxiality and on compression tests on elliptical cross–section specimens, both tests involving multiaxial strain fields and large deformations.

4.1. Introduction

The main aims of the current study presented in this Chapter are:

- The measurement of the quasi–static mechanical behavior of TA6V alloy at Room Temperature (RT) for different multi–axial stress states.
- The development of a methodology to identify the well–known macroscopic orthotropic yield criterion CPB06 developed by Cazacu et al., 2006.
- Te verification of the ability of FEM simulations using this model to predict loads and shape changes of the specimens due to plastic deformation during notched tensile tests or compression tests.

Numerous models have been applied to simulate the quasi–static behavior of TA6V. Some scientists even when strain rate range is not reaching dynamic state use Johnson Cook or Norton Hoff model to take into account strain rate sensitivity of TA6V alloy but neglect strength differential effect and plastic anisotropy (Kotkunde et al., 2014, Vanderhasten et al., 2008). Some authors are focused on damage prediction however assuming an isotropic behaviour. For instance Peirs, 2012 has investigated the fracture prediction of TA6V using either a Johnson–Cook damage initiation criterion combined with a progressive isotropic damage law or the Gurson model. Its TA6V alloy presents like the one studied here a true fracture strain of around 40%. Not surprisingly, Peirs experimentally observed that the number of voids strongly depends on triaxiality and is higher for uniaxial tensile tests than for plain strain and nearly inexistent in shear where shear localization often is the mechanism leading to rupture. Peirs confirmed that the void distribution in uniaxial tensile state is strongly heterogeneously distributed in the fracture zone, which justifies why coalescence of voids, resulting in cracks happens even for low void fraction of 0.5%. Lecarme exactly focused on the same material as the one studied in this thesis (same batch) and developed her own ductile damage model based. First, the Gologanu model for void growth and two versions of the Thomason criterion for coalescence were used, coupled to a Kocks–Mecking type hardening law. The void growth model was then extended to elasto–viscoplastic materials, and a void nucleation law was formulated based on a

criterion for the nucleation of new cavities, the configuration of the voids at nucleation and an evolution law of the porosity rate associated to nucleation. She measured by tomography void volume fraction of 0.57% for a uniaxial true strain of 0.7 in uniaxial state. A review of the constitutive models applied on TA6V incorporating strain rate, temperature, damage and anisotropic effects is beyond the scope of this thesis. The specific observations in the studied TA6V of relatively flat load–displacement curves, very quick softening near crack appearance, added to the former work of Peirs and Lecarme confirming quite low porosity levels before and even at rupture justify that an elasto–plastic model non–coupled with damage is investigated. The focus of this chapter is to check the ability of a phenomenological macroscopic anisotropic elasto–plastic law to predict TA6V plastic flow until equivalent strain in the range of [0; 0.35] equivalent strain (still before rupture in the stress states studied here). The model being identified by the part of tests before necking, its post–necking predictions are extrapolations so, their validity has to be verified.

Constitutive laws such as Khan–Huang–Liang (KHL) model (Khan and Liang, 1999) and its extensions (Khan and Yu, 2012, Khan et al., 2012) or CPB06 yield criterion developed by Cazacu et al., 2006 capture both the anisotropy due to texture evolution and the Strength Differential effect (SD). CPB06 was chosen for its flexibility. This phenomenological criterion is identified here from a set of monotonic tests: uniaxial tensile, uniaxial compression, simple shear and plane strain states performed on TA6V at RT and at low strain rate equal to 10^{-3} s^{-1}. The former ‘one step’ identification method proposed by Gilles et al., 2011 is replaced by a ‘two steps’ method integrating FEM inverse modeling and improving the accuracy. The anisotropic hardening behavior is described by linear interpolation of continuous CPB06 yield surfaces identified at several plastic work levels, which makes it possible to describe the different hardening rates in tension, compression and shear. Inverse modeling including uniaxial stress–strain curves in tension, plane strain, shear as well as Finite Element (FE) analyses of compression tests are used to adjust the material parameters. This identification method relies for instance on predicting the experimental axial strain distribution measured in the median cross–section of cylindrical compression specimens of initially elliptical cross–section measured by 3D digital image correlation (DIC) for three orthogonal material directions.

4.1. Introduction

Finally, the sensitivity of the different sets of identified material parameters to the identification method as well as the capacity of the model to accurately predict forces and displacement fields are discussed.

This research focuses not only on capturing the SD and anisotropy of TA6V alloy observed in monotonic stress–strain curves, but also on verifying that FE simulations can accurately reproduce the load and shape changes of the specimens subjected to multiaxial loading and large plastic strains.

This chapter is organized as follows:

- Section 2 describes the experimental framework used to perform the tests as well as the features of the alloy investigated.
- Section 3 presents the quasi–static behavior of TA6V at room temperature obtained from the experimental results.
- Section 4 introduces the CPB06 orthotropic yield criterion and the identification procedure adopted. The comparisons of the analytical predictions with experimental uniaxial stress–strain curves used for the identification are also presented.
- Section 5 focuses on the evaluation of the predictions of the identified CPB06 model by correlating the load–displacement curves and the shape evolution of the tested specimens involving different stress triaxialities.
- In section 6, the overall conclusions are highlighted.
- Lastly, Appendix B describes the viscoplastic correction of stress strain curves and in Appendix C the Bauschinger effect is quantified.

4.2. Material and experimental procedures at RT

Compression, tension, shear and plane strain specimens were machined from an initial bulk piece of TA6V alloy with the dimensions shown in Fig. 4.1. Both tensile and compression tests are performed in three orthogonal material directions: Longitudinal (LD), Transverse (TD) and Short Transverse (ST), shear, Bauschinger and plane strain tests are applied in ST–LD plane. Due to the high strain rate and temperature sensitivity of this hcp alloy in quasi–static loading, the tests are performed at room temperature and the targeted strain rate is a constant value equal to 10^{-3} s^{-1}.

Chapter 4. Anisotropy and tension–compression asymmetry predictions of the plastic response of bulk Ti–6Al–4V alloy at room temperature

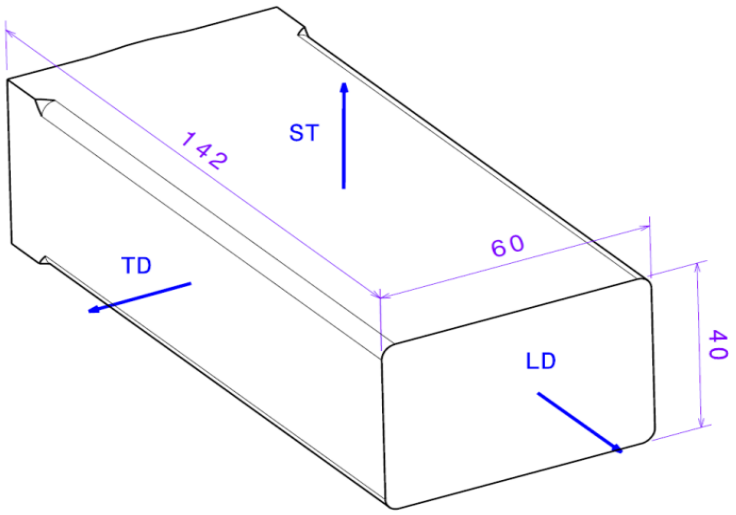

Figure 4.1. Material directions of the studied bulk piece of TA6V (dimensions in mm).

4.2.1. Material

TA6V is a α–β–type alloy with β transus temperature about 996 °C. The aluminum alloying element stabilizes the α (hcp) phase, i.e., increases the temperature at which this α phase is stable. On the other hand, vanadium alloying is β (bcc) stabilizer which results in stability of the β phase at lower temperatures (Donachie, 2000). The bulk TA6V alloy investigated in this thesis has a chemical composition given in Table 4.1. The hcp α–phase represents 94% of the volume. Optical microscopy showed that the material has slightly elliptical grains and that the mean grain size is equal to 12 µm in the ST–LD plane and 9µm in ST–TD plane (Lecarme, 2013). Fig. 4.2 was determined by X–ray diffraction (XRD) at Paris–13 University. The initial texture is quite weak.

Table 4.1. Chemical composition of the TA6V alloy.

Al	V	Fe	N	O	C	Ti
6.1	4.0	0.3	0.05	0.20	0.08	Bal.

4.2. Material and experimental procedures

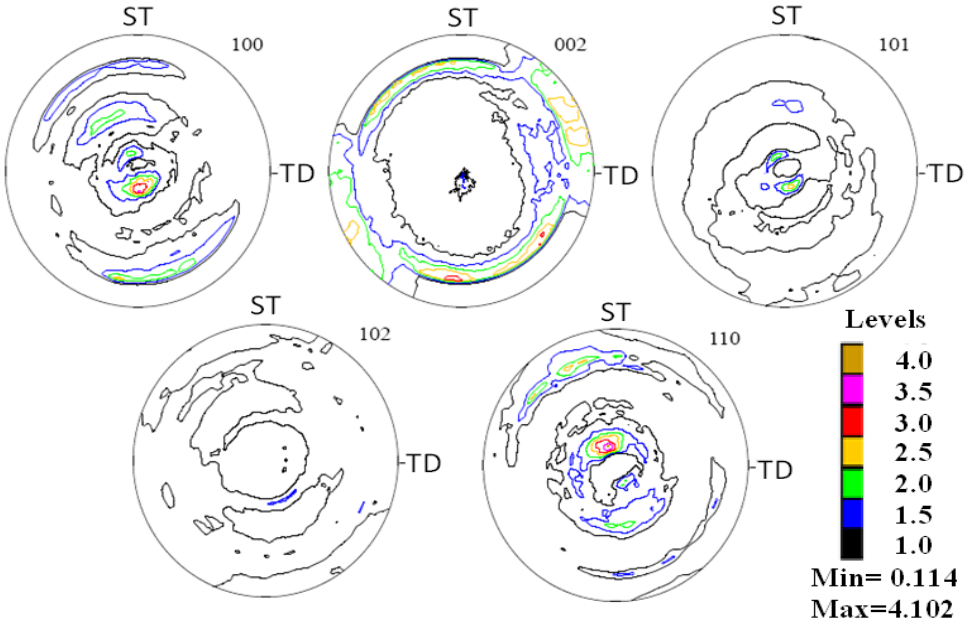

Figure 4.2. Initial texture of the investigated TA6V alloy.

4.2.2. Compression tests

Specimens were machined by wire electron discharge machining (EDM) with the dimensions shown in Fig. 4.3(a). The experiments are performed in three orthogonal material directions: LD, TD and ST. The servo hydraulic axial testing machine is controlled in order to impose constant strain rates equal to 10^{-3}, 10^{-2}, and 10^{-1} s^{-1}. Three 3D optical measurement systems (6 CCD cameras) are used and the strain/displacement fields are measured for characterization and validation purposes (Fig. 4.3(b)). Due to friction, a slight barreling is observed and true uniaxial state is not reached. Stress–strain curves are computed by the method proposed by Tuninetti et al., 2012a and described in Chapter 3. The cross–section of the specimen is obtained by fitting an ellipse with the experimental data. The average true axial stress is computed by dividing the load measured by the load cell with the current cross–section area. The true average axial strain is obtained by averaging the axial strain measured on the surface of the horizontal symmetric plane of the sample.

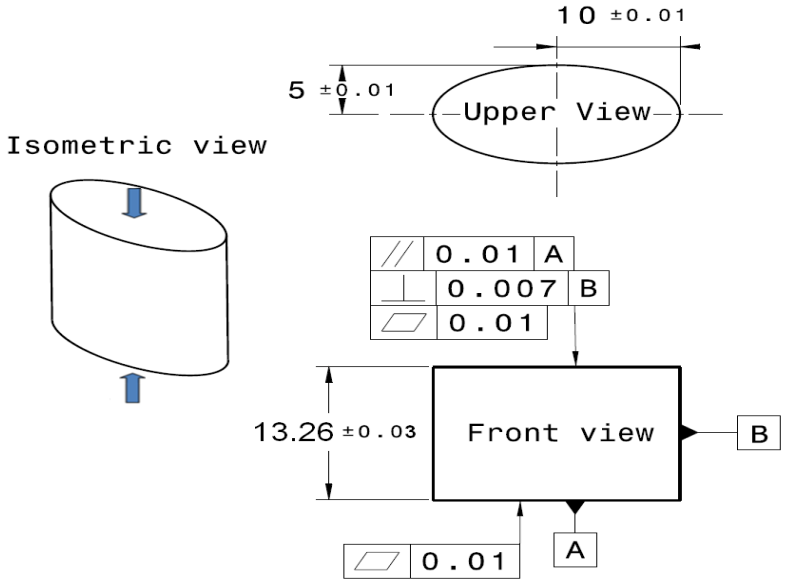

(a)

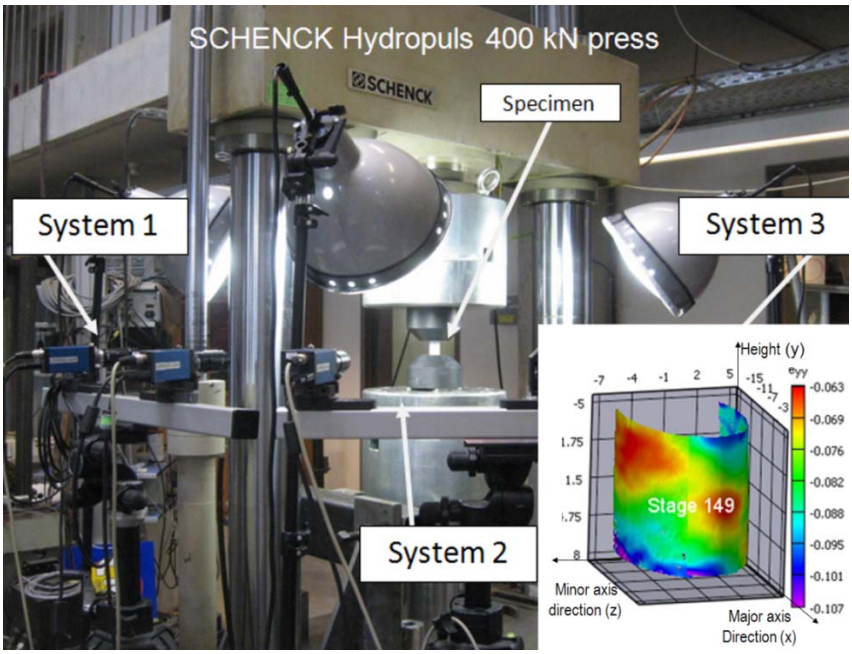

(b)

Figure 4.3. Compression tests; (a) geometry and dimensions of specimens in mm. (b) DIC system of 6 cameras provides axial strain fields.

4.2. Material and experimental procedures

4.2.3. Uniaxial tensile tests

Axisymmetric specimens of 6 mm diameter for the LD direction are tested at a constant strain rate equal to 10^{-3} s^{-1} using a universal testing machine (electro–mechanic Press ZWICK 100 kN) and three 3D–DIC systems are used for the strain/displacement measurements. By using the cross–section evolution of the tensile samples measured by DIC, a parameter similar to the "Lankford" coefficient used for sheets is computed. It is defined as the ratio of the strain rates in the TD direction and in the ST direction, i.e. $R_{LD} = \dot{\varepsilon}_{TD} / \dot{\varepsilon}_{ST}$ with $\dot{\varepsilon}_{TD} = \ln(b/r)/t$, $\dot{\varepsilon}_{ST} = \ln(a/r)/t$, and where r is the initial radius of the sample and a, b are the major and minor axis lengths of the current elliptical cross–section of the specimen, while t is the time. As accurate sections are measured during the entire duration of the test, the average value of axial stress could be computed even after the onset of necking. However as such information was not available in TD and ST directions, it was decided to only use the pre–necking part of the curve. Applying the Considère criterion, the load–displacement curve is identified until the earliest possible necking.

The tensile tests in the TD and ST directions are performed on axisymmetric specimens of 4 mm in diameter using a Zwick universal testing machine equipped with a digital axial extensometer (Lecarme, 2013). The section is estimated by assuming volume conservation until the onset of necking identified by the Considère criterion. The machine is piloted in order to keep a constant cross–head speed. The stress strain curves obtained for average plastic strain rates equal to $7\text{x}10^{-4}$ s^{-1} for the TD and $9\text{x}10^{-5}$ s^{-1} for the ST direction are transformed into the corresponding response at a rate of 10^{-3} s^{-1} using the Johnson–Cook (JC) viscoplastic model (see Appendix B.1). The material parameters dictating the rate dependency where indeed previously identified from compression tests at different strain rates in the LD direction (Tuninetti et al., 2012b). This minor correction is applied in order to identify the anisotropic yield locus at exactly the same strain rate (10^{-3} s^{-1}) in order to get rid of all possible viscosity effect.

4.2.4. Simple shear, Bauschinger and plane strain tests

The tests are carried out on the specimens shown in Fig. 4.4 with the biaxial machine developed and validated by Flores et al., 2005 at the University of Liège. This machine uses vertical and horizontal actuators which control the displacement of the grips. These actuators are controlled in displacement at a constant speed in order to reach plastic strain rates between $1x10^{-3}$ and $2x10^{-3}$ s^{-1} and elastic strain rates from $1x10^{-4}$ to $4x10^{-4}$ s^{-1}. Two 3D–DIC systems are used for strain/displacement measurements. The true stress for plane strain tests is computed with the method proposed by Flores et al., 2010. This new accurate computational method uses the experimental data while including the edge effect evolution as a function of plastic strain. In the case of current shear tests, the edge effect is negligible and the shear stress can be accurately computed using: $\tau=F/A_0$, where F is the load and A_0 is the initial cross–section of the specimen.

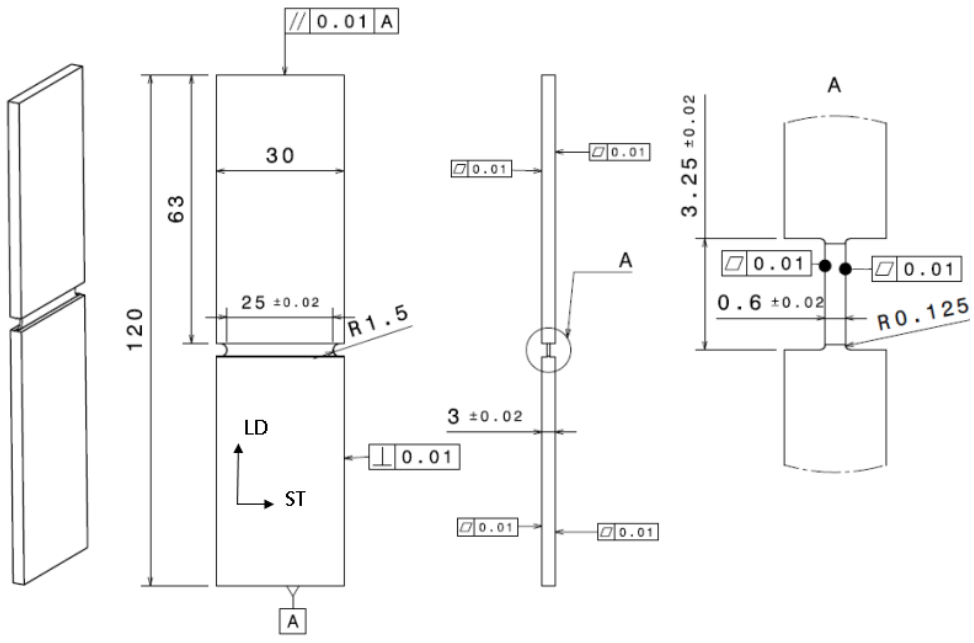

Figure 4.4. Geometry and dimensions of plane strain, shear and Bauschinger specimens (dimensions in mm).

4.3. Experimental results

The average initial yield stress and the Young's modulus are shown in Table 4.2 with the standard deviations. The alloy involves anisotropic elastic properties at room temperature. Similar results were already published by Olsen and Moreen, 1973, Lanning et al., 2005 and Oldenber et al., 2012 and explained by cylindrical symmetry of the hcp crystal structure (Tromans, 2011). For many materials, the Young's modulus in tension is found different from the Young's modulus in compression and it has to be derived from test data obtained in the stress mode of interest, as proposed by ASTM, 2010. These elastic properties were mainly determined in this work using quasi–static uniaxial tension and compression tests with loading/unloading cycles near the onset of plasticity under constant strain rate of 10^{-3} s^{-1}. For the FE simulations described later, the apparent Young's modulus related to tension or compression state in the test direction (see Table 4.2) is used. Using a simple average Young modulus value induces discrepancy in the measured and predicted load–displacement curves (Figures 4.11, 4.15 and 4.16). The small difference between the Young's modulus in tension and in compression can presumably be explained by the asymmetry in the interatomic potential. This asymmetry leading to larger stiffness in compression compared to tension shows up only for sufficiently large elastic strains. As the elastic strains reached in Ti alloys are indeed on the order of + or – 1 % due to the large strength and relatively low modulus.

Fig. 4.5 gathers all the available curves (See Appendix 5.B.1 for the correction of the ST and TD tensile curves) at 10^{-3} s^{-1} strain rate and RT, based on an average experimental curve for each loading direction and loading condition. The material response of TA6V demonstrates a significant strength asymmetry between tension and compression. Anisotropic hardening is found and is observed to be stronger in compression compared to tension. Usual Lankford coefficient, used in sheet plane to measure anisotropic behaviour, has to be adapted for this bulk material. The so called "R value" in tension and LD direction is measured during the tests by DIC identifying the evolution of the radii of elliptic minimal cross–section. This value for the axial strain range [0, 0.1] was nearly constant and its average value will be used hereafter: $R_{LD} = \dot{\varepsilon}_{TD} / \dot{\varepsilon}_{ST} = 1.15.$

Chapter 4. Anisotropy and tension–compression asymmetry predictions of the plastic response of bulk Ti–6Al–4V alloy at room temperature

Often, isotropic hardening is related to an increase of the dislocation density during plasticity and can be modeled by a simple homothetic expansion of the yield locus. Here, the hardening behavior is more complex. As already observed by Lou et al., 2007 and Nixon et al., 2010, the hardening rate in the TA6V alloy is different in tension and in compression. It varies with the loading direction as well (Fig. 4.5). For this reason, in the next section, the fitting of the CPB06 yield locus with the monotonic experimental stress–strain data for several plastic work levels will take into consideration the updating of the shape of the yield criterion. The texture evolution and the effect of twinning are the primary reasons for these macroscopic observations.

Table 4.2. Experimental Young's modulus and yield stress.

test	Direction	Strain rate s^{-1}	Young's Modulus E GPa / Std. Dev.	Yield Strength σ_0 MPa (0.2% plastic strain) / Std. Dev.
Tension	LD	10^{-3}	111±1	927±3
	TD	10^{-3}	115±4	933±1
	ST	10^{-3}	117±1	941±4
Compression	LD	10^{-1}	127±3	1013±5
		10^{-2}	125±4	986±4
		10^{-3}	122±1	968±3
	TD	10^{-3}	128±3	1040±6
	ST	10^{-3}	123±3	1002±5

4.3. Experimental results

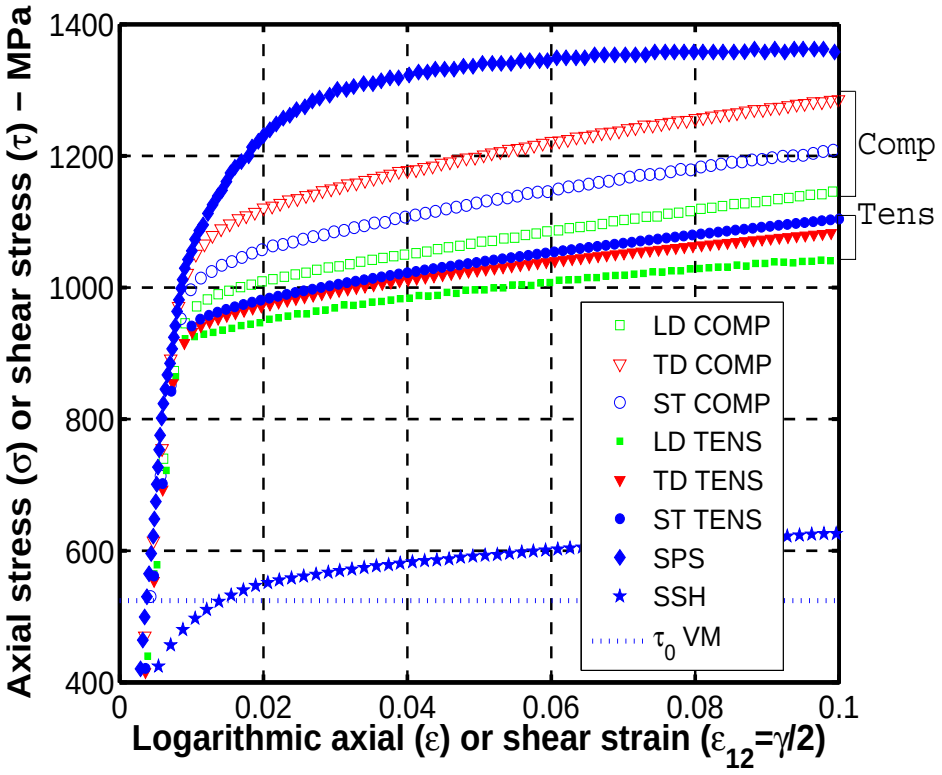

Figure 4.5. True stress strain curves for monotonic tensile and compression in three orthogonal material directions (LD, TD and ST), plane strain (SPS in LD–ST plane), and shear (SSH in LD–ST plane) at 10^{-3} s^{-1} and at RT.

4.4. Constitutive model and identification procedure

4.4.1. The CPB06 orthotropic yield criterion

The macroscopic orthotropic yield criterion CPB06 proposed by Cazacu et al., 2006 and Plunkett et al., 2006, was selected in this study, as it describes both the tension/compression asymmetry and the anisotropic behavior. This criterion is defined by:

$$F_1 = \left(|\Sigma_1| - k\Sigma_1\right)^a + \left(|\Sigma_2| - k\Sigma_2\right)^a + \left(|\Sigma_3| - k\Sigma_3\right)^a \qquad (4.1)$$

where k is a parameter which takes into account the strength differential effect (SD), a is the degree of homogeneity, Σ_1, Σ_2, Σ_3 are the principal values of the tensor $\boldsymbol{\Sigma}$ defined by $\boldsymbol{\Sigma} = \mathbf{C} : \mathbf{S}$ where $\mathbf{C}$ is a fourth–order orthotropic tensor that accounts for the plastic anisotropy of the material and $\mathbf{S}$ is the deviator of the Cauchy stress tensor. The tensor $\mathbf{C}$ represented as Voigt notations is defined as follows:

$$\mathbf{C} = \begin{bmatrix} C_{11} & C_{12} & C_{13} & 0 & 0 & 0 \\ C_{12} & C_{22} & C_{23} & 0 & 0 & 0 \\ C_{13} & C_{23} & C_{33} & 0 & 0 & 0 \\ 0 & 0 & 0 & C_{44} & 0 & 0 \\ 0 & 0 & 0 & 0 & C_{55} & 0 \\ 0 & 0 & 0 & 0 & 0 & C_{66} \end{bmatrix} \tag{4.2}$$

A methodology that allows describing directional hardening which accounts for the distortion of the yield locus of hexagonal materials has been proposed by Plunkett *et al.,* 2006. It consists in determining the anisotropy coefficients corresponding to several fixed levels of accumulated plastic strain and then use a piece–wise linear interpolation to obtain the yield surface corresponding to any level of accumulated plastic strain. Gilles et al., 2011 have used a similar methodology where the plastic work is used instead of the accumulated plastic strain. This second methodology is adopted here. The updated yield locus is described by

$$f\left(\boldsymbol{\sigma}, \bar{\varepsilon}_p\right) = \bar{\sigma}\left(\boldsymbol{\sigma}, \bar{\varepsilon}_p\right) - Y\left(\bar{\varepsilon}_p\right) \tag{4.3}$$

where $\bar{\sigma}$ is the equivalent stress according to the given yield criterion in Eq. (4.1) while $\bar{\varepsilon}_p$ is the equivalent plastic strain associated to $\bar{\sigma}$ using the work–equivalence principle (Hill, 1987), and $Y\left(\bar{\varepsilon}_p\right)$ is a reference hardening curve (the tensile stress–strain curve along LD direction is adopted in this study). The form of the latter is chosen as $Y\left(\bar{\varepsilon}_p\right) = A_0 + B_0\left[1 - \exp\left(-C_0\bar{\varepsilon}_p\right)\right]$, where A_0, B_0, C_0 are material constants. For any $\bar{\varepsilon}_p$, the plastic work per unit volume is given by

4.4. Constitutive model and identification procedure

$$W_p\left(\bar{\varepsilon}_p\right)=\int_0^{\bar{\varepsilon}_p} Y(p)dp=\left(A_0+B_0\right)\bar{\varepsilon}_p-\frac{B_0}{C_0}\left(1-\exp\left(-C_0\bar{\varepsilon}_p\right)\right). \tag{4.4}$$

The anisotropy coefficients and SD parameters are considered to evolve as a function of the plastic work per unit volume W_p. They are determined for several levels of W_p: $W_p^{(1)}<\ldots<W_p^{(j)}<\ldots<W_p^{(m)}$, $j=i..m$, where $W_p^{(1)}$ corresponds to initial yielding and $W_p^{(m)}$ corresponds to the highest level of plastic work attained in the tests. Next, for each of the individual plastic work levels, $W_p^{(j)}$, $\bar{\sigma}$ is calculated using Eq. (4.1). The determination of the yield surface corresponding to an intermediate level of plastic work ($W_p^{(j)}\le W_p\le W_p^{(j+1)}$) is made by a linear interpolation.

4.4.2. Identification procedure

The anisotropy coefficients C_{ij} and SD parameters *k* of the CPB06 yield criterion are fitted on experimental yield stress ratios and R–ratios using the Simulated Annealing (SA) algorithm (Metropolis *et al.,* 1953, Hastings, 1970). This is a global optimization method that distinguishes between different local optima. In this study, the error function to be minimized is defined as follows:

$$E=\sum_{i=1}^{r}\eta_i\left[\frac{\left(\sigma_D^T/\sigma_{LD}^T\right)_i^{\text{num}}}{\left(\sigma_D^T/\sigma_{LD}^T\right)_i^{\text{exp}}}-1\right]^2+\sum_{j=1}^{s}\eta_j\left[\frac{\left(\sigma_D^C/\sigma_{LD}^T\right)_j^{\text{num}}}{\left(\sigma_D^C/\sigma_{LD}^T\right)_j^{\text{exp}}}-1\right]^2+\sum_{k=1}^{t}\eta_k\left[\frac{\left(\sigma_D^{SPS}/\sigma_{LD}^T\right)_k^{\text{num}}}{\left(\sigma_D^{SPS}/\sigma_{LD}^T\right)_k^{\text{exp}}}-1\right]^2+\ldots \tag{4.5}$$
$$\ldots+\sum_{l=1}^{u}\eta_l\left[\frac{\left(\sigma_D^{SSH}/\sigma_{LD}^T\right)_l^{\text{num}}}{\left(\sigma_D^{SSH}/\sigma_{LD}^T\right)_l^{\text{exp}}}-1\right]^2+\sum_{m=1}^{v}\eta_m\left[\frac{r_m^{\text{num}}}{r_m^{\text{exp}}}-1\right]^2$$

where *r, s, t, u* and *v* are respectively the number of tensile, compressive, plane strain, shear yield stresses, and available R–ratios. The superscript indicates whether the value is experimental (exp) or numerical (num). Parameters $\eta_{i,j,k,l,m}$ are used to balance the weight of each term. In the current identification, uniaxial tensile and compression tests were available in the three directions RD, TD, ST, while plane strain and shear tests and R–

ratio are only available in LD direction. This first identification step provides an initial set of parameters that requires further adjustments.

Starting from this first set of material parameters, inverse modelling of the compression tests provides a second refined set of parameters. This second identification step compares the predicted response with the experimental axial strain distribution measured in the median cross–section of the specimen by 3D–DIC for LD, TD and ST directions. This second identification is essential as this axial strain distribution is very sensitive to the material anisotropy as seen in Chapter 3 (Tuninetti et al., 2012a). One–eighth of the specimen is modeled in the FE simulations within the updated Lagrangian FE code Lagamine developed by ArGEnCo Department of the University of Liège. The BWD3D finite element is selected. It is an 8–node 3D brick element with a mixed formulation adapted to large strains and large displacements. It uses a reduced integration scheme (with only one integration point) and an hourglass control technique. This element is based on the nonlinear three–field (stress, strain and displacement) HU–WASHIZU variational principle (Belytschko and Bindeman, 1991, Duchêne et al., 2007, Simo and Hughes, 1986). In order to simulate friction between the dies and the surface of the specimen for compression tests, 3D CFI3D contact elements (Habraken and Cescotto, 1998) with 4 integration points and a Coulomb friction law are chosen. The Coulomb friction coefficient Φ is considered to be constant. A value $\Phi = 0.08$ is obtained by fitting the measured and predicted barreling. Finally, these two identification steps provide a material parameter set based on compression and tension tests in three directions (LD, TD, ST), shear, plane strain tests and R_{LD} value for 5 plastic work levels and imposing the constraint $C_{44}=C_{55}=C_{66}$ (Table 4.3).

The CPB06 constitutive model identified by the above procedure (the results of other identification strategies will be addressed in the next section) is used to predict experimental results, as shown in Figs. 4.6, 4.7 and 4.8. Fig. 4.6 shows the yield surfaces along with the experimental points (discrete symbols) for 5 levels of plastic work. Three 2D cuts of the yield surface are presented (LD–TD, LD–ST and TD–ST) as well as the π–plane projection. Note that irrespective of the level of plastic work, the yield loci exhibit a distorted elliptical shape. The agreement between the model and experiments is quite satisfactory.

4.4. Constitutive model and identification procedure

Table 4.3. Coefficients of CPB06 yield function for TA6V and for 5 plastic works levels (a = 2, C_{11} = 1 and $C_{44} = C_{55} = C_{66}$) and values of $Y\left(\bar{\varepsilon}_p\right)$ identified in tension along LD direction.

W_p	k	C_{12}	C_{13}	C_{22}	C_{23}	C_{33}	C_{44}
3	–0.136	–2.373	–2.364	–1.838	1.196	–2.444	–3.607
9.38	–0.136	–2.495	–2.928	–2.283	1.284	–2.446	4.015
48.7	–0.165	–2.428	–2.920	1.652	–2.236	1.003	–3.996
100.2	–0.164	–2.573	–2.875	1.388	–2.385	0.882	–3.926
206.6	–0.180	–2.973	–2.927	0.534	–2.963	0.436	–3.883
LD Tension		A_0=921.0		B_0=160.0		C_0=15.48	

In order to analyze the plastic anisotropy predictions of the CPB06 model, the strain field predictions of compression tests in LD, TD and ST directions were also compared with the experimental results in Fig. 4.7 which provides the variation of the axial strain (along the surface of the middle cross–section of the compression samples) with the theta angle. The strain distribution is well predicted but with a slight discrepancy in the ST direction.

Finally, Fig. 4.8 shows the experimental stress–strain curves along with the model predictions. Except for the compression in the TD direction, the predictions are consistent with the experiments. The different curves for both tension and compression in three directions (LD, TD and ST) clearly confirm that the von Mises isotropic approach is insufficient to describe the mechanical behaviour of the TA6V alloy. The linear parts observed within the predicted curves in Fig. 4.8 reminds that the hardening behavior is related to interpolation between different yield locus shapes identified for five plastic work levels.

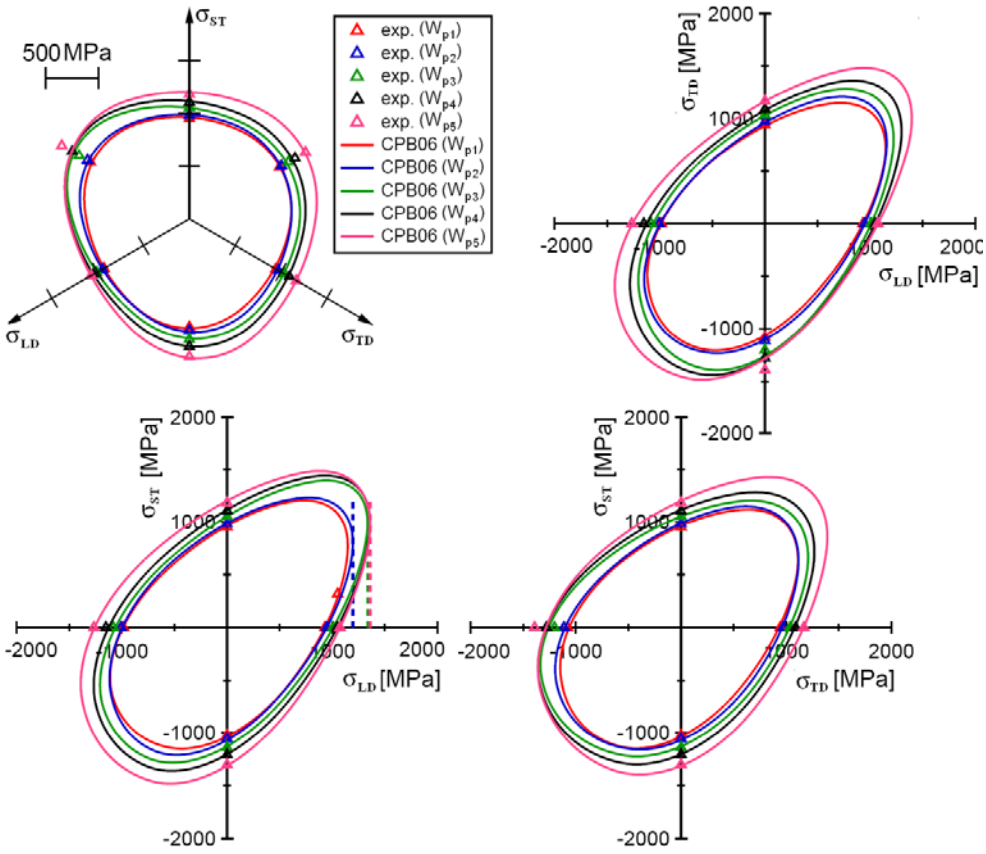

Figure 4.6. Yield loci predicted by CPB06 and experimental points (exp.) for 5 accumulated plastic works: W_{p1}= 1.86, W_{p2}=9.38, W_{p3}=48.7, W_{p4}=100.2 and W_{p5}=206.6 J/cm^3.

4.4. Constitutive model and identification procedure

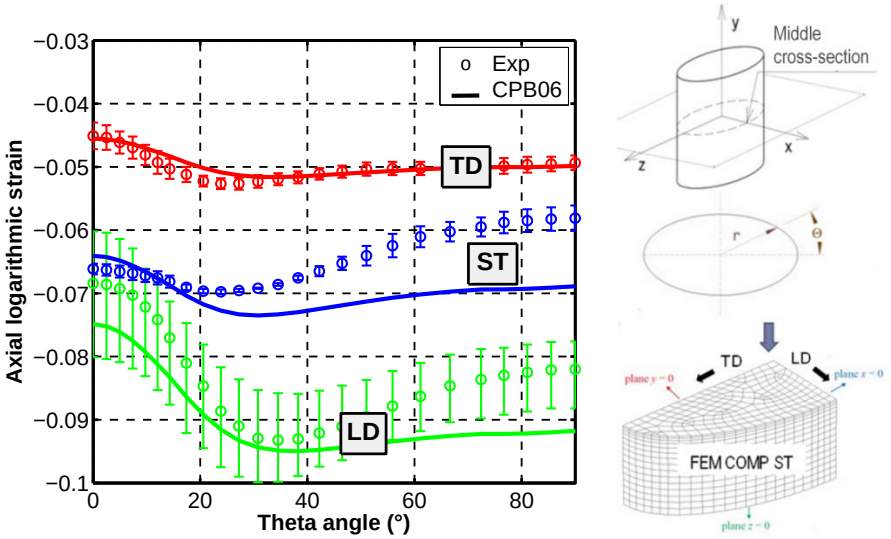

Figure 4.7. Experimental (DIC) and CPB06 predictions of axial strain distribution along the surface of the middle cross–section of compression samples for LD at ε_{axial}=0.08, TD at ε_{axial}=0.05 and ST at ε_{axial}=0.065 (axial strain levels are selected for a 200 kN of axial load).

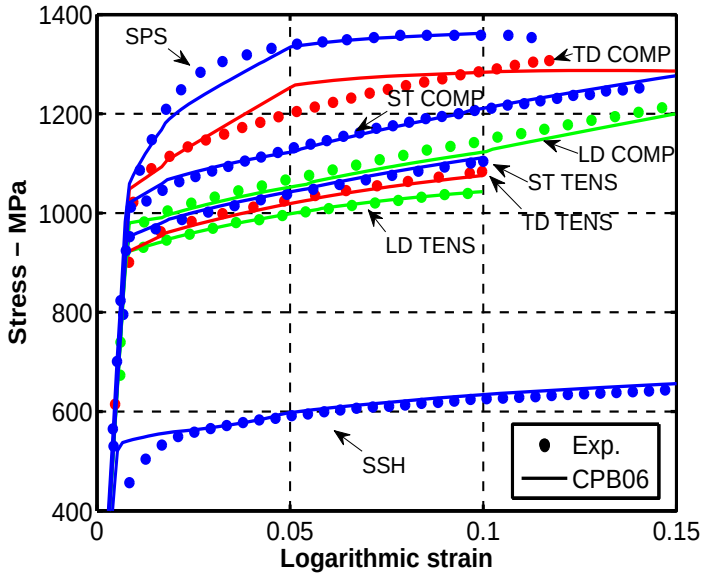

Figure 4.8. Experimental (Exp.) and CPB06 predictions of stress–strain curves in tension (TENS) and in compression (COMP) for the LD, TD and ST directions, plane strain LD–ST (SPS) and shear (SPS) LD–ST.

4.5. Application and validation of the identified CPB06 model

Tensile tests on notched specimens with two geometries R1.5 and R5 (Fig. 4.9) and a compression test on elliptical cross–section specimen (Fig. 4.3(a)) are used in order to validate the identified CPB06 model. These geometries are chosen in order to validate the CPB06 model on different stress states. For instance, Fig. 4.10 confirms a different initial and "final" (for axial strain near fracture) triaxiality distributions along the radius of the minimal cross section for both notched specimen. Note that the triaxiality is defined as the ratio of the mean stress to the equivalent stress according to the CPB06 criterion (Eq. 4.1). The numerical simulations are run within the updated Lagrangian FE code Lagamine already introduced in the previous section.

In Fig. 4.10 (a) and (b), the load as a function of the displacement for a 40 mm gauge zone and the experimental cross–section of the geometry R1.5 just before fracture measured by 3D–DIC are compared with the predictions of the CPB06 model based on 4 different material parameter sets identified with different choices of experimental test data and the two step identification method of previous section CPB06(4):

1. Initial CPB06 yield locus identified with compression and tension tests for LD, TD and ST with Voce type hardening law (isotropic hardening, the shape evolution of the yield criterion is neglected); under the name CPB0(1);

2. Initial CPB06 yield locus identified with compression and tension tests for LD, TD and ST, shear and plane strain tests with Voce type hardening law; under the name CPB0(2);

3. CPB06 identified with compression and tension tests for LD, TD and ST, shear, plane strain tests and $R_{LD}=1.15$ value for 5 plastic work levels; under the name CPB0(3);

4. CPB06 identified with compression and tension tests for LD, TD and ST, shear, plane strain tests and $R_{LD}=1.15$ value for 5 plastic work levels and imposing $C_{44}=C_{55}=C_{66}$ (data set used for Fig. 4.7 to 4.9), under the name CPB0(4).

4.5. Application and validation of the identified CPB06 model

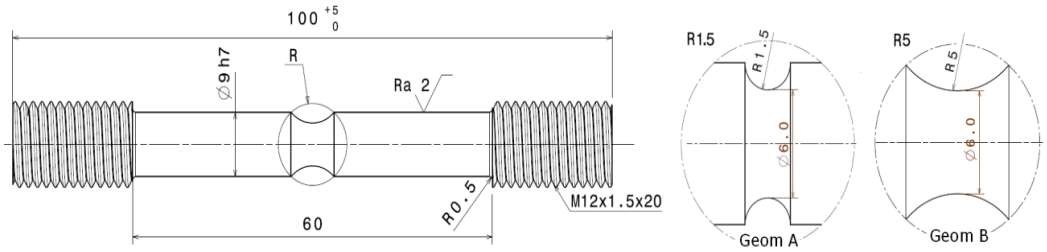

Figure 4.9. Specimen geometries R1.5 and R5 for notched tensile tests (dimensions in mm).

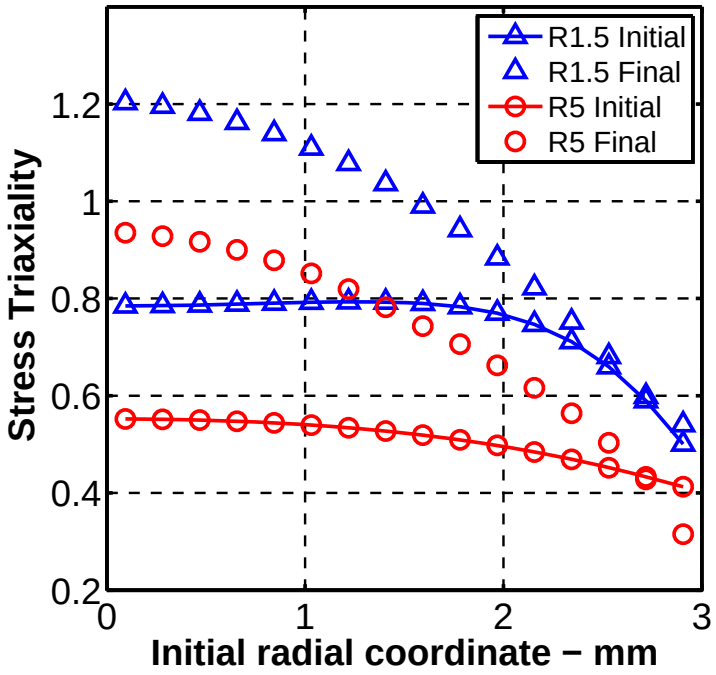

Figure 4.10. Triaxiality distribution along the radius of the minimal cross section for notched tensile tests geometries R1.5 and R5 at initial and final stage. The axial displacement at the final stage is equal to 0.8 mm for geometry R1.5 and 1 mm for geometry R5.

The results (Fig. 4.11) show that the identifications with the highest number of monotonic tests (CPB06(3) and CPB06(4)) better reproduce both the load prediction and the shape of the deformed cross–section of the

sample. However, the constraint of $C_{44}=C_{55}=C_{66}$ used for identification CPB06(4) is needed in order to insure an accurate prediction of the load evolution. This constraint could be relaxed if shear tests for each material direction were available. Note that for this specific notch geometry loaded in LD direction and reaching limited axial strain, isotropic elasto–plastic von Mises law fitted on tensile tests in this direction predicts quite well both load and average radius. However, as presented hereafter, the second notch geometry, smoother and allowing a larger plastic deformation before fracture confirms that even for tensile in LD direction the von Mises law is not adapted as non negligible plastic strain anisotropy experimentally appeared (see Fig. 4.12(a)).

The second tensile tests on specimens with a medium sharp notch radius (geometry R5: reaching a maximum stress triaxiality of 0.93 near fracture while previous notch R1.5 reached 1.2) have also been simulated. The section before fracture (Fig. 4.13(b)) involves a much larger distortion toward an elliptical shape compared to R1.5 (See Fig. 4.11(b)) confirming that the von Mises (VM) isotropic approach is clearly insufficient. The results obtained from FEM by using the CPB06(3) and CPB06(4) are compared to the experimental measurements in Fig. 4.12 to Fig. 4.14. Inhomogeneous strain (Fig. 4.12(a) and Fig. 4.13(a)) fields and elliptical cross–section (Fig. 4.13b) were found just before fracture. These data were measured by DIC and are properly predicted by the CPB06 model identified with both sets of parameters and with an improved accuracy for set 3 (Fig. 4.12 and Fig. 4.13). The notch shape of the specimen just before fracture was also assessed in Fig. 4.14. and is close to DIC measurements. Load vs. axial displacement comparisons shown in Fig. 4.15 reveals that imposing the constraint $C_{44}=C_{55}=C_{66}$ is less important, however CPB06(4) is still more accurate. This smaller effect is due to the strain field within the specimen which is subjected to less shear when the notch is smoother. It is worth noting that cross–section geometry predictions just before fracture should have been computed using a coupled–plasticity damage model. Nevertheless, it is worth investigating how the predictions compare with experimental data when the damage effects are neglected.

4.5. Application and validation of the identified CPB06 model

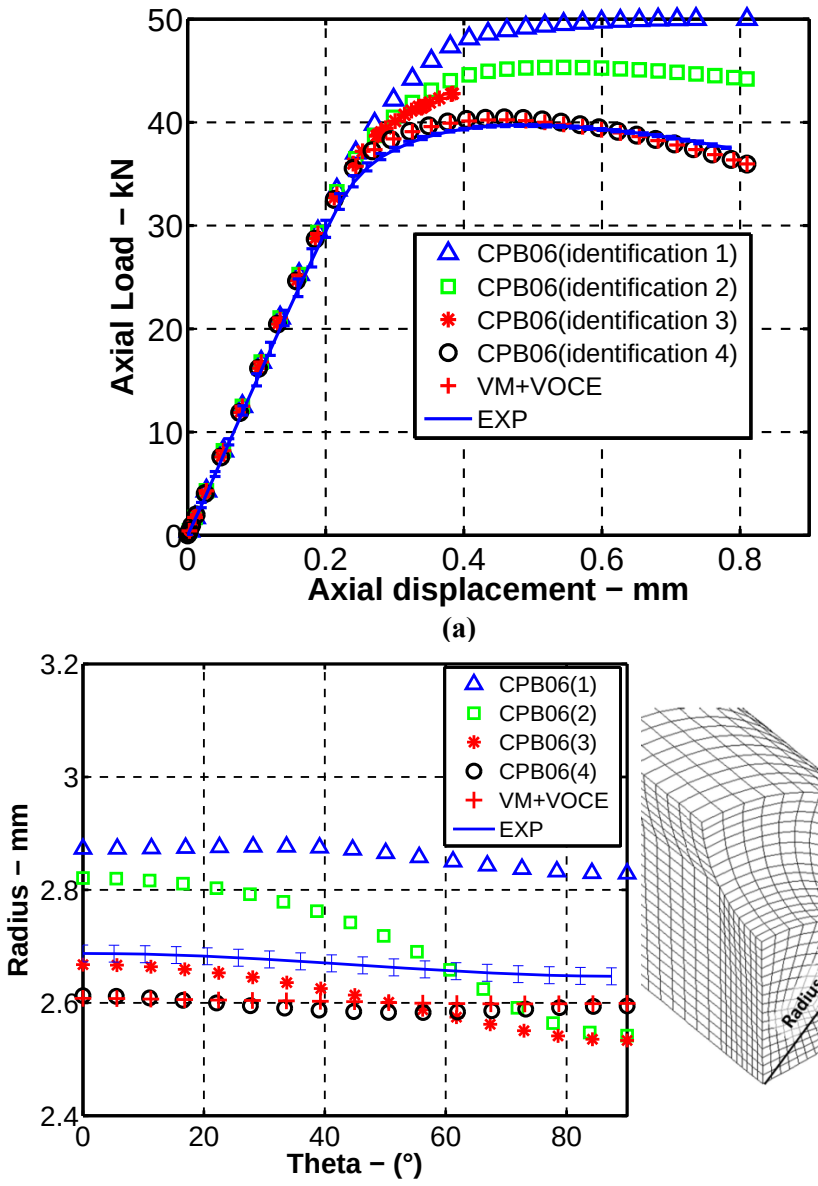

Figure 4.11. CPB06 predictions of the (a) load vs. displacement for specimen geometry R1.5 (40 mm gauge length) (b) cross–section of the specimen geometry R1.5 for 0.8mm of axial displacement.

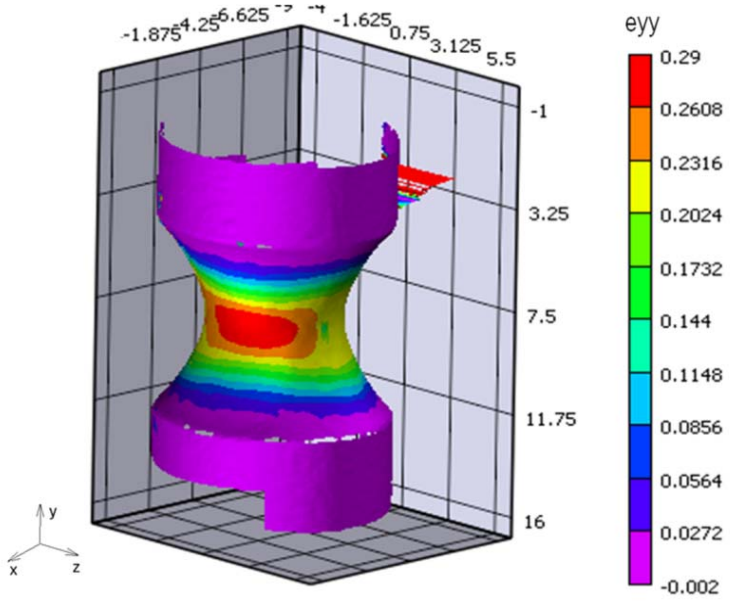

(a)

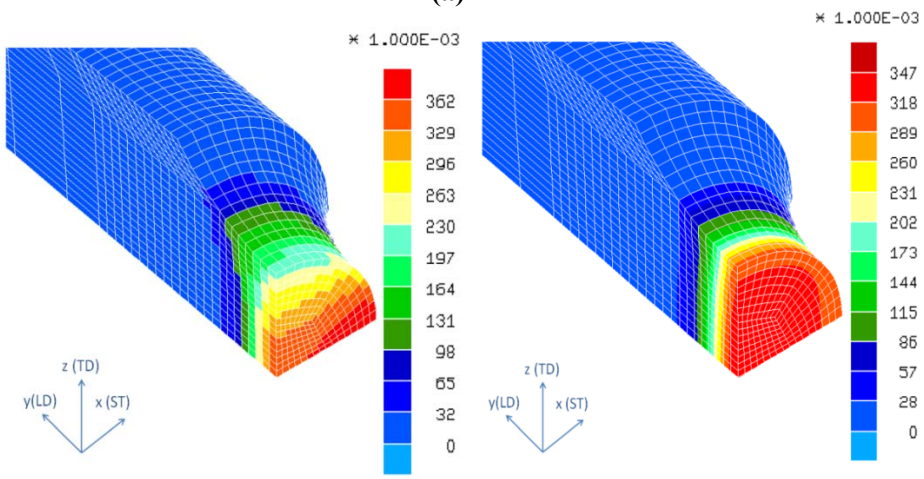

(b) (c)

Figure 4.12. Comparison of axial strain field ε_{yy} for geometry R5 at 1 mm of axial displacement. (a) measured by 3D–DIC (b) predicted by CPB06(3) and (c) by CPB06(4).

4.5. Application and validation of the identified CPB06 model

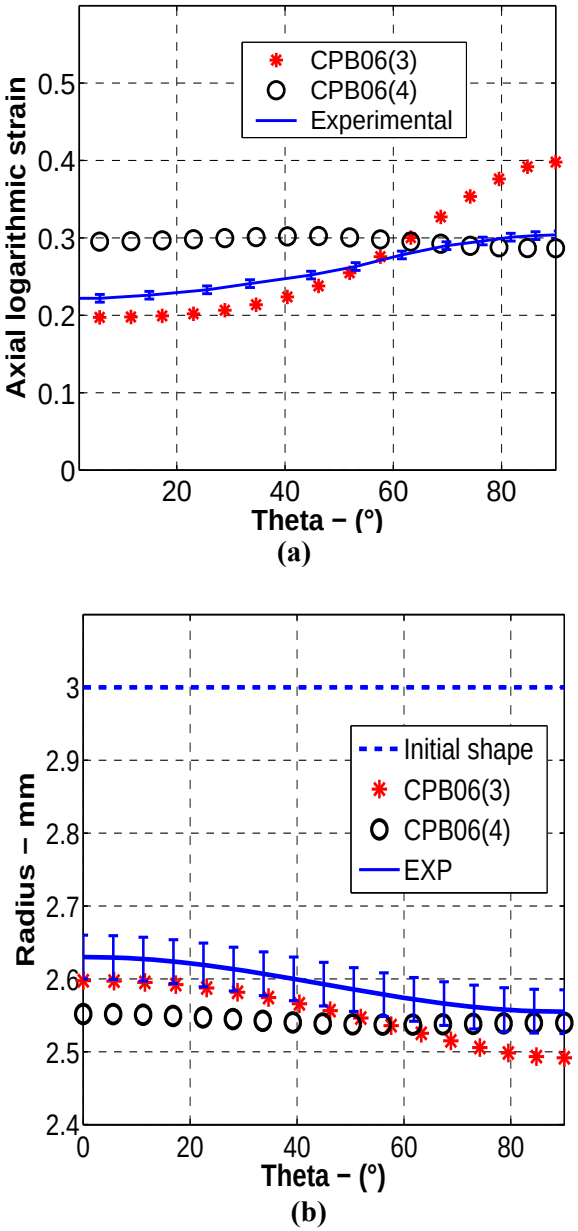

Figure 4.13. Comparison of CPB06(3) and CPB06(4) predictions with DIC measurements for the specimen geometry R5 at 1 mm of axial displacement. (a) Axial strain distribution in the minimum cross–section of specimen. (b) Cross–section of specimen.

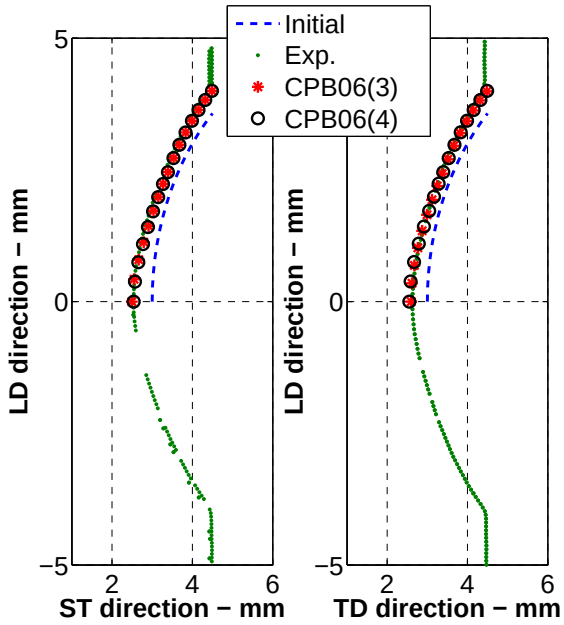

Figure 4.14. Comparison of predicted CPB06(3) and CPB06(4) notch shape of the specimen geometry R5 (at 1 mm of axial displacement) with DIC measurements.

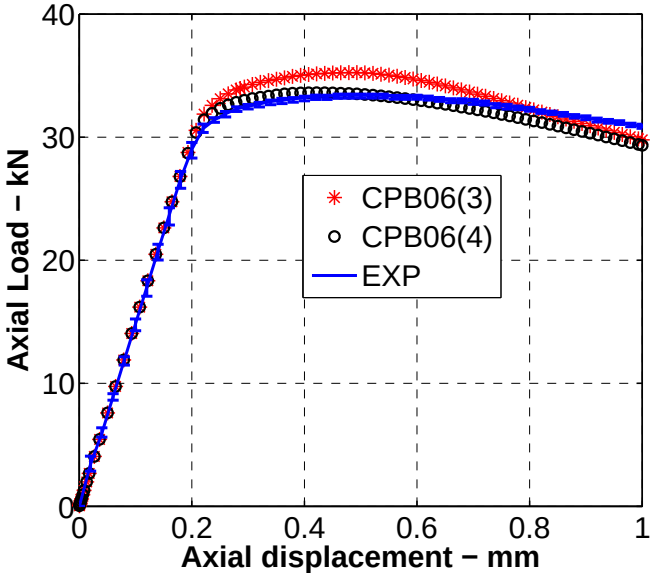

Figure 4.15. Correlations of predicted load vs. displacement curve with experimental results of geometry R5.

4.5. Application and validation of the identified CPB06 model

In Fig. 16, experimental measurements by using DIC for the compression tests in the ST direction were also compared to the FE results obtained with the parameter set CPB06(4). Fig. 4.16 provides a comparison between experimental results and the load predictions for the optimal value of friction coefficient Φ = 0.08 with the CPB06(4) model and with the von Mises model using a hardening law based on a mean stress–strain curve for tension in LD direction. The minor and major axis lengths are shown in Fig.17. The elliptical shape of the middle cross–section of the compression specimen is modified during the test. This effect was expected due to the friction between the dies and the sample and also due to plastic anisotropy of the material. A verification of the effect of friction is shown in Fig. 4.18 by comparing the predicted barreling with the DIC measurements.

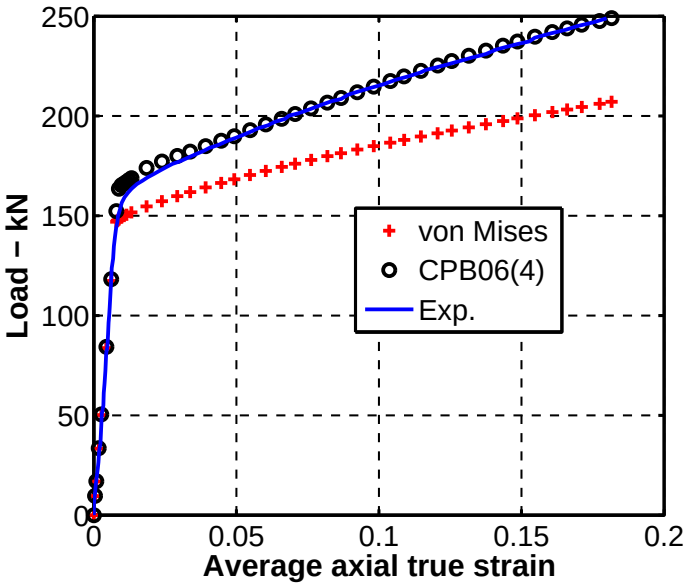

Figure 4.16. Load vs. axial true strain predicted by CPB06(4) and measured in the experiment for compression tests in ST direction.

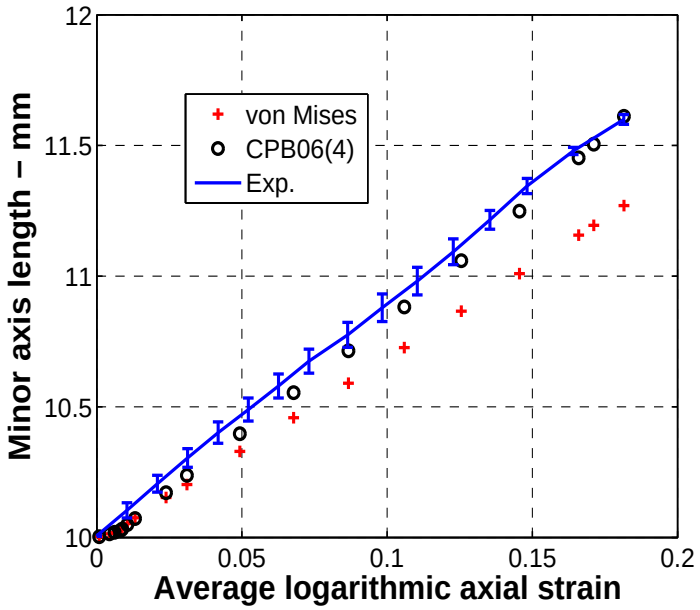

(a)

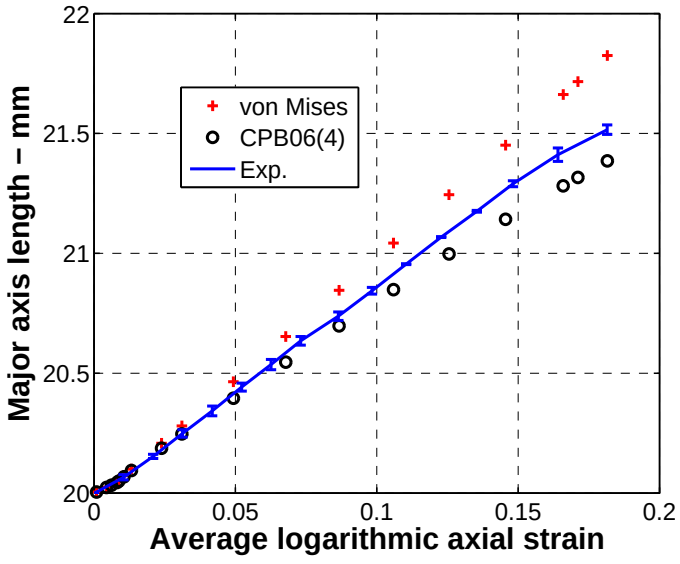

(b)

Figure 4.17. Comparison between DIC measurements, CPB06(4) and von Mises law predictions of minor (a) and major (b) axis length of the elliptical cross–section of compression sample in ST direction.

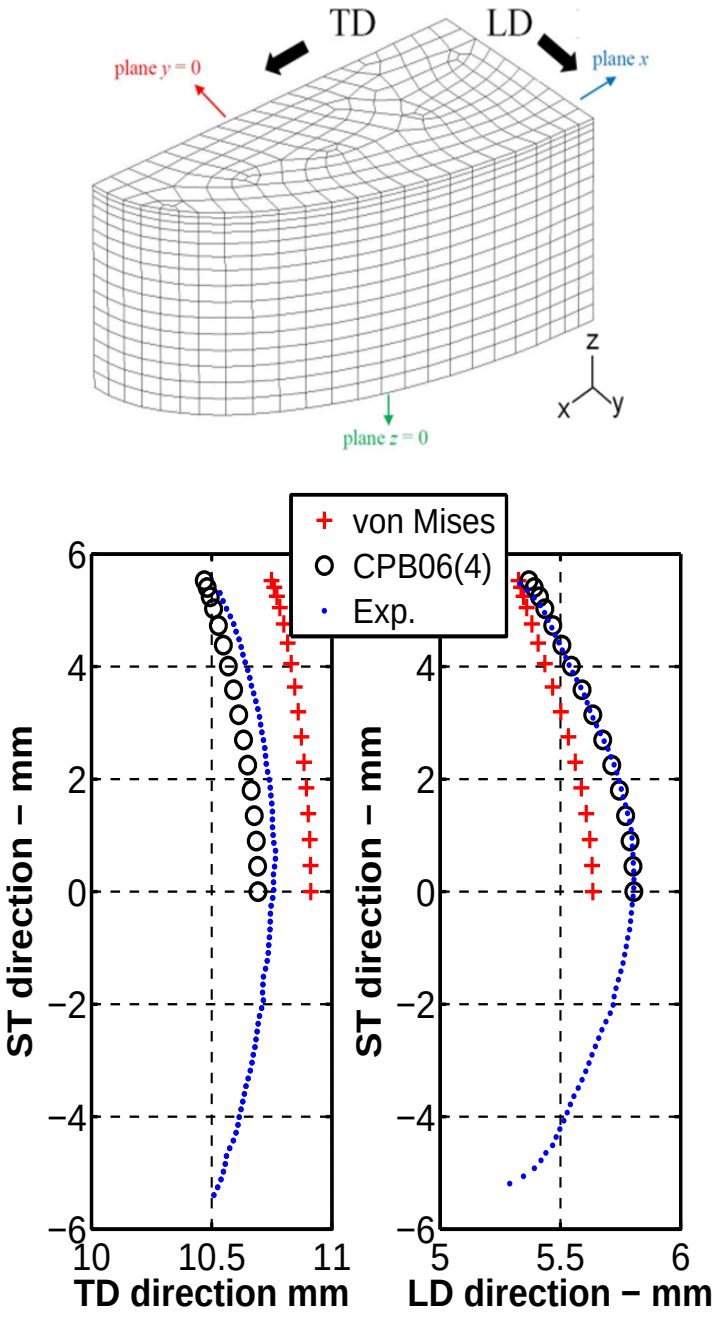

Figure 4.18. Barreling predictions by CPB06(4) and von Mises law compared to experimental measurements obtained by DIC.

4.6. Conclusions

The quasi–static mechanical response of a TA6V alloy was studied based on a wide set of tests at room temperature and low strain rate (10^{-3} s^{-1}). A yield stress anisotropy and tension/compression asymmetry has been revealed. Furthermore, the anisotropy in compression is more pronounced than in tension. Then, the experimental data were used in order to identify the material parameters of the CPB06 yield criterion. The validity of the model was studied at quasi–static strain rate and room temperature. This model captures most of the experimental features:

1. in monotonic tests: the distortion of the yield surface associated with the tension–compression asymmetry and the anisotropic hardening;

2. in specimens with multiaxial stress–strain states and several stress triaxialities (notched tensile tests and compression tests): load, shape changes and strain fields for different loading directions (tensile tests in LD, compression in ST directions).

The simulations demonstrated that the material parameter sets identified with the higher number of tests and taking into account the yield locus shape evolution through interpolation between surfaces associated to different plastic work provides results closer to experimental measurements. The interest of defining identical shear behavior in the 3 orthogonal planes when only one experiment is available, seems demonstrated by the force predictions (Fig. 4.11(a) and Fig. 4.15) but is still unclear for strain distributions (Fig. 4.11(b) and Fig. 12 and Fig. 13(a))).

4.7. Appendix B. Viscoplastic correction

4.7. Appendix B. Viscoplastic correction

The tensile tests in the TD and ST directions were not performed at 10^{-3} s^{-1} strain rate. As mentioned above, with the purpose of identifying the initial anisotropic yield locus and its evolution, the first task is to determine hardening laws at identical strain rate, while also correcting for possible temperature effects. The Johnson–Cook (JC) material model (Johnson and Cook, 1983) is used for this purpose, with the following expression

$$\sigma_y = \left(A + B{\varepsilon_p}^n\right)\left(1 + C\ln\dot{\varepsilon}^*\right)\left(1 - T^{*m}\right) \qquad (4.B.1)$$

where σ_y is the yield stress; ε_p is the equivalent plastic strain; $\dot{\varepsilon}^* = \dot{\varepsilon}/\dot{\varepsilon}_0$ is the dimensionless plastic strain rate (ratio of strain rate to a reference plastic strain rate), T^{*m} is the homologous temperature $T^{*m} = (T–T_{room})/(T_{melt}–T_{room})$. The expression in the first brackets is the strain hardening contribution with the strain hardening coefficient B and the strain hardening exponent n. The expression in the second and third sets of brackets represents the effects of strain rate and temperature, respectively.

In order to avoid temperature effect, the tests where all performed at RT and at low strain rates.

According to Eq. (4.B.1), there is a set of four parameters to identify: X= (*A, B, C, n*) through the minimization of the Euclidean distance between the experimental data and material model.

By using the compression tests at strain rates equal to 10^{-3}, 10^{-2} and 10^{-1} s^{-1}, the strain rate parameter C is identified (Figure 4.B.1(a)) and assumed constant for all the three orthogonal directions. Experimental tensile stress–strain curves for ST and TD performed at different strain rates are used in order to compute a set of hardening parameters *A, B, n* for each direction (Figure 4.B.1(b) and Table 4.B.1). Finally, the true stress–strain curves at a strain rate of 10^{-3} s^{-1} for tensile tests at TD and ST directions are given by the predictions of the identified Johnson–Cook laws.

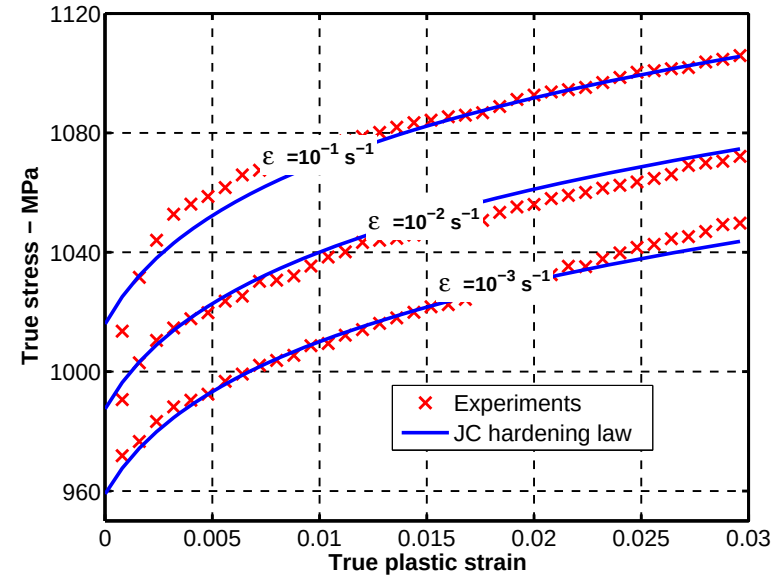

(a)

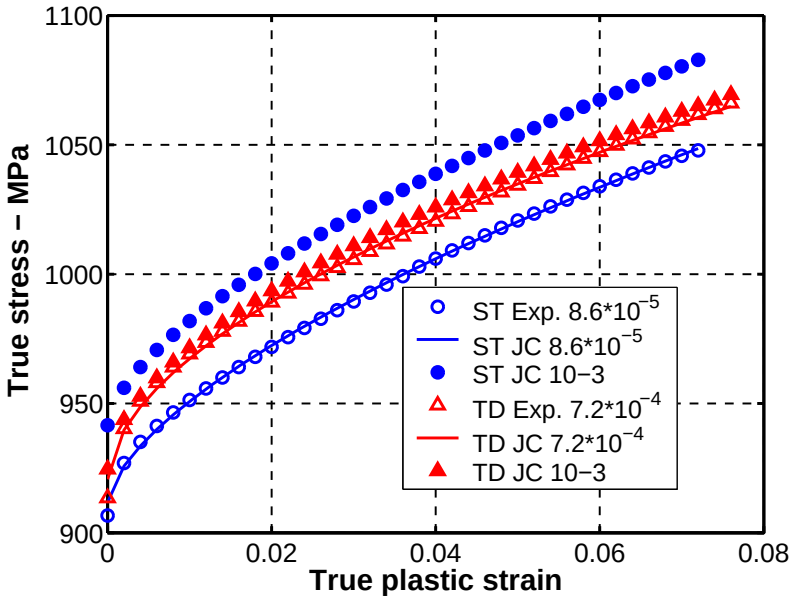

(b)

Figure 4.B.1. Experimental and fitted stress–strain curves by Johnson–Cook model for tension and compression; (a) compression tests at LD and several strain rates; (b) true stress–strain curves for tensile test in the TD and ST directions.

Appendix B. Viscoplastic correction

Table 4.B.1. JC material parameters for compression in LD and tensile in LD and ST directions.

	A	*B*	*C*	*n*
LD compression	785.3	424.5	0.0129	0.1438
TD tension	924.6	607.2	0.0129	0.5563
ST tension	941.6	751.7	0.0129	0.6354

4.8. Appendix C. Quantification of kinematic hardening

Figure 4.C.1 shows the variation of the shear stress ($\tau = F/A_0$) with the shear strain ($\gamma/2$). Three pre–strain 5, 10 and 15% of shear strain tests are presented. The reverse curves show early re–yielding and rapid work hardening. This significant kinematic hardening is quantitatively presented by using the Bauschinger ratio (Br) defined by

$$Br = \frac{\sigma_f - \sigma_R}{2\sigma_F}, \quad (Br \leq 1) \tag{4.C.1}$$

where σ_F is the yield stress at the start of unloading and is the σ_R the yield stress at the reverse loading (Table 4.C.1). Br is equal to 1 for pure isotropic hardening $(\sigma_f = -\sigma_R)$. The smaller the Bauschinger ratio, the larger the Bauschinger effect. The presence of different stress levels within the α and β phases of the TA6V as well as the heterogeneity of the strain at the local level (twins and grain orientation implying different active slip systems with different critical resolved shear) explain the origin of the kinematic hardening.

Table 4.C.1. Bauschinger ratios as a function of pre–strain measured in shear tests for TA6V.

Pre–strain	*Br* (1st unloading)	*Br* (2nd unloading)
5%	0.77	0.73
10%	0.72	0.69
15%	0.69	0.67

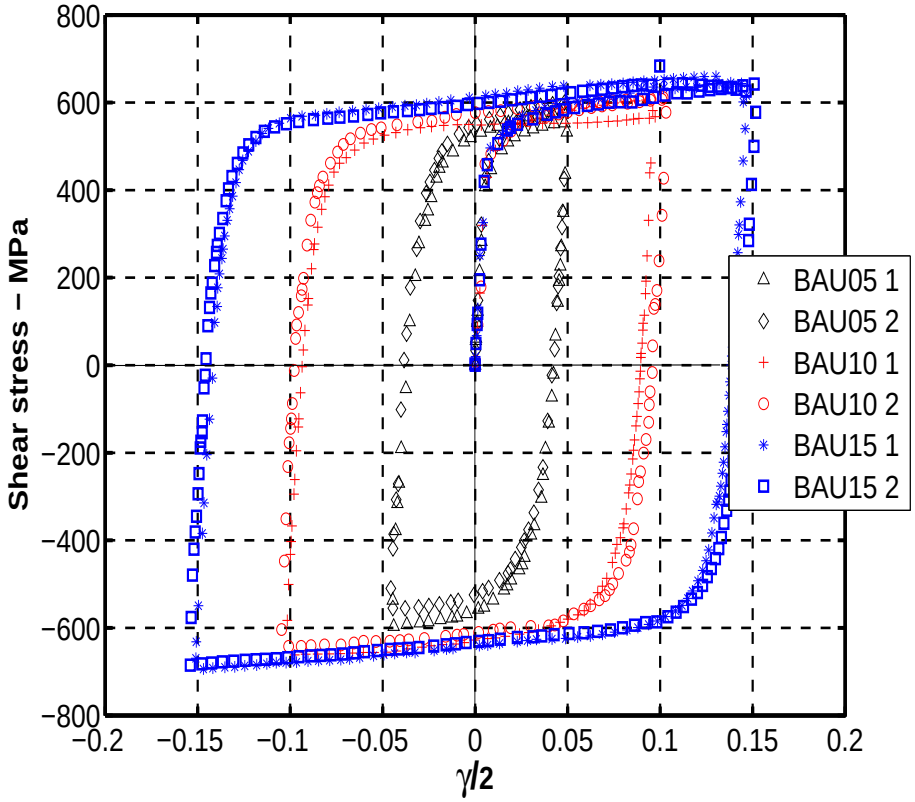

Figure 4.C.1. Shear stress vs. shear strain curves for Bauschinger (BAU) tests at 05%, 10% and 15% shear prestrains. Two tests for each shear level are shown (1 and 2).

4.9. References

ASTM, 2010. Standard Test Method for Young's Modulus, Tangent Modulus, and Chord Modulus. ASTM E111 – 04.

Belytschko, T., Bindeman, L.P., 1991. Assumed strain stabilization of the 4–node quadrilateral with 1–point quadrature for nonlinear problems. Comput. Methods Appl. Mech. Eng. 88, 311–340.

4.9. References

Bettaieb, M.B., Lemoine, X., Duchêne, L., Habraken, A.M., 2011. On the numerical integration of an advanced Gurson model. Int. J. Numer. Meth. Engng. 85, 1049–1072.

Donachie Jr., M.J., 2000. Titanium: a technical guide, Second edition. ASTM international, Ohio, USA.

Cazacu, O., Plunkett, B., Barlat, F., 2006. Orthotropic yield criterion for hexagonal close packed metals. Int. J. Plasticity 22, 1171–1194.

Duchêne, L., El Houdaigui, F., Habraken, A.M. 2007. Length changes and texture prediction during free end torsion test of copper bars with FEM and remeshing techniques, Int.J. Plasticity, 23, 1417–1438.

Flores, P., Rondia, E., Habraken, A.M., 2005. Development of an experimental equipment for the identification of constitutive laws. Int. J. Forming Processes (Special Issue), 117–137

Flores, P., Tuninetti, V., Gilles, G., Gonry, P., Duchêne, L., Habraken, A.M., 2010. Accurate stress computation in plane strain tensile tests for sheet metal using experimental data. J. Mater. Process. Technol. 210, 1772–1779.

Gilles, G., Hammami, W., Libertiaux, V. Cazacu, O. Yoon, J.H., Kuwabara, T., Habraken, A.M., Duchêne, L. 2011. Experimental characterization and elasto–plastic modeling of the quasi–static mechanical response of TA–6 V at room temperature. Int. J. Solids Struct. 48, 1277–1289.

Habraken, A.M., Cescotto, S., 1998. Contact between deformable solids: The fully coupled approach. Mathematical and Computer Modelling 28, 153–169.

Hammami, W., Tirry, W., Coghe, F., Duchêne, L., Delannay, L., Habraken, A.M., 2011. Ti6A14V anisotropy and texture evolution predictions using Multisite and self consistent crystal plasticity models. The 12th World Conference on Titanium Ti–2011.

Hastings, W.K., 1970. Monte Carlo sampling methods using Markov chains and their applications. Biometrika 57, 97–109.

Hill, R., 1987. Constitutive dual potentials in classical plasticity. J. Mech. Phys. Solids 35, 23–33.

Johnson, G.R., Cook, W.H, 1983. A constitutive model and data for metals subjected to large strains, high strain rates and high temperatures. Proceedings of the 7th International Symposium on Ballistics: 541–547.

Khan, A.S., Kazmi, R., Farroch, B., 2007. Multiaxial and non–proportional loading responses, anisotropy and modeling of Ti–6Al–4V titanium alloy over wide ranges of strain rates and temperatures. Int. J. Plasticity 23, 931–950,

Khan, A.S., Liang, R., 1999. Behaviors of three BCC metal over a wide range of strain rates and temperatures: experiments and modeling. Int. J. Plasticity 15, 1089–1109.

Khan, A.S., Suh, Y.S., Kazmi, R., 2004. Quasi–static and dynamic loading responses and constitutive modeling of titanium alloys. Int. J. Plasticity 20, 2233–2248.

Khan, A.S., Yu, S., 2012. Deformation induced anisotropic responses of Ti–6Al–4V alloy. Part I: Experiments. Int. J. Plasticity 38, 1–13.

Khan, A.S., Yu, S., Liu, H., 2012. Deformation induced anisotropic responses of Ti–6Al–4V alloy Part II: A strain rate and temperature dependent anisotropic yield criterion, Int. J. Plasticity 38, 14–26.

Kotkunde, N., Deole, A.D., Gupta, A.K., Singh, S.K., 2014. Comparative study of constitutive modeling for Ti–6Al–4V alloy at low strain rates and elevated temperatures. Materials & Design 55, 999–1005.

Lanning, D., Nicholas, T., Haritos, G., 2005. On the use of critical distance theories for the prediction of the high cycle fatigue limit stress in notched Ti–6Al–4V. Int. J. of Fatigue 27, 45–57.

Lecarme, L., 2013. Viscoplasticity, Damage and Fracture of Ti–6Al–4V. PhD thesis, Université Catholique de Louvain, Belgium.

4.9. References

Lee, W.S., Lin, C.F., 1998. Plastic deformation and fracture behaviour of TA6V alloy loaded with high strain rate under various temperatures. Mater. Sci. Eng. A 241, 48–59.

Lou, X.Y., Li, M., Boger, R.K., Agnew, S.R., Wagoner, R.H., 2007. Hardening evolution of AZ31B Mg sheet. Int. J. Plasticity 23, 44–86.

Majorell, A., Srivatsa, S., Picu, R.C, 2002. Mechanical behavior of TA6V at high and moderate temperatures – Part I: Experimental results. Mater. Sci. Eng. A 326, 297–305.

Metropolis, N., Rosenbluth, A.W., Rosenbluth, M.N., Teller, A.H., Teller, E., 1953. Equation of state calculations by fast computing machines. J. Chem. Phys 21, 1087–1092.

Nixon, M.E., Cazacu, O., Lebensohn, R.A., 2010. Anisotropic response of high–purity α–titanium: experimental characterization and constitutive modeling. Int. J. Plasticity 26, 516–532.

Odenberger, E.L., Hertzman, J., Thilderkvist, P., Merklein, M., Kuppert, A., Stöhr, T., Lechler, J., Oldenburg, M., 2012. Thermo–mechanical sheet metal forming of aero engine components in Ti–6Al–4V – PART 1: Material characterisation. Int. J. Mater. Form., 1–12.

Olsen, R.H. Moreen, H.A., 1973. Calculation of the elastic anisotropy of Ti–6Al–4V alloy sheet from pole figure data. Metall. Trans. 4, 701–705.

Peirs, J., Verleysen, P., Degrieck, J., Coghe, F., 2010. The use of hat–shaped specimens to study the high strain rate shear behaviour of Ti–6Al 4V Int. J. Impact Eng. 37, 703–714.

Peirs, J., 2012. Experimental characterisation and modelling of the dynamic behaviour of the titanium alloy Ti6Al4V. PhD thesis, Ghent University, Belgium.

Plunkett, B., Lebensohn, R.A., Cazacu, O., Barlat, F., 2006. Anisotropic yield function of hexagonal materials taking into account texture development and anisotropic hardening. Acta Mater. 54, 4159–4169.

Simo, J.C., Hughes, T.J.R., 1986. On the variational foundations of assumed strain methods. J. Appl. Mech., ASME 53, 51–54.

Tromans, D., 2011. Elastic Anisotropy of Hcp Metal Crystals and Polycrystals. Int. J. Research & Reviews in Applied Sciences 6, 462–483

Tuninetti, V., Gilles, G., Péron–Lührs, V. Habraken, A.M., 2012a. Compression Test for Metal Characterization using Digital Image Correlation and Inverse Modeling, Procedia IUTAM. 4, 206–214.

Tuninetti, V., Gilles, G., Milis, O., Lecarme, L., Habraken, A.M., 2012b. Compression test for plastic anisotropy characterization using optical full–field displacement measurement technique. Steel Res. Int. SE: 14th Int. Conf. Metal Forming 2012, 1239–1242.

Vanderhasten, M., Rabet, L., Verlinden, B., 2008. Ti–6Al–4V: Deformation map and modelisation of tensile behavior. Materials & Design 29, 1090–1098

Chapter 5. Anisotropy, SD effect and strain rate hardening predictions of the plastic response of bulk TA6V at high temperatures

This chapter is based on the published article:

Impact of anisotropy and viscosity to model the mechanical behavior of Ti–6Al–4V alloy

Authors: V. Tuninetti , A.M. Habraken.

Journal: Materials Science and Engineering: A, 605, 39–50, (2014).

This chapter compares the predictions of an isotropic thermo–elasto–viscoplastic approach and of an anisotropic thermo–elastoplastic one with experimental results representative of the mechanical behavior of Ti–6Al–4V at moderate temperatures and low strain rates. The first model is the well known Norton–Hoff viscoplastic constitutive law with isotropic von Mises yield locus identified by using monotonic tension tests performed at strain rates from 10^{-3} s^{-1} to 10^{-1} s^{-1} and at temperatures up to 400 °C. The second model is a thermo–elasto–plastic one defined by the orthotropic yield criterion CPB06 of Cazacu et al. (2006) described in Chapter 4. It takes into account the anisotropy and the strength differential (SD) effect in tension–compression of Ti–6Al–4V at RT, 150 °C and 400 °C. The identification of the SD effect is done by using tension and compression tests at the identification temperature and the anisotropy behavior is identified by using shear, plane strain, tension and compression tests performed in three orthogonal material directions. The accuracy of the load and displacements predictions of the two macroscopic constitutive models are compared to experimental results obtained from tests performed on specimens with multiaxial loadings and large strain at several temperatures.

5.1. Introduction

Over the last few years, numerous experimental studies have been carried out on TA6V alloy in order to characterize its mechanical behavior as a function of strain rates and temperature. In addition to the strength differential (SD) effect, and a distortion of the yield surface with the accumulated plastic deformation studied in Chapter 4, reported results in the literature (Burkins et al., 2000 and 2001, Lee and Lin, 1998, Khan et al., 2004, 2007, 2012b, Majorell et al., 2002, Peirs et al., 2010, Meyer Jr and Kleponis, 2001, Milani et al., 2009, Seo et al., 2005) show that the yield stress of this two phase $\alpha+\beta$–type alloy is strongly dependent on both temperature and strain rate. Like many other metals, the higher the strain rate, the greater is the yield stress. On the other hand, the stress level decreases when temperature increases. Nevertheless, the effect of the temperature on the yield stress has been found greater than the one of the strain rate for low and high strain rates and temperatures from RT to 1000K (Lee and Lin, 1998, khan et al. 2004). Lee and Lin, 1998 and Arrieta and Espinosa, 2001, explain that the increase of temperature tends to reduce the yield stress by lowering the thermally activated part of the resistance to dislocation motions.

Many different purely phenomenological models are currently available to describe the strain hardening, strain–rate hardening, and thermal softening of materials with specific material constants, e.g., Johnson–Cook (JC) (Johnson and Cook, 1983), Norton–Hoff (NH) (Norton, 1929), Khan–Huang–Liang (KHL) (Khan et al., 2004) models, etc. Most of the studies available in the literature (Zhang et al., 2012, Lee and Lin, 1997, Khan et al., 2004, 2007, 2012a, 2012b, Seo et al., 2005) focus on capturing softening, workability, work hardening for cold (RT), warm (around 400 °C) and hot working processes (around 900 °C). However, the validation of these models is essentially based on predictions of the true stress–strain curves of experimental tests.

Many commercial FE codes offer isotropic viscoplastic and anisotropic elastoplastic constitutive models to describe material behavior. However, even if some authors propose anisotropic viscoplastic approach (Bron and Besson, 2004; Plunkett et al., 2007) the standard user of commercial codes in industry has generally to choose between neglecting viscosity or

anisotropy. For this reason, this Chapter presents an evaluation of the mechanical modeling of TA6V alloy by comparing the prediction accuracy of these two types of macroscopic plasticity models. The first one is the Norton–Hoff (NH) constitutive law with the isotropic von Mises (VM) yield locus which accounts for isotropic–thermo–viscoplastic behavior of materials and the second one is the CPB06 yield criterion modeling the plastic anisotropy and the SD effect. In both cases, elasticity follows Hooke's law taking into account anisotropic elastic coefficients.

The identification of the NH constitutive model is based on tension tests performed in one material direction at constant strain rates equal to 10^{-3}, 10^{-2} and 10^{-1} s^{-1} and at room temperature (RT), 150 °C and 400 °C for the bulk TA6V alloy. A study of temperature and strain rate sensitivity of the plastic behavior of the alloy is also presented hereafter.

The identification of the CPB06 yield loci for the same TA6V has already been described in Chapter 4 (Tuninetti et al. (under–review)) at RT and at one strain rate equal to 10^{-3} s^{-1}. In addition, a new set of parameters of CPB06 identified at 150 °C and 400 °C is computed in this Chapter, using tension and compression tests performed at a constant strain rate equal to 10^{-3} s^{-1} at 150 °C and 400 °C.

The capacities of the two identified models (CPB06 and NH) to accurately reproduce the plastic behavior of TA6V at several temperatures and low strain rate range are evaluated. The error between FE predictions and experimental data allows quantitative comparison of the accuracy of the two models in force and displacement predictions on specimens subjected to multiaxial tensile and compressive loading, with different initial stress triaxialities and large strains. The tests used for the validation of the models are compression tests on elliptical cross–section specimens, tensile tests on notched round bars and tensile tests on holed round bars performed at temperatures up to 400 °C. Note that none of these tests were included in the database used for the identification of the models.

These identified material models can be used not only for FE simulations of cold and warm bulk forming processes of TA6V, but also for aircraft structural or engine components design at operating temperatures. The current study helps designers to make the right decision in choosing the

5.1. Introduction

constitutive law for the simulations of the mechanical behavior of the TA6V alloy with similar microstructure as the one studied here.

Chapter 5 is actually similar to the article Tuninetti and Habraken (2014) except for this introduction which was shortened as the reader had already discovered same information in previous chapters. It is organized as follows:

- Section 2 describes the experimental framework used to perform the tests
- Section 3 presents the experimental results obtained at several temperatures: elastic parameters, strain rate sensitivity and SD effect.
- Section 4 introduces the NH and the CPB06 models. *The reader could skip the description of the CPB06 model as it was already given in Chapter 4* but stays here for the continuity of the text.
- Section 5 presents the identification procedure of the models adopted to determine the material parameters. Besides, the comparisons of their analytical predictions with experimental uniaxial stress–strain curves used for their identification are shown.
- Section 6 focuses on the evaluation of the predictions of the models on complex specimens involving different loading and stress triaxilities.
- Lastly, in section 7 the overall conclusions are highlighted.

It is recalled that that damage is not addressed in this thesis. As verified, it does not prevent the constitutive laws to model the TA6V behavior even for large plastic strain after the onset of necking. This fact is related to the mechanism of ductile fracture in TA6V due to void nucleation, growth and coalescence which is strongly localized and affects the mechanical behavior only for states very close to rupture (Lecarme, 2013; Peirs, 2012).

5.2. Material properties, testing equipments and experimental procedures

5.2.1. Material

The material properties, chemical composition, grain size and orientation, α–phase percentage of the volume and initial texture are given in Chapter 4, Section 2.1.

5.2.2.Monotonic compression and tensile tests at several temperatures and strain rates

The compression tests performed at RT are conducted using a servohydraulic testing machine which is controlled in order to impose constant strain rates equal to 10^{-3}, 10^{-2}, and 10^{-1} s^{-1}. For the tests at elevated temperatures (between 150 °C and 800 °C) the testing machine is equipped with an Infrared (IR) furnace (Quad Ellipse Chamber, Model E4, Radiant Energy Research Inc.) and the targeted constant strain rate is equal to 10^{-3} s^{-1}. Stress–strain curves for compression tests are computed by using the method described in Chapter 3 (Tuninetti et al., 2012a).

The tensile tests are performed at constant strain rates equal to 10^{-3}, 10^{-2}, and 10^{-1} s^{-1} for each level of temperature (RT, 150 °C and 400 °C). A universal testing machine (electro–mechanic Press ZWICK 100 kN) equipped with a H&C furnace with three independent heating zones is used.

Prior to both tensile and compression tests, the specimens were held for 10 minutes at the testing temperature in order to ensure a homogeneous temperature distribution through the specimens. The experimental setup at elevated temperatures did not allow the use of an extensometer or optical measurements. For this reason, a procedure for the correction of the deflection of testing machine was developed and implemented in order to reach constant strain rates (See Chapter 2, Section 1). All of the monotonic compression and tensile tests are performed in the longitudinal material direction (LD) for all the investigated temperatures and strain rates. The anisotropy was investigated by means of other tests described in Chaper 4.

5.3. Tensile and compression experimental results at several temperatures

Table 5.1 shows the average initial yield strength and the Young's modulus with the standard deviation. This experimental material data show that the alloy involves strain rate and temperature sensitive properties, as well as SD effect.

Table 5.1. Experimental Young's modulus and yield stress for tension and compression at several temperatures and strain rates for LD direction.

Test	Temperature °C	Strain rate s^{-1}	Young's Modulus E GPa ± Std. Dev.	Yield Strength σ_0 MPa (0.2% plastic strain) ± Std. Dev.
Tension	RT	10^{-1}	–	–
		10^{-2}	113±1	973±1
		10^{-3}	111±1	927±3
	150	10^{-1}	63.5±4	743±5
		10^{-2}	74.9±3	784±1
		10^{-3}	85.7±5	740±4
	400	10^{-1}	57.6±6	451±3
		10^{-2}	68.0±1	531±2
		10^{-3}	70.8±2	528±2
Compression	RT	10^{-1}	127±3	1013±5
		10^{-2}	125±4	986±4
		10^{-3}	122±1	968±3
	150	10^{-3}	74.3±4	772±5
	400	10^{-3}	66±7	540±4
	600	10^{-3}	41.6	386
	800	10^{-3}	11	106

5.3.1. Strain rate sensitivity

The tensile yield stress as a function of the strain rate at 0.02 of true plastic axial strain in tensile tests is presented in Fig. 5.1. The usual value of 0.2% of plastic strain to define yield stress is not adopted because it is not representative of the studied plastic range. A linear increase of the yield stress with the strain rate is observed at RT and 150 °C, and a weak strain rate influence on the yield stress is found at 400 °C.

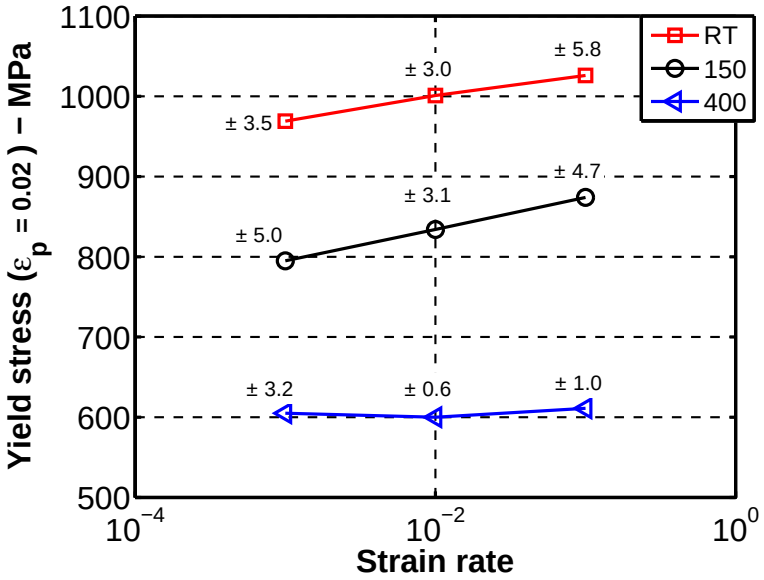

Figure 5.1. Yield stress in tension at 2% of plastic strain as a function of the strain rate at several temperatures.

5.3.2. Temperature sensitivity

Fig. 5.2 shows the evolution of the yield stress at 0.02 of true plastic strain with the temperature under several low strain rates. A strong effect of the temperature on the yield stress is observed. The stress rapidly decreases with the increase of the temperature for all the investigated strain rates. Note that at low strain rates ($<10^{-1}$ s^{-1}) the temperature increase on the sample associated to plastic work is negligible and therefore the tests are considered as isothermals.

5.3. Tensile and compression experimental results at several temperatures

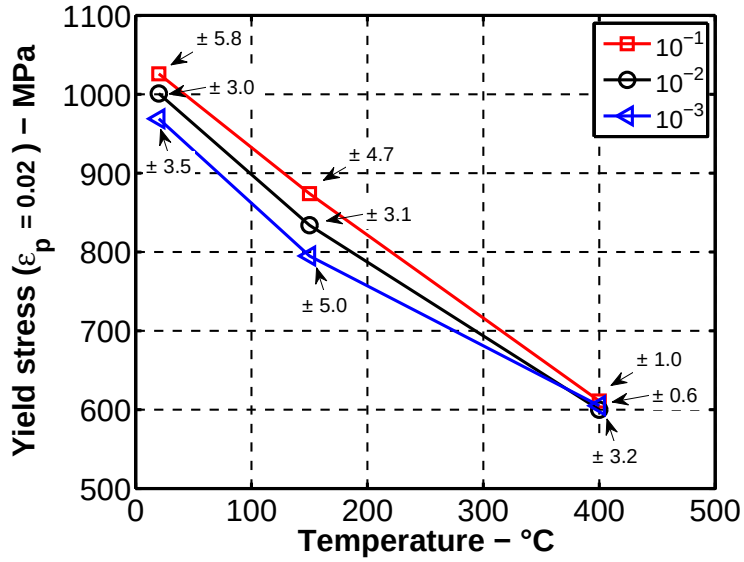

(a)

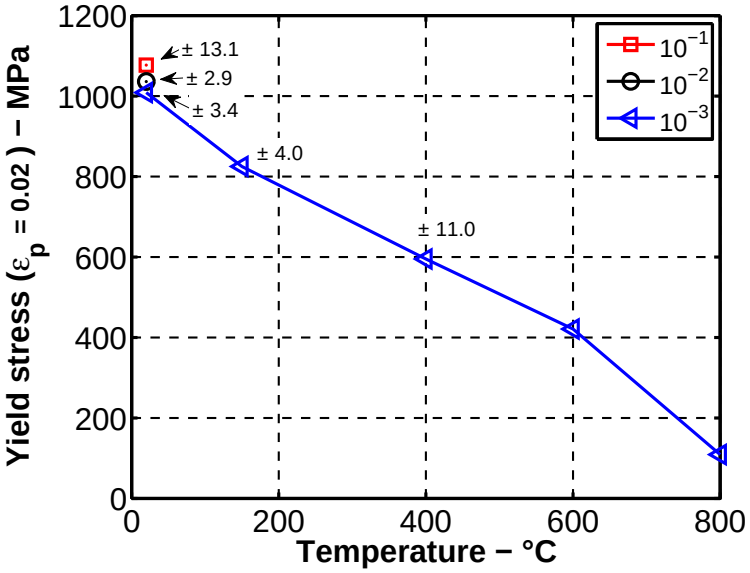

(b)

Figure 5.2. Yield stress at 2% of plastic strain as a function of the temperature under several strain rates investigated. (a) Tension. (b) Compression.

5.3.3. SD effect and anisotropic hardening

Tensile and compression true stress/strain curves of test performed at constant strain rate equal to 10^{-3} s^{-1} are shown in Fig. 5.3(a). These curves demonstrate that the hardening rate is different in tension and in compression and varies with the temperature. Fig. 5.3(b) gathers the values of yield stress evolution with the temperature for tension and compression at a true strain value equal to 0.02. Based in this experimental information, it can be concluded that the material response of TA6V demonstrates a strength asymmetry between tension and compression (SD effect) for the temperature range investigated but a weak asymmetry at 400 °C.

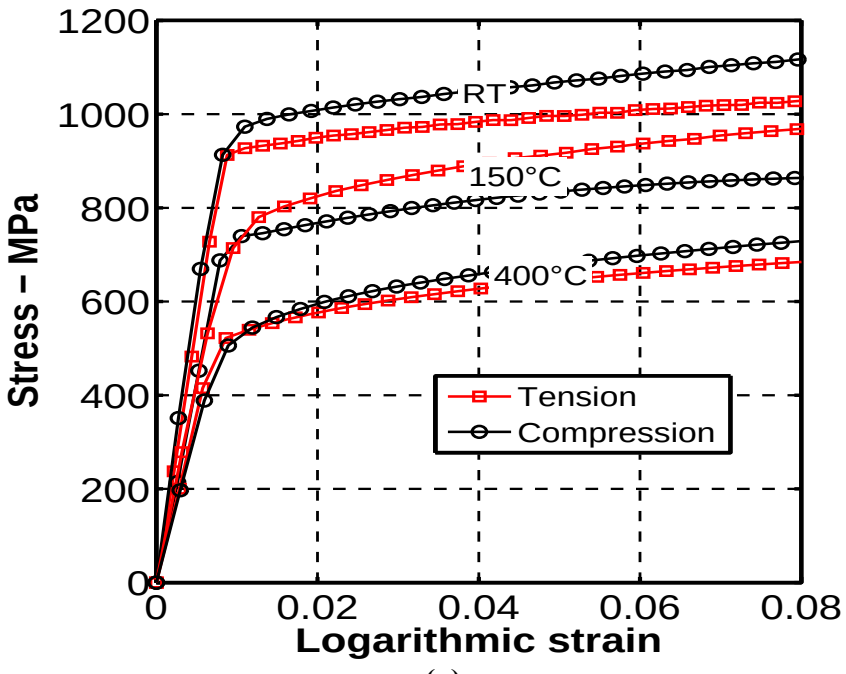

(a)

5.3. Tensile and compression experimental results at several temperatures

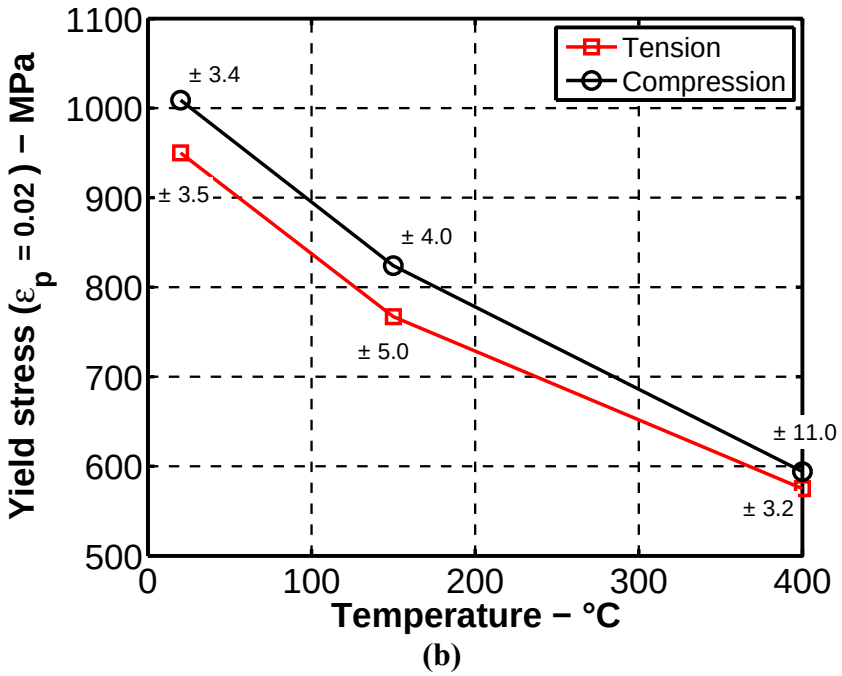

(b)

Figure 5.3. (a) True stress strain curves for monotonic tensile and compression in LD material direction at 10^{-3} s^{-1} and at RT, 150 °C and 400 °C (b) Yield stress in tension and compression at 2% of plastic strain as a function of the temperature.

5.4. Constitutive models

In this section, the Norton–Hoff and the CPB06 models are presented.

5.4.1. The elasto–thermo–viscoplastic Norton–Hoff model

A non–linear thermo–viscoplastic formulation with the strain rate sensitivity introduced by the Norton–Hoff material model is chosen to predict the observed dependence of the yield stress on the strain, strain rate and temperature of TA6V at large strains. The Norton–Hoff (NH) law was introduced by Norton (Norton, 1929) in order to describe the uniaxial creep of steel at high temperature and extended by Hoff (Hoff, 1954) to the multiaxial loadings. The constitutive equation is defined as follows:

$$\overline{\sigma} = \exp(-P_1\overline{\varepsilon})\sqrt{3}P_2(\sqrt{3}\dot{\overline{\varepsilon}})^{P_3}\overline{\varepsilon}^{P_4} \tag{5.1}$$

where $\overline{\sigma}$ is the equivalent stress, $\overline{\varepsilon}$ the equivalent total strain and $\dot{\overline{\varepsilon}}$ the equivalent strain rate. The material parameters P_1, P_2, P_3 and P_4 are related respectively to softening, strength, viscosity and hardening behaviors and they are all thermally affected. The equivalent stress is associated to the von Mises yield criterion and the viscoplastic strain tensor $\dot{\boldsymbol{\varepsilon}}^{vp}$ as a function of stress tensor $\boldsymbol{\sigma}$ is given by (Pascon, 2002):

$$\dot{\boldsymbol{\varepsilon}}^{vp} = \frac{J_2^{P_5}\exp\left(\frac{P_1}{P_3}\overline{\varepsilon}\right)\overline{\varepsilon}^{-\frac{P_4}{P_3}}}{2\left(P_2\right)^{\frac{1}{P_3}}}\boldsymbol{\sigma} \tag{5.2}$$

where $J_2 = \frac{1}{3}\overline{\sigma}^2$ and $P_5 = \frac{1-P_3}{2P_3}$.

5.4.2. The orthotropic CPB06 yield criterion

The CPB06 yield criterion has been already described in Chapter 4. However, for simplicity and the facility of the reader, the main constitutive equations are summarized in this section.

The orthotropic yield criterion CPB06 was developed by Cazacu et al. 2006. The criterion is defined by:

$$F_1 = \left(|\Sigma_1| - k\Sigma_1\right)^a + \left(|\Sigma_2| - k\Sigma_2\right)^a + \left(|\Sigma_3| - k\Sigma_3\right)^a \tag{5.3}$$

k is a parameter which takes into account the strength differential effect (SD) and a is the degree of homogeneity. Σ_1, Σ_2, Σ_3 are the principal values of the tensor $\boldsymbol{\Sigma}$ defined by $\boldsymbol{\Sigma} = \mathbf{C}:\mathbf{S}$ where $\mathbf{C}$ is a fourth–order orthotropic tensor that accounts for the plastic anisotropy of the material and $\mathbf{S}$ is the deviator of the Cauchy stress tensor.

Directional hardening or distortion of the yield locus is taken into account. The anisotropy coefficients C_{ij} and the SD parameter k are obtained for five

fixed levels of plastic work and then the model uses a piece–wise linear interpolation to obtain the yield surface corresponding to any level of plastic work. The updated yield locus is described by

$$f\left(\boldsymbol{\sigma},\bar{\varepsilon}_p\right)=\bar{\sigma}\left(\boldsymbol{\sigma},\bar{\varepsilon}_p\right)-Y\left(\bar{\varepsilon}_p\right) \tag{5.4}$$

$\bar{\sigma}$ is the equivalent plastic strain associated to the given yield criterion in Eq. (5.3) while $\bar{\varepsilon}_p$ is the equivalent plastic strain associated to $\bar{\sigma}$ using the work–equivalence principle (Hill, 1987) and $Y\left(\bar{\varepsilon}_p\right)$ is a reference hardening curve defined as:

$Y\left(\bar{\varepsilon}_p\right)=A_0+B_0\left[1-\exp\left(-C_0\bar{\varepsilon}_p\right)\right]$ where A_0, B_0, C_0 are material constants. For any $\bar{\varepsilon}_p$, the plastic work per unit volume is given by:

$$W_p\left(\bar{\varepsilon}_p\right)=\int_0^{\bar{\varepsilon}_p}Y(p)dp=\left(A_0+B_0\right)\bar{\varepsilon}_p-\frac{B_0}{C_0}\left(1-\exp\left(-C_0\bar{\varepsilon}_p\right)\right) \tag{5.5}$$

5.5. Material parameter identification

In this section, the identifications of the Norton–Hoff and the CPB06 models are presented. In addition, the comparisons of their analytical predictions with experimental results are reported.

5.5.1. Identification of the Norton–Hoff model

The set of NH model parameters are identified at three levels of temperatures, RT, 150 °C and 400 °C by using the experimental equivalent tensile strain–stress curves at strain rates equal to 10^{-3}, 10^{-2} and 10^{-1} s^{-1} (LD direction). A direct identification method is chosen which uses the Nelder–Mead Simplex algorithm (Nelder and Mead, 1965). P_1, P_2, P_3 and P_4 are obtained by minimizing the weighted mean square error (*MSE*) between the experimental (*Exp*) and the model (*NH*) stress–strain curves defined as:

$$MSE=\sum_{\dot{\bar{\varepsilon}}}\sum_{\bar{\varepsilon}}w_{\dot{\bar{\varepsilon}}}\left(\frac{\bar{\sigma}^{Exp}\left(\dot{\bar{\varepsilon}},\bar{\varepsilon}\right)-\bar{\sigma}^{NH}\left(\dot{\bar{\varepsilon}},\bar{\varepsilon}\right)}{\bar{\sigma}^{Exp}\left(\dot{\bar{\varepsilon}},\bar{\varepsilon}\right)}\right)^2 \tag{5.6}$$

The identified NH parameters are given in Table 5.2 and their evolutions are shown in Fig. 5.4. The effect of softening does not appear in the investigated domain of temperatures and P_1 is set with a zero value. As seen in the experimental results section 3, the increasing of temperature decreases the parameter P_2 related to the strength of the material (Fig. 5.4(a)). The strain rate sensitivity parameter P_3 increases from RT to 150 °C and becomes negligible at 400 °C, which indicates that for this latter temperature no strain rate effect occur Fig. 5.4(b). The evolution of P_4 with the temperature shown in Fig. 5.4(c) demonstrates that hardening gradually increases with rising temperature.

An overview of the NH model predictions of true stress–strain curves in tensile and compression as a function of the temperature and the strain rate and compared with experiments is shown in Figs. 5.5 and 5.6. The model properly describes the initial yield stress and strain hardening of the TA6V for the three investigated strain rates and temperatures in uniaxial tensile (Fig. 5.5), but this is not the case in the uniaxial compression (Fig. 5.6). These results are the expected ones as the NH model take into account neither of SD effect nor of anisotropic hardening.

Table 5.2. Values of the identified parameters of the Norton–Hoff law for the TA6V investigated alloy at several temperatures.

Temperature	P_1	P_2	P_3	P_4
RT	0	731.2	0.0110	0.0501
150	0	690.4	0.017	0.0847
400	0	551.2	0.003	0.1246

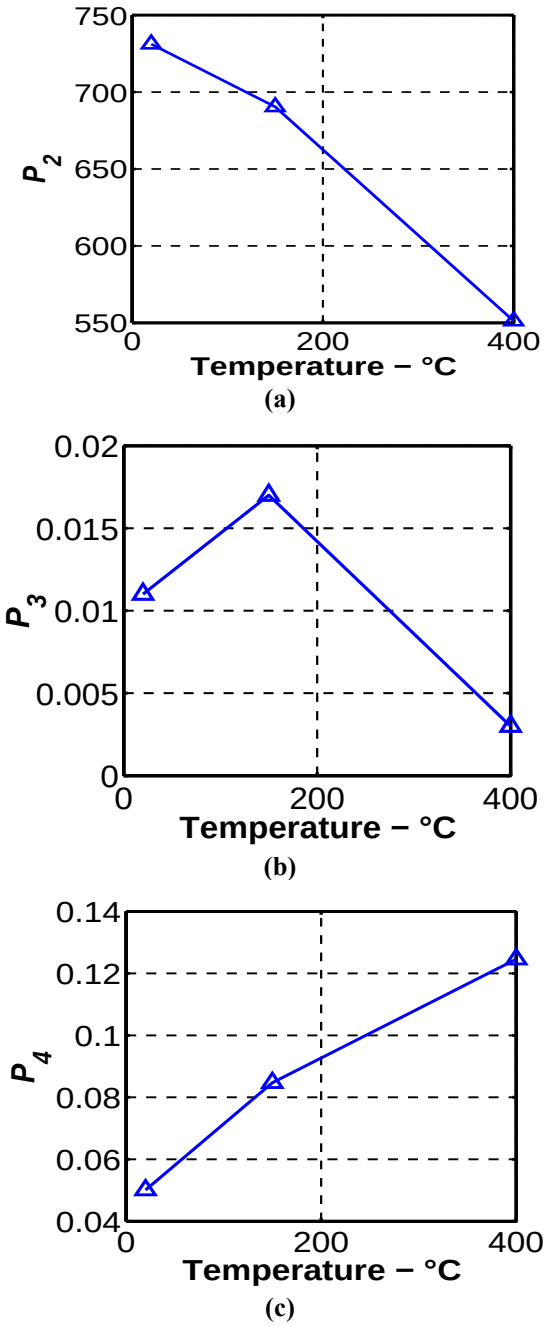

Figure 5.4. Variation of the NH parameters with the temperature. (a) P_2 related to strength, (b) P_3 related to strain rate sensitivity and (c) P_4 related to hardening.

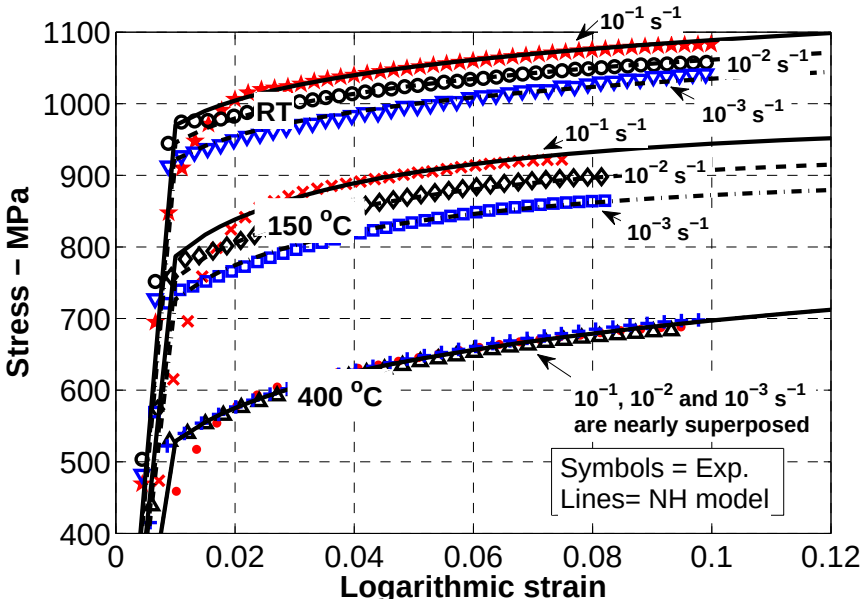

Figure 5.5. N–H law predictions of the true stress strain curves of tensile tests along with experimental data for RT, 150 °C and 400 °C at strain rates equal to 10^{-3}, 10^{-2} and 10^{-1} s^{-1}.

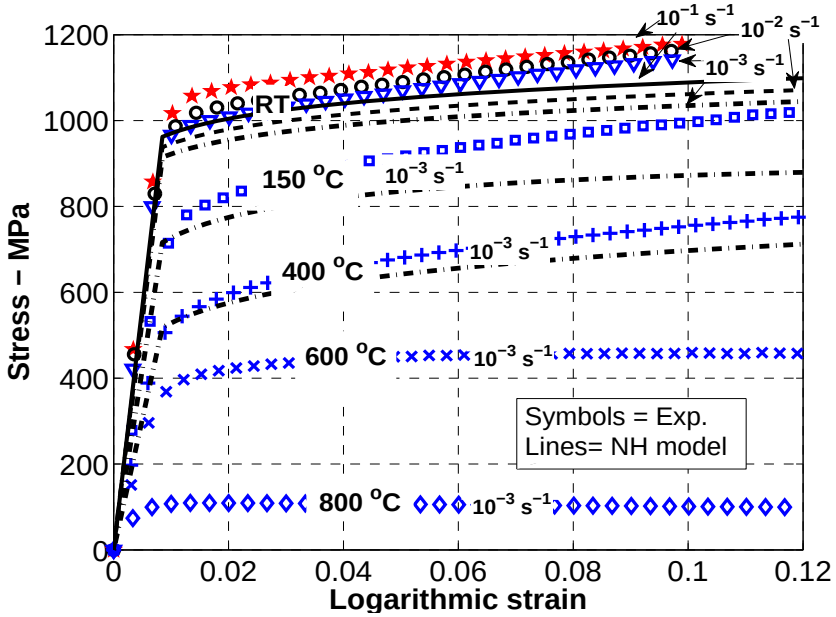

Figure 5.6. N–H law predictions of true stress strain of compression tests along with experimental data at strain rates equal to 10^{-3}, 10^{-2}, and 10^{-1} s^{-1} for RT, 150 °C and 400 °C.

5.5. Material parameter identification

5.5.2. Identification of the CPB06 model at several temperatures

The anisotropy coefficients and SD parameters are considered to evolve as a function of the plastic work per unit volume W_p . In Chapter 4, continuous yield surfaces of CPB06 were identified at five plastic work levels, in three orthogonal directions of the material, at RT and at 10^{-3} s^{-1}. The identification was based on a set of monotonic tests: uniaxial tensile, uniaxial compression, simple shear and plane strain and an inverse modeling of strain fields measured by DIC in compression specimens was used. The excellent capabilities of the model were validated not only in the set of monotonic stress–strain curves but also in specimens (notched tensile tests) with multiaxial loading with accurate results.

The anisotropy coefficients and SD parameters of CPB06 yield criterion identified at RT and presented in Chapter 4 (Tuninetti et al., (under–review)) are used in this Chapter (Table 5.3). In order to predict the SD effect and anisotropy of TA6V at higher temperatures, the CPB06 model is identified in the present study at 150 °C and 400 °C and at 10^{-3} s^{-1} (Table 5.3–5.4). The anisotropy coefficients C_{ij} are kept constant (Table 5.3), but k coefficients and hardening are temperature dependent. This assumption can seems quite strong as microstructure event such as different twining activity and texture evolution with temperature could be expected. However, validation section confirms that the possible loss of accuracy model predictions due to this assumption can be neglected.

Five levels of plastic work are considered for each set of parameters. These levels of plastic work are computed at the same amount of equivalent plastic strain that the ones used for RT. A_0, B_0, C_0 are obtained by fitting the reference hardening curves $Y\left(\bar{\varepsilon}_p\right)= A_0 + B_0\left[1-\exp\left(-C_0\bar{\varepsilon}_p\right)\right]$ with the tensile tests at both identification temperatures. SD parameters (k) are computed for each plastic work levels by fitting the experimental and numerical yield stress ratios between tension and compression using the Simulated Annealing (SA) algorithm (Metropolis *et al.*, 1953, Hastings, 1970).

The biaxial plane projections of the identified CPB06 yield loci (lines) in LD–TD at RT, 150 °C and 400 °C and at 10^{-3} s^{-1} along with the

experimental values (symbols) for the five levels of plastic work are shown in Fig. 5.7. Correlations demonstrate that the CPB06 law predicts the distortion of the yield surface with the variation of plastic work and also the asymmetry between tension and compression for all the range of temperatures.

Table 5.3. Anisotropy coefficients of CPB06 yield function for TA6V for 5 plastic works levels identified at RT (a=2).

Surface	C_{11}	C_{12}	C_{13}	C_{22}	C_{23}	C_{33}	$C_{44}=C_{55}=C_{66}$
1	1	-2.373	-2.364	-1.838	1.196	-2.444	-3.607
2	1	-2.495	-2.928	-2.283	1.284	-2.446	4.015
3	1	-2.428	-2.920	1.652	-2.236	1.003	-3.996
4	1	-2.573	-2.875	1.388	-2.385	0.882	-3.926
5	1	-2.973	-2.927	0.534	-2.963	0.436	-3.883

Table 5.4. SD coefficients k of CPB06 yield function for TA6V for 5 plastic works levels and for RT, 150 °C and 400 °C and parameters of the reference curves (Tensile LD).

		RT		**150 °C**		**400 °C**	
LD tension (ref. curve)	A_0	921		730		525	
	B_0	160		166		201	
	C_0	15.48		23.98		21.93	
		W_p	k	W_p	k	W_p	k
Surface 1		1.857	-0.136	1.553	-0.136	1.364	-0.074
Surface 2		9.377	-0.171	7.682	-0.154	6.513	-0.089
Surface 3		48.66	-0.255	26.51	-0.150	40.78	-0.168
Surface 4		100.2	-0.226	28.14	-0.117	73.17	-0.148
Surface 5		206.6	-0.107	177.1	-0.153	146.8	-0.143

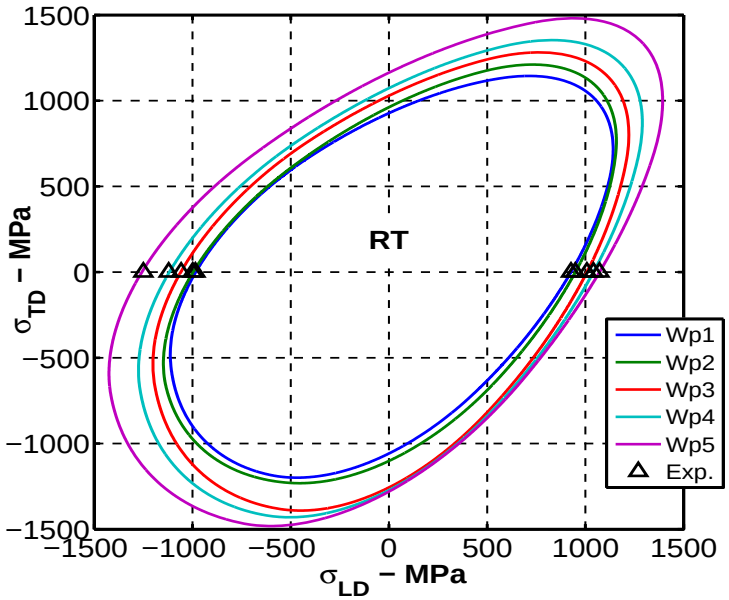
RT
Wp1
Wp2
Wp3
Wp4
Wp5
Exp.
σTD – MPa
σLD – MPa
1500
1000
500
0
−500
−1000
−1500
−1500 −1000 −500 0 500 1000 1500

(a)

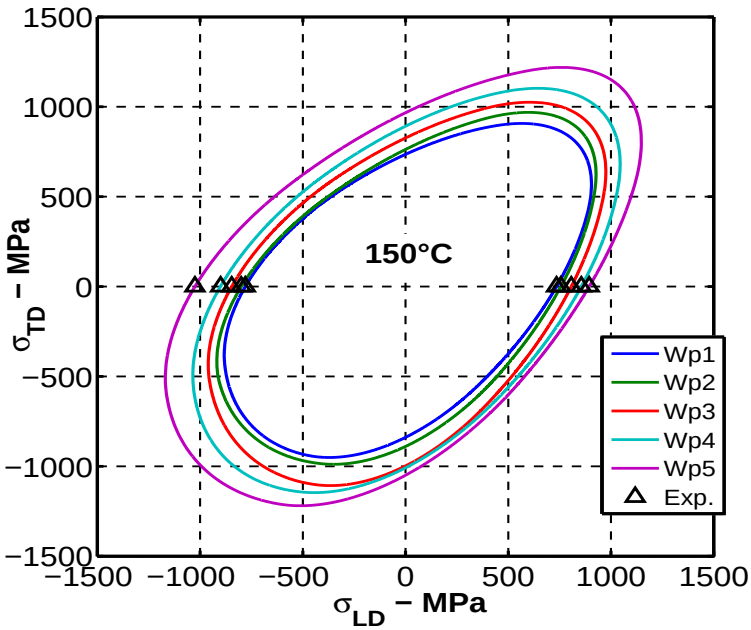
150°C
Wp1
Wp2
Wp3
Wp4
Wp5
Exp.
σTD – MPa
σLD – MPa
1500
1000
500
0
−500
−1000
−1500
−1500 −1000 −500 0 500 1000 1500

(b)

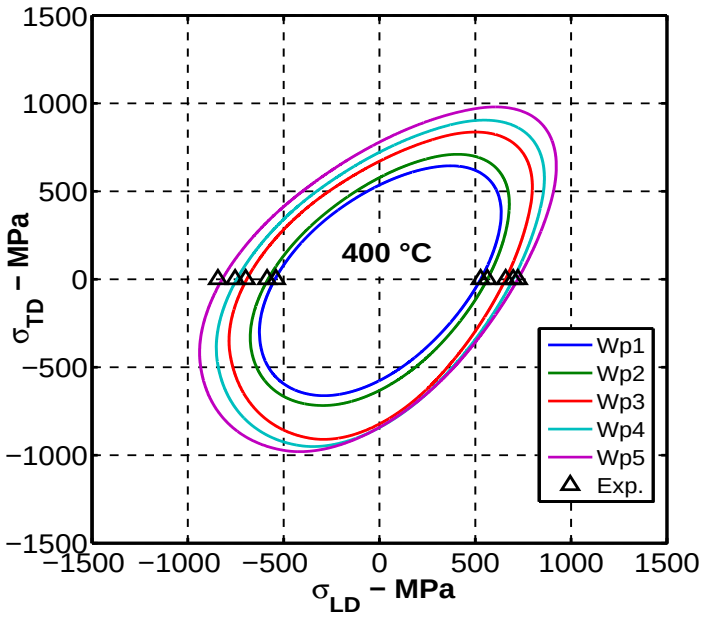

(c)

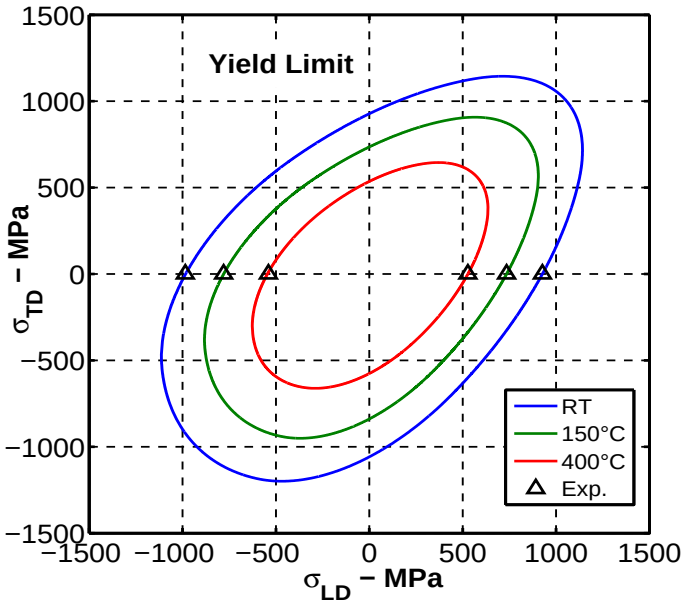

(d)

Figure 5.7. CPB06 yield surfaces for five *Wp* (a) at RT, (b) at 150 °C (c) at 400 °C. (d) Initial CPB06 yield surfaces at RT, 150 °C and 400 °C.

5.6. Assessment of predictions of the thermo–viscoplastic Norton–Hoff model and the orthotropic yield criterion CPB06

5.6. Assessment of predictions of the thermo–viscoplastic Norton–Hoff model and the orthotropic yield criterion CPB06

Compression tests on elliptical cross–section specimens and tensile tests on holed and V–notch specimens with geometries presented in Fig. 5.8 are tested and compared with FE simulations in order to evaluate the two identified models.

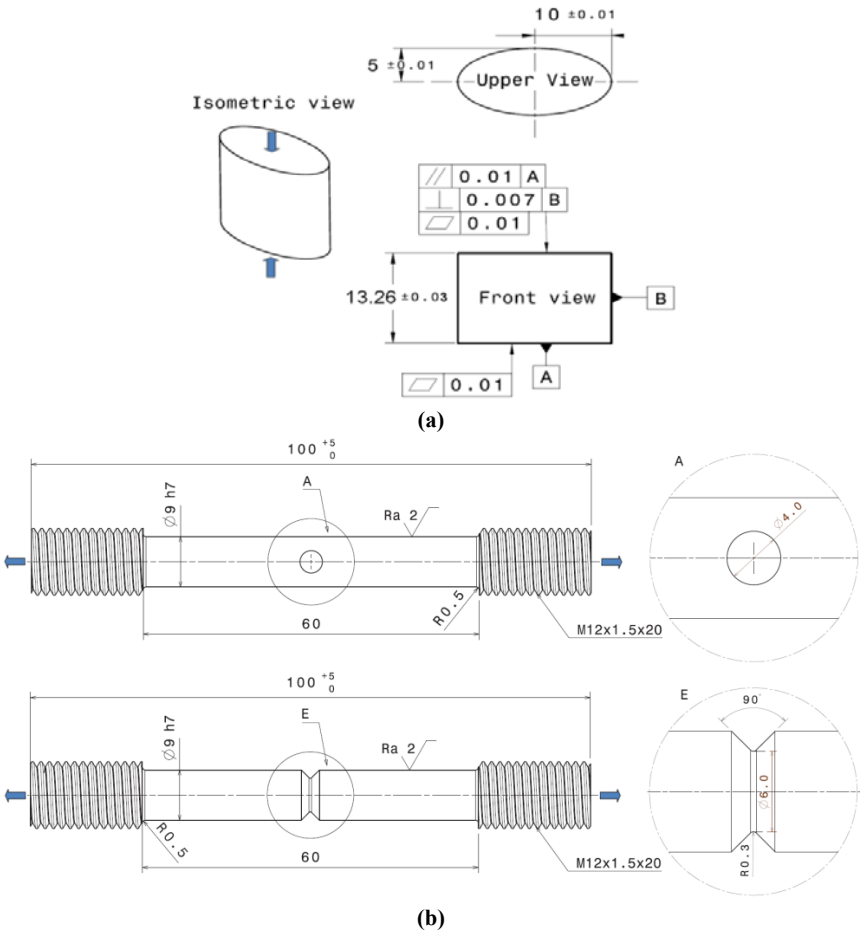

Figure 5.8. Geometries and dimensions of the specimens chosen for the evaluation of the models: (a) compression and (b) tensile specimens with axial load in LD direction.

One–eighth of the specimens are meshed. The updated Lagrangian FE code Lagamine is chosen and the thermomechanical mixed solid finite element BLZ3T (Li and Cescotto, 1997) is used for simulation with the Norton Hoff constitutive law. The latter is based on an implicit integration scheme (Habraken et al. 1998). BWD3D finite element is used for the simulations with CPB06 law. Both finite elements are 8–node 3D brick elements with a mixed formulation adapted to large strains and large displacements. They use a reduced integration scheme (with only one integration point) and an hourglass control technique. These elements are based on the non–linear three–field (stress, strain and displacement) HU–WASHIZU variational principle (Belytschko and Bindeman, 1991, Duchêne et al., 2007, Simo and Hughes, 1986).

The experimental and predicted axial load and displacement curves are used to assess the predictions of the models.

5.6.1. Mesh sensitivity analysis

In order to verify the accuracy of the FE simulations with the identified constitutive laws, the NH and the CPB06 simulations are applied on a tensile test on a V–notch round bar. A sensitivity evaluation of the mesh density of the predicted cross–sectional areas is performed just before the experimental fracture. This geometry is chosen as it presents stress concentration at the sharp edge. Four meshes are used with a progressive increase in the number of elements along the three orthogonal directions of the sample Fig. 5.9(a). The results show a low influence of the mesh density on the computation of the cross–sectional area (Fig. 5.9(b)). This low sensitivity was expected, as the global variation of the plastic behavior of the entire cross–section with the mesh density is affected by a very localized variation of the behavior on the sharp edge. Despite this low sensitivity, the measured cross–sectional area is found higher than the predicted ones. Similar phenomenon in tensile tests on U–notch round bar was presented in Chapter 4, and it could be explained by the volume conservation assumption used in the plasticity models and the neglect of the porosity of the material. The void volume fraction of 0.57% is present in the material just before fracture in a uniaxial tensile test (see Lecarme, 2013) when error of volume of 0.75% is computed in the cross–section. Another reason could be also related to a necking event predicted too early. For each model, a different

reason could be responsible: isotropic–visco–plastic NH model presents a too low strength because it neglects anisotropy behavior (see Fig. 5.12), when the natural regularization brought by viscosity and delaying necking is missing in elastoplastic Cazacu model. Finally, a fine mesh density (18 elements along the radius of the minimal cross–section of the V–notch round bar) is chosen as a compromise between good numerical accuracy and CPU time efficiency of the simulations.

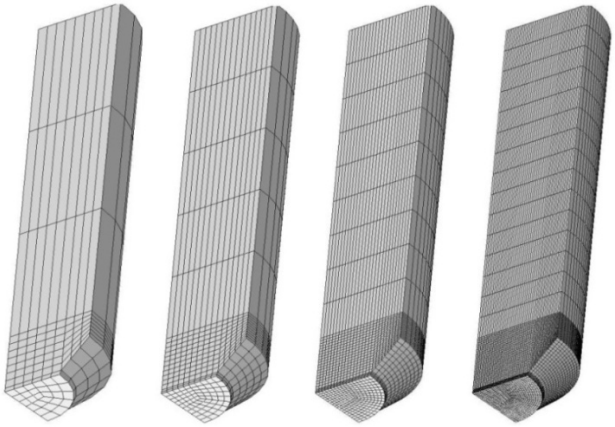

(a)

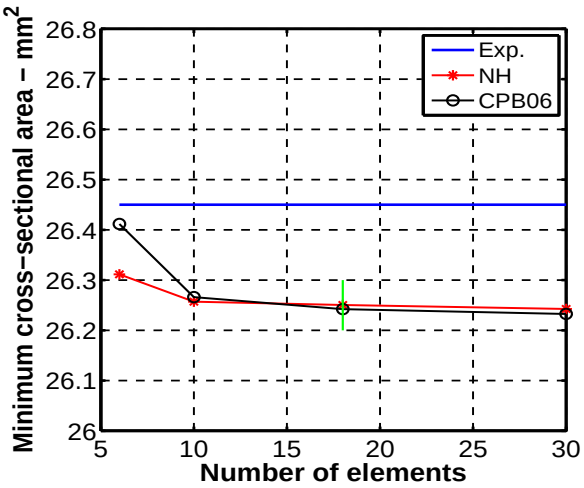

(b)

Figure 5.9. Mesh sensitivity analysis. (a) V–notch round bars meshed with 6, 10, 18 and 30 elements along the radius (b) Evolution of the predicted minimum cross–sectional area with the number of elements along the radio (experimental error equal to +–0.05 mm).

5.6.2.Load predictions

5.6.2.1. Tensile tests

The tensile tests are performed on the two geometries shown in Fig. 5.8(b) until fracture at RT, 150 °C and 400 °C. Figs. 5.10–5.11 show the evolution of the load with the axial displacement of a gauge length of the specimen equal to 40 mm for the tests performed at RT and 60 mm for the tests at 150 °C and 400 °C. The experimental curves are presented as the average of three tests with the respective error bars. The large error bars represent the tensile fracture zone. The linear elastic increment of the load with the axial displacement is well predicted for all the simulations. Such a result allows validating the Young's modulus indentified at several temperatures in LD direction by using simple tensile tests.

Eq. 5.7 is used in order to quantify the accuracy of the load predictions $\left(F^{\text{model}}\right)$ of both models compared with experimental data $\left(F^{\text{exp}}\right)$ at several fixed values of axial displacements (i) equal to multiples of 0.2 mm (m is the total number of values used in each curve)..

$$\text{Error} = \frac{1}{m}\sum_{i=1}^{m}\frac{\left|F_i^{\text{exp}} - F_i^{\text{model}}\right|}{F_i^{\text{exp}}} \tag{5.7}$$

The axial load predictions in the plastic zone for the V–notch round bars shown in Fig. 5.10 are overestimated by the NH model at the three temperatures suggesting a too high hardening extrapolated curve. Better load correlations are obtained from simulations using CPB06 model with an error lower than 3.6% at RT and 150 °C. The CPB06 predictions are very accurate at 400 °C with an error equal to 1.2%. It should be considered that the CPB06 model identification is different at RT than the ones at 150 °C and 400 °C. The latter were performed with only tensile and compression tests in one direction of the material, while the CPB06 yield criterion at RT was identified with stress–strain data in the three orthogonal directions of the material for tensile and compression tests and in one direction for simple shear and plane strain tests (Fig. 5.12). Even though error predictions by CPB06 are low, they could still be reduced to smaller values. The errors at the beginning of the plastic zone are attributed to the purely empirical bases

of the material models and the fact that the stress state in the V–notch is far from the stress states included in the identification of the models.

The axial load predictions from the tensile test of round bars with a central hole by the two models are more accurate than the ones for V–notch for all the temperature range investigated (Fig. 5.11). This could be attributed to the closer stress state in the specimen to uniaxial stress state used in the identification of both models. However, a slight decrease of the predicted load before fracture found with both models does not represent the feature experimentally observed. This effect could be attributed to the identification of the strain hardening law (NH) and yield surfaces (CPB06) which are performed with true stress–strain curves till strain value equal to 0.1 (before the onset of necking in simple tensile tests), and the fact that the strain reached in the minimal cross–section of the specimen with central hole is much higher (maximum strain value equal to 0.33), so the real hardening after the axial strain equal to 0.1 is unknown and assumed to follow the constitutive hardening law of the model.

For the last part of the load–displacement curves, the sudden decrease of the experimental load is attributed to a damage of the material which is not taken into account by the studied models.

As a conclusion, the gap between the experimental results and the simulations in tensile tests with V–notch and central hole at RT and 150 °C could be explained by the fact that the stress states in the V–notch and O–holed are far from the ones used in the identification of the constitutive laws, specially for V–notch. Inverse modeling for instance could be applied for this purpose. Also, it can be seen from Fig. 5.12 that the initial shear yield stress was overestimated in the identification of CPB06 and NH (von Mises yield locus) models at RT. This overestimation increases the axial load in notch round bars as demonstrated Chapter 5. However, the maximum error on the load prediction with CPB06 is low (around 3% for round bar with central hole and less than 3.6% for V–notch).

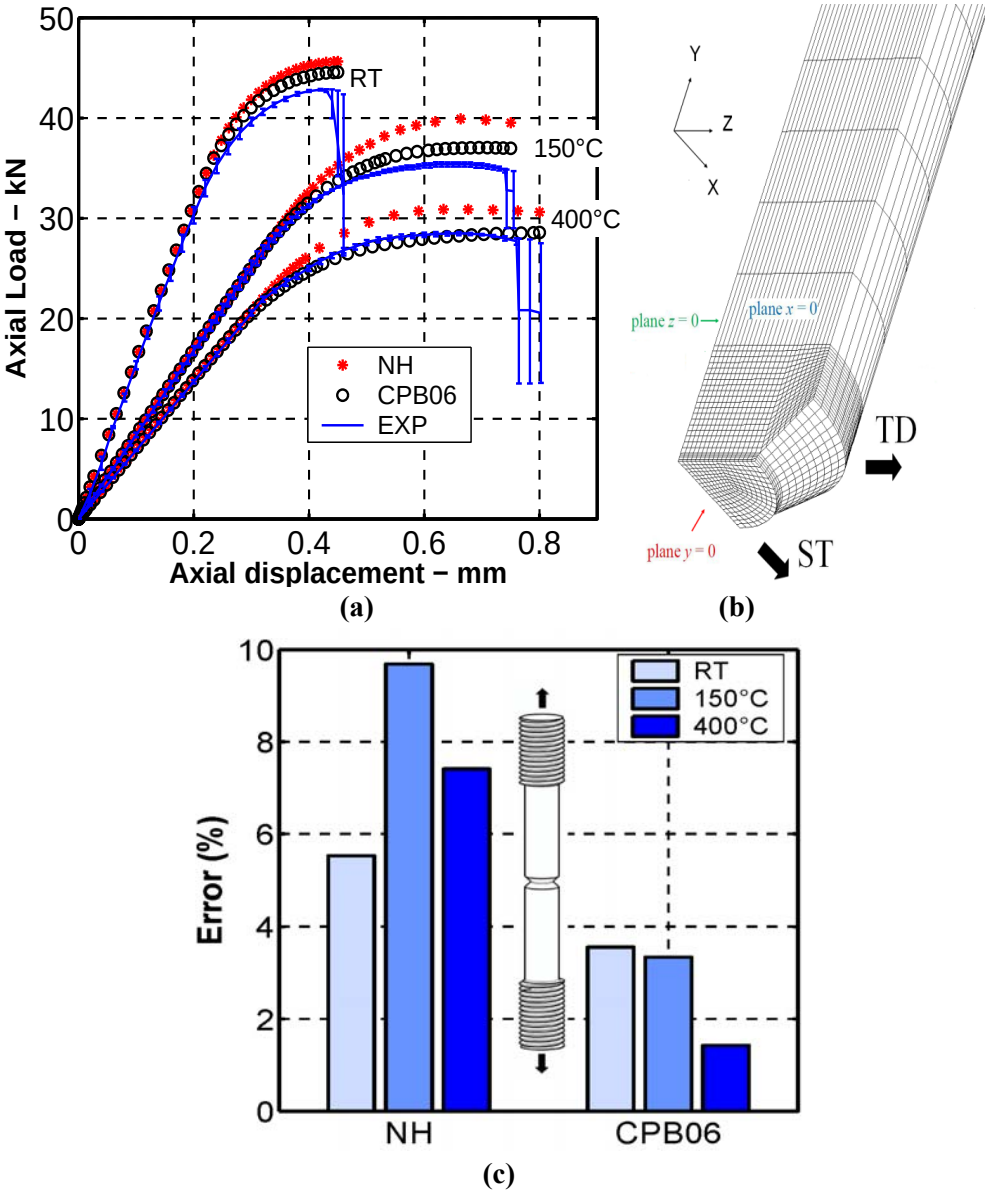

Figure 5.10. (a) Axial load predictions (LD direction) of the identified Norton–Hoff and CPB06 models applied to tensile tests on round bars with V–Notch. The gauge length for test performed at 150 °C and 400° is 60 mm and for tests at RT is 40 mm. Experimental curves are shown with the error bar. (b) Mesh of the one–eighth of the specimen. (c) Percentage error on the load prediction.

5.6. Assessment of predictions of the thermo−viscoplastic Norton–Hoff model and the orthotropic yield criterion CPB06

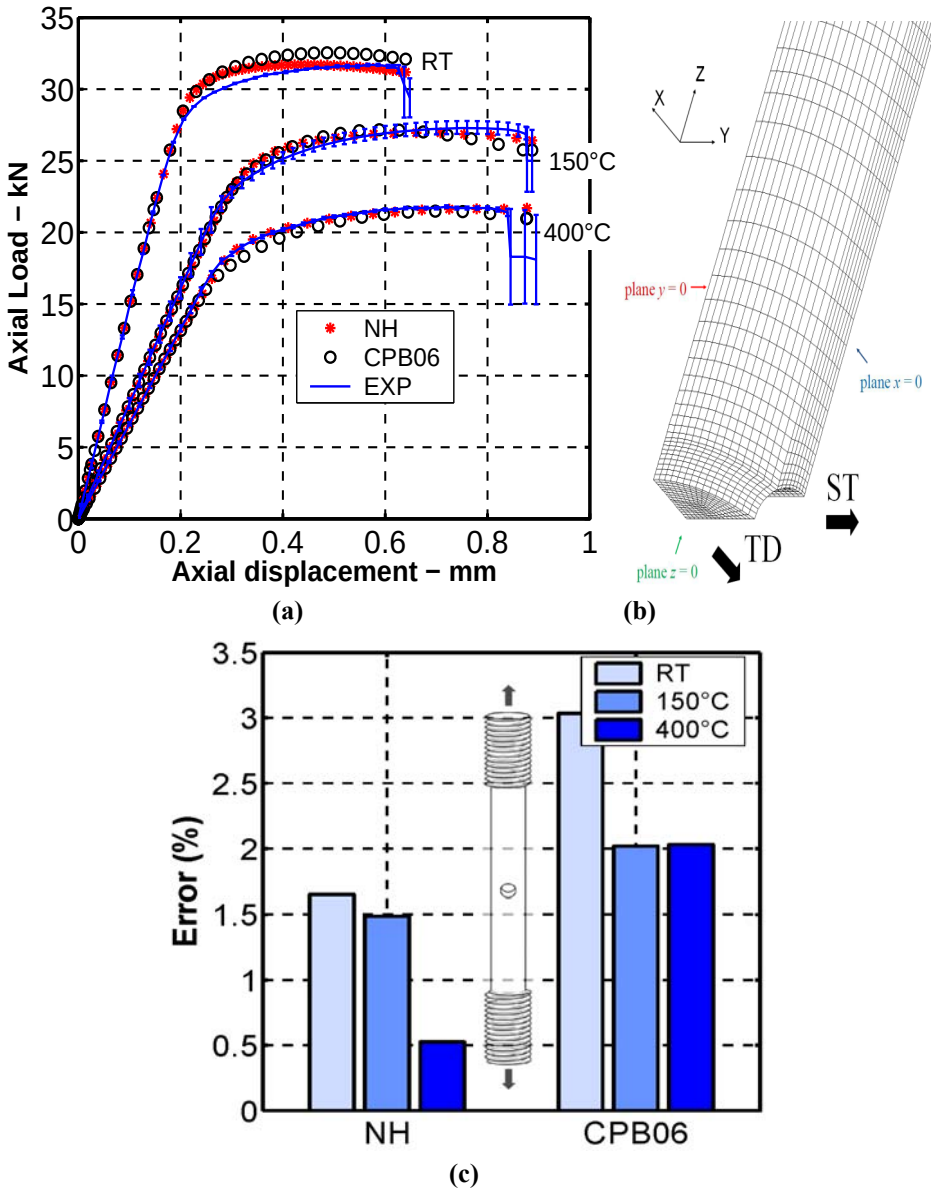

Figure 5.11. Axial (LD) Load predictions of the identified Norton–Hoff and CPB06 models applied to tensile tests on bars with a central hole. The gauge length for test performed at 150 °C and 400° is 60 mm and for tests at RT is 40 mm. (b) Mesh of the one–eighth of the specimen. (c) Percentage error on the load prediction.

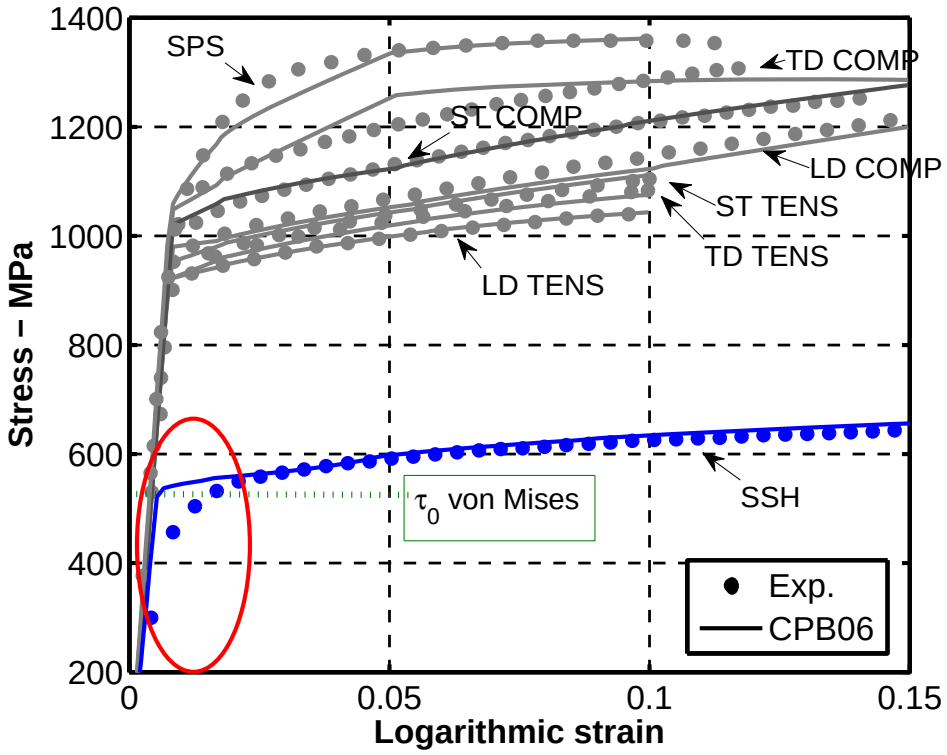

Figure 5.12. Experimental (Exp.) and CPB06 predictions of stress–strain curves in tension (TENS) and in compression (COMP) for the LD, TD and ST directions, plane strain LD–ST (SPS) and shear (SSH) LD–ST at RT.

5.6.2.2. Compression tests

The compression tests are performed on specimens shown in Fig. 5.8(a) until 16% of average axial strain. These tests are performed at three different strain rates (10^{-3}, 10^{-2} and 10^{-1} s^{-1}) for RT and at one strain rate equal to 10^{-3} s^{-1} for 150 °C and 400 °C. Fig. 5.13(a) shows the axial load versus axial displacement of the compression specimens with elliptical cross–sections and Fig. 5.13(b) assesses simulation results versus experiments.. The variation of the compressive load with the strain rate is not well predicted by NH model, nor of course by the CPB06 model (Fig. 5.13(a)). Even though NH takes into account the strain rate sensitivity of TA6V, the predicted load with this model is much lower than the ones

obtained by the experiments, and the one obtained with the CPB06 model. The latter model provides a more accurate load computation insensitive to strain rate than the NH model (Fig. 5.13b, Eq. 5.7). This can be explained by the fact that the tension–compression strength asymmetry observed in the TA6V is only taken into account by the CPB06 model. The same conclusion is obtained from the observation between the predicted and experimental compressive loads on tests at several temperatures (Fig. 5.13(d)), where CPB06 presents a high accuracy load prediction (Fig. 5.13(e)).

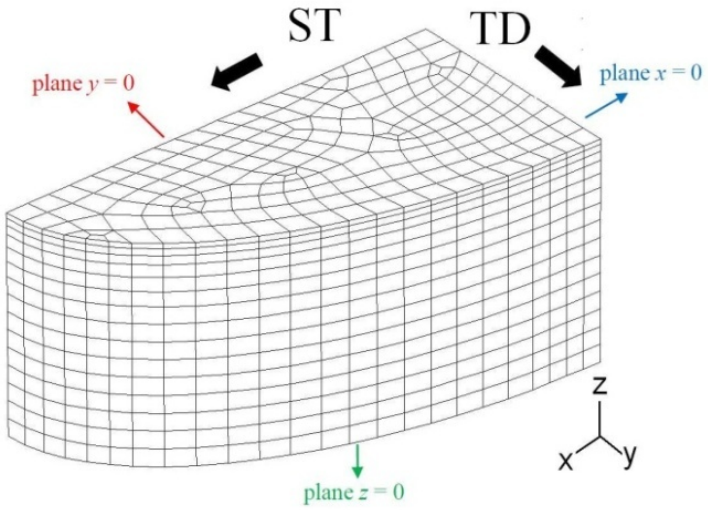

(a)

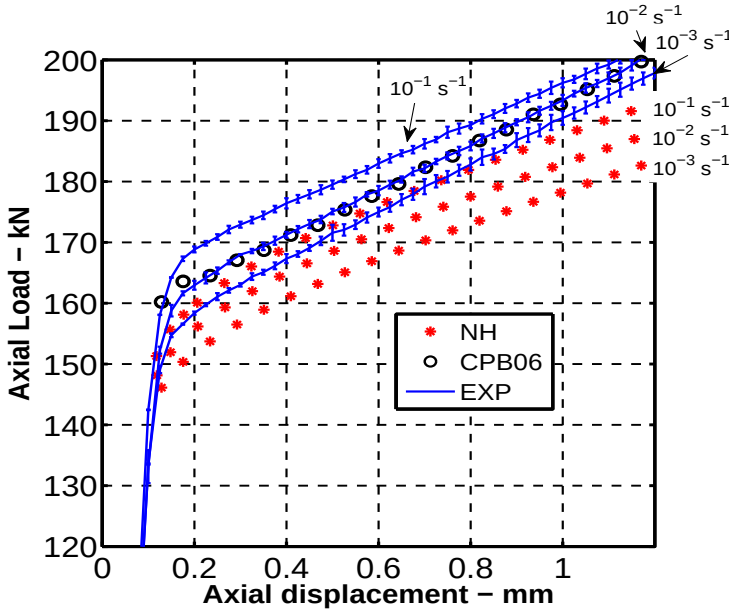
10^{-2} s^{-1}
10^{-3} s^{-1}
10^{-1} s^{-1}
10^{-1} s^{-1}
10^{-2} s^{-1}
10^{-3} s^{-1}
NH
CPB06
EXP
Axial Load – kN
Axial displacement – mm
200
190
180
170
160
150
140
130
120
0
0.2
0.4
0.6
0.8
1

(b)

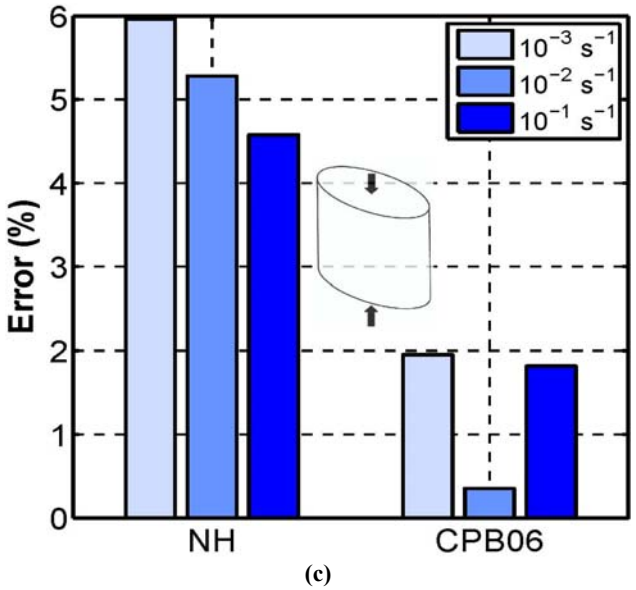
10^{-3} s^{-1}
10^{-2} s^{-1}
10^{-1} s^{-1}
Error (%)
NH
CPB06
6
5
4
3
2
1
0

(c)

5.6. Assessment of predictions of the thermo−viscoplastic Norton–Hoff model and the orthotropic yield criterion CPB06

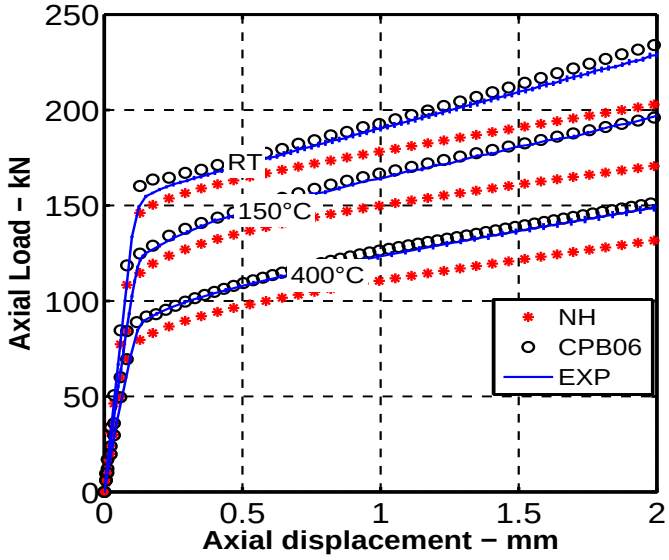

(d)

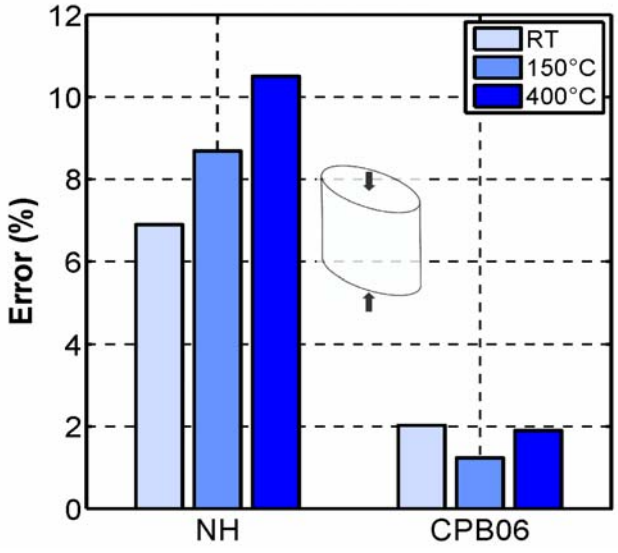

(e)

Figure 5.13. Axial (LD) load predictions of the identified Norton–Hoff and CPB06 models applied to compression tests on elliptical cross–section (a) mesh of the one–eighth of the compression specimen (b) Compression tests at RT and three strain rates equals to 10^{-3}, 10^{-2} and 10^{-1} s^{-1} and the (c) Percentage error on the load prediction. The initial height of the specimen is equal to 13.25 mm. (d) Compression tests at RT, 150 °C and 400 °C and at 10^{-3} s^{-1} with the (e) Percentage error on the load prediction.

5.6.3. Shape predictions

5.6.3.1. O–Holed bar tensile test

The use of 3D–DIC allows obtaining the entire experimental strain and displacement fields of the tested samples with accurate results. Fig. 5.14 shows the evolution of the true axial strain field and geometry measured on the tensile round bar with a central hole at RT.

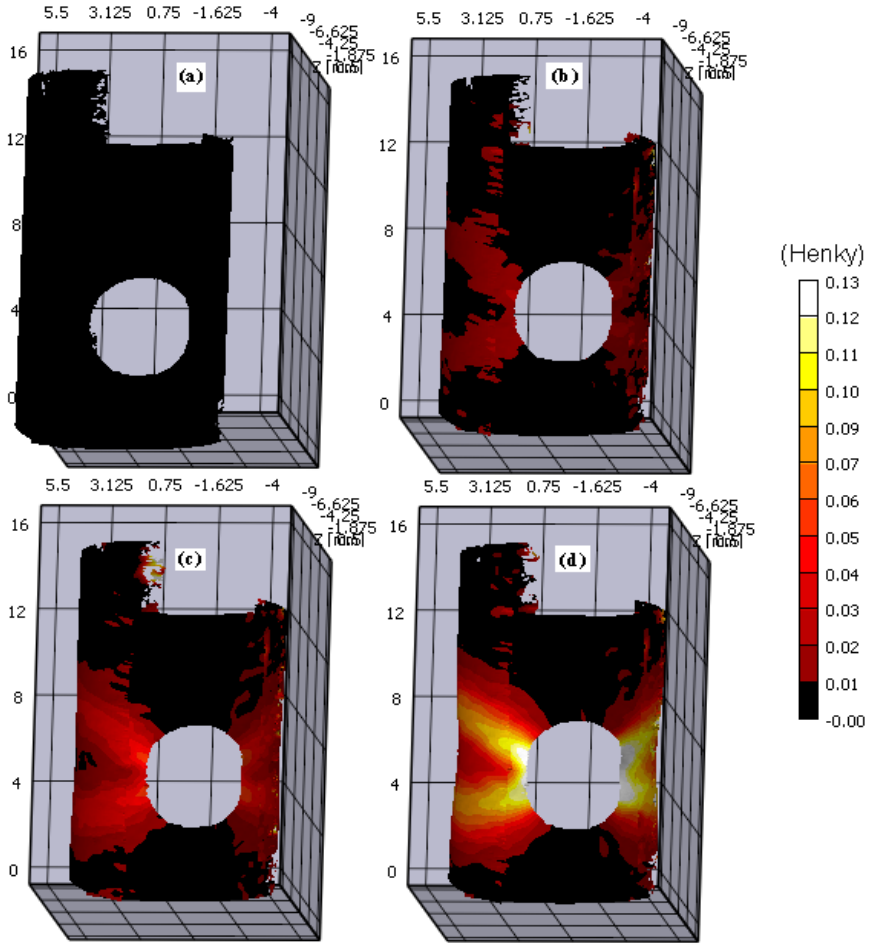

Figure 5.14. Evolution of the true axial strain field and geometry of the specimen with central hole measured by 3D–DIC. (a) Initial measurements of the specimen without load, (b) at 0.2 mm and (c) 0.4 mm of axial displacement (gauge length=40 mm), (d) and right before the fracture.

5.6. Assessment of predictions of the thermo−viscoplastic Norton–Hoff model and the orthotropic yield criterion CPB06

The predictions of the evolution of necking (diameter D, Fig. 5.15(b)) with the experimental value until rupture are compared in Fig. 5.15(a). NH model largely underestimates the value of D and the anisotropic CPB06 model shows closer predictions to the experimental values in the entire loading range.

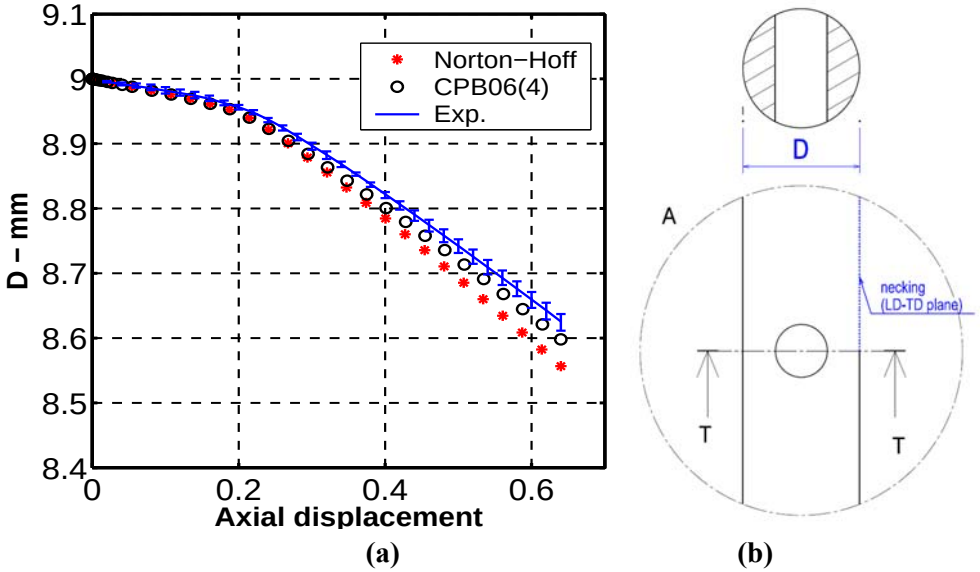

Figure 5.15. (a) Comparison between DIC measurements, CPB06 and Norton–Hoff law predictions of the (b) diameter D of the cross–section of the central holed specimen.

5.6.3.2. Compression test

The compression tests performed at 10^{-3} s^{-1} and at RT is also used to assess the shape predictions of the models. The evolution of the lengths of the minor (2b) and major (2a) axes of the elliptical cross–section of the specimens are shown in Fig. 5.16. Both models closely predict the major axis length but the viscoplastic Norton–Hoff results neglecting anisotropy differ more and more from the experimental value of the minor axis length with the increase of the loading. The latter isotropic model cannot simulate the true anisotropic plastic flow.

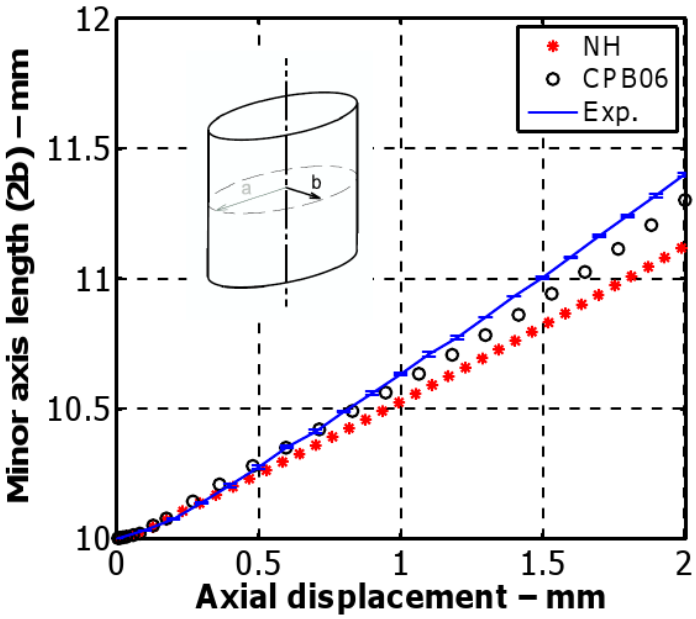

(a)

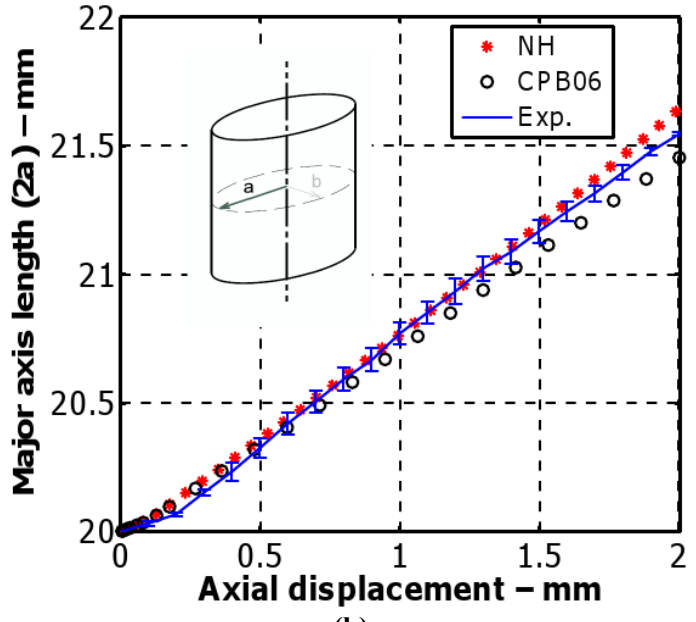

(b)

Figure 5.16. Comparison between DIC measurements, CPB06 and Norton–Hoff law predictions of minor (a) and major (b) axis length of the elliptical cross–section of compression sample loaded in LD direction.

5.7. Conclusions and perspectives

The mechanical response of TA6V was studied with a set of tension and compression tests performed at moderate temperatures up to 400 °C and a range of strain rates between 10^{-3} and 10^{-1} s^{-1}. Mechanical properties such as yield stress, strain hardening, strain rate hardening, strength differential effect and their evolution with the temperature were determined. The influence of the temperature on these properties was found to be higher than the one of the strain rate. Furthermore, the experimental data were used for the identification of the material parameters of CPB06 and Norton–Hoff constitutive laws at RT, 150 °C and 400 °C.

The following points are the main findings regarding the assessment of both models to predict the load and displacements on specimens with several initial stress triaxialities:

- NH model accurately fits the experimental strain and strain rate hardening of monotonic tests TA6V only for the type of loading and material direction used for its identification (in this case, uniaxial tensile in LD direction). This is due to the fact that the model takes into account neither the SD effect nor the anisotropic behavior of the alloy.

- The CPB06 model results show a better experimental correlation than the NH model predictions, for all the range of temperatures investigated. It is attributed to the ability of the model to capture the SD effect and distortion of the anisotropic yield surface of the TA6V. However, this model does not take into account the change of yield surface with the strain rate. Its accuracy is limited to the strain rate range chosen for its identification and depends on the strain rate sensitivity of the alloy.

- The maximum and global average Error values in load prediction on all the validation tensile tests were found to be equal to 3.6% and 2.0 % for the CPB06 model, while for the NH model, these errors were equal to 10.4% and 5.6%.

- The shape of the specimens used for the validation tests at RT were also compared with the predictions of the plasticity models:
    - In compression tests on elliptical cross–section specimens, the CPB06 model predicts more accurately the evolution of the shape with a maximum deviation of displacements equal to 0.1 mm in the minor axis length compared to 0.2 mm for the one obtained with the NH model.
    - In the tensile test of round bars with a central hole, good correlations of the evolution of the necking were obtained with the CPB06 model with a maximum deviation of 0.015 mm compared to 0.05 mm obtained with the NH model.

Finally, based on the extensive experimental and numerical analysis, one concludes that the CPB06 model proposed by Cazacu et al. (2006) shows a good and higher accuracy when predicting shape and load on complex specimens of TA6V (several initial triaxilities with axial and radial load, e.g. V–notch, central holed round bars, compression with barreling, etc) than the Norton–Hoff law. If one has no access to an elasto–visco–plastic anisotropic model, it seems better to neglect viscosity than anisotropy for low strain rates..

5.8. References

Arrieta, H.V., Espinosa, H.D., 2001. The role of thermal activation on dynamic stress–induced inelasticity and damage in Ti–6Al–4V. Mechanics of Materials 33, 573–591.

Belytschko, T., and Bindeman, L.P., 1991. Assumed Strain Stabilization of the 4–Node Quadrilateral with 1–Point Quadrature for Nonlinear Problems. Computer Methods in Applied Mechanics and Engineering 88, 311–340.

Bron, F. and Besson, J., 2004, A yield function for anisotropic materials. Application to aluminium alloys. Int. J. Plasticity 20, 937–963.

Burkins, M., Hansen, J., Paige, J., Turner, P., 2000. The effect of thermomechanical processing on the ballistic limit velocity of extra low

5.8. References

interstitial titanium alloy Ti–6Al–4V. U.S. Army research laboratory ARL–MR–486, 1–69.

Burkins, M., Wells, M., Fanning, J., Roopchand, B., 2001. The Mechanical and Ballistic Properties of an Electron Beam Single Melt of Ti–6Al–4V Plate. U.S. Army Research Laboratory, ARL–MR–515.

Cazacu, O., Plunkett, B., Barlat, F., 2006. Orthotropic yield criterion for hexagonal close packed metals. Int. J. Plasticity 22, 1171–1194.

Duchêne, L., El Houdaigui, F., Habraken, A.M. 2007. Length changes and texture prediction during free end torsion test of copper bars with FEM and remeshing techniques. Int. J. Plasticity 23, 1417–1438.

Follansbee, P.S., Kocks, U.F., 1988. A constitutive description of the deformation of copper based on the use of the mechanical threshold. Acta Metallurgica 36, 81–93.

Gilles, G., Hammami, W., Libertiaux, V. Cazacu, O. Yoon, J.H., Kuwabara, T., Habraken, A.M., Duchêne, L. 2011. Experimental characterization and elasto–plastic modeling of the quasi–static mechanical response of TA–6 V at room temperature. Int. J. Solids Struct. 48, 1277–1289.

Habraken, A.M., Charles, J.F., Wegria, J., Cescotto, S., 1998. Dynamic recrystallization during zinc rolling. Int. J. Forming Processes 1, 1292–7775.

Hammami, W., Tirry, W., Coghe, F., Duchene, L., Delannay, L., Habraken, A.M., 2011. Ti6A14V anisotropy and texture evolution predictions using Multisite and self consistent crystal plasticity models. The 12th World Conference on Titanium Ti–2011.

Hastings, W.K., 1970. Monte Carlo sampling methods using Markov chains and their applications. Biometrika 57, 97–109.

Hill, R., 1987. Constitutive dual potentials in classical plasticity. J. Mech. Phys. Solids 35, 23–33.

Hoff, N. J., 1954. Approximate analysis of structures in the presence of moderately large creep deformations. Quarterly of Applied Mathematics 12, 49–55.

Johnson, G.R., Cook, W.H., 1983. A constitutive model and data for metals subjected to large strains, high strain rates and high, Proc. of the 7th International Symposium on Ballistics, 541–547.

Khan, A.S., Kazmi, R., Farroch, B., 2007. Multiaxial and non–proportional loading responses, anisotropy and modeling of Ti–6Al–4V titanium alloy over wide ranges of strain rates and temperatures. Int. J. Plasticity 23, 931–950.

Khan, A.S., Suh, Y.S., Kazmi, R., 2004. Quasi–static and dynamic loading responses and constitutive modeling of titanium alloys. Int. J. Plasticity 20, 2233–2248.

Khan, A.S., Yu, S., 2012a. Deformation induced anisotropic responses of Ti–6Al–4V alloy. Part I: Experiments. Int. J. Plasticity 38, 1–13.

Khan, A.S., Yu, S. Liu, H., 2012b. Deformation induced anisotropic responses of Ti–6Al–4V alloy Part II: A strain rate and temperature dependent anisotropic yield criterion. Int. J. Plasticity 38, 14–26.

Lecarme, L., 2013. Viscoplasticity damage and fracture of Ti–6Al–4V. PhD thesis. Université catholique de Louvain, Belgium.

Lee, W.S., Lin, M.T., 1997. The effects of strain rate and temperature on the compressive deformation behaviour of Ti–6A1–4V alloy. J. Materials Processing Technology 71, 235–246.

Lee, W.S., Lin, C.F., 1998. Plastic deformation and fracture behaviour of TA6V alloy loaded with high strain rate under various temperatures. Mater. Sci. Eng. A 241, 48–59.

Li, X. K., Cescotto, S., 1997. A mixed element method in gradient plasticity for pressure dependent materials and modelling of strain localization. Computer Methods in Applied Mechanics and Engineering 144, 287–305.

Majorell, A., Srivatsa, S., Picu, R.C, 2002. Mechanical behavior of TA6V at high and moderate temperatures – Part I: Experimental results. Mater. Sci. Eng. A 326, 297–305.

5.8. References

Metropolis, N., Rosenbluth, A.W., Rosenbluth, M.N., Teller, A.H., Teller, E., 1953. Equation of state calculations by fast computing machines. J. Chem. Phys 21, 1087–1092.

Meyer Jr., H., Kleponis, D., 2001. Modeling the high strain rate behavior of titanium undergoing ballistic impact and penetration. Int. J. Impact Eng. 26, 509–52.

Milani, A.S., Dabboussi, W., Nemes, J.A., Abeyaratne, R.C., 2009. An improved multi–objective identification of Johnson–Cook material parameters. Int. J. Impact Eng. 36, 294–302.

Nelder, J., Mead, R., 1965. A simplex method for function minimization. Computer Journal 7, 308–313.

Nixon, M.E., Cazacu, O., Lebensohn, R.A., 2010. Anisotropic response of high–purity α–titanium: experimental characterization and constitutive modeling. Int. J. Plasticity 26, 516–532.

Norton, F. H., 1929. The Creep of Steel at Hight Temperature, The McGraw–Hill, New York, USA.

Odenberger, E.L., Hertzman, J., Thilderkvist, P., Merklein, M., Kuppert, A., Stöhr, T., Lechler, J., Oldenburg, M., 2012. Thermo–mechanical sheet metal forming of aero engine components in Ti–6Al–4V – PART 1: Material characterisation. Int. J. Mater. Form., 1–12.

Pascon, F. 2D1/2 Thermal–Mechanical Model of Continuous Casting of Steel Using Finite Element Method. PhD thesis. Université de Liège, Belgium.

Peirs, J., Verleysen, P., Degrieck, J., Coghe, F., 2010. The use of hat–shaped specimens to study the high strain rate shear behaviour of Ti–6Al 4V Int. J. Impact Eng. 37, 703–714.

Peirs, J., 2012. Experimental characterisation and modelling of the dynamic behaviour of the titanium alloy Ti6Al4V. PhD thesis, Ghent University, Belgium.

Plunkett, B., Lebensohn, R.A., Cazacu, O., Barlat, F., 2006. Anisotropic yield function of hexagonal materials taking into account texture development and anisotropic hardening. Acta Mater. 54, 4159–4169.

Plunkett, B., Cazacu, O., Lebensohn, R.A., Barlat, F., 2007. Elastic–viscoplastic anisotropic modeling of textured metals and validation using the Taylor cylinder impact test. I. J. of Plasticity 23, 1001–1021.

Seo, S., Min, O., Yang, H., 2005. Constitutive equation for Ti–6Al–4V at high temperatures measured using the SHPB technique. Int. J. Impact Eng. 31, 735–754.

Simo, J.C., Hughes, T.J.R., 1986. On the variational foundations of assumed strain methods. J. Appl. Mech., ASME 53, 51–54.

Tuninetti, V., Gilles, G., Péron–Lührs, V. Habraken, A.M., 2012a. Compression Test for Metal Characterization using Digital Image Correlation and Inverse Modeling, Procedia IUTAM. 4, 206–214.

Tuninetti, V., Gilles, G., Milis, O., Lecarme, L., Habraken, A.M., 2012b. Compression test for plastic anisotropy characterization using optical full–field displacement measurement technique. Steel Res. Int. SE: 14th Int. Conf. Metal Forming 2012, 1239–1242.

Tuninetti, V., Gilles, G., Milis, O., Pardoen, T., Habraken, A.M. (under review). Anisotropy and tension–compression asymmetry predictions of the plastic response of bulk Ti–6Al–4V titanium alloy. Submitted to Int. J. Plasticity.

Tuninetti, V., Habraken, A.M., (2014). Impact of anisotropy and viscosity to model the mechanical behavior of Ti–6Al–4V alloy. Materials Science and Engineering: A, 605, 39–50.

Zhang, C., Li, X.q., Li, D.s., Jin, C.h., Xiao, J.j., 2012. Modelization and comparison of Norton–Hoff and Arrhenius constitutive laws to predict hot tensile behavior of Ti−6Al−4V alloy. Trans. Nonferrous Met. Soc. China 22: s457−s464.

5.8. References

Zerilli, F.J., Armstrong, R.W., 1987. Dislocation–mechanics–based constitutive relations for material dynamics calculations. Journal of Applied Physics 61, 1816–1825.

Chapter 6. General conclusions and perspectives

6.1. Conclusions

This thesis was focused on the identification of the mechanical behavior and more specifically the plastic behavior of TA6V alloy. The following experimental developments were performed in order to properly calibrate the constitutive laws representing the features observed in the alloy:

- A tool to obtain constant strain rate tests for compression and tension tests with universal testing machine. The importance of implementing this capability for the characterization of the TA6V alloy was also highlighted by comparing the error induced by performing tests at constant cross–die speed instead of constant strain rate.
- A methodology to perform tests with the optical full field displacement measurement technique and a new tool to automatically post–process the DIC data used for characterization and validation of constitutive laws.
- A novel experimental tool to accurately determine the cross–sections and the displacement/strain field evolution of the samples. This tool leads to a more accurate true stress–strain curves computation than conventional methods.
- A new elliptical cylinder specimen to investigate the behavior of bulk TA6V alloy. The use of the DIC technique easily provides accurate barreling profile used to compute Coulomb's friction coefficient by using inverse method

A numerical study of compression test on the proposed elliptical cross–section specimen including friction was performed. A sensitivity of the axial strain field to the plastic anisotropy was found. This feature was used in order to identify the CPB06 material parameters by using the inverse modeling of compression tests in the three directions of the material. The main advantage of this new identification method is that the number of compression tests is considerably reduced and the effect of plastic

6.1. Conclusions

anisotropy on the shape is separated from the friction. For instance, comparing to the identification method with the Lankford's coefficients, the friction between the dies and the specimen cannot be completely eliminated or determined.

The mechanical behavior of the Ti–6Al–4V alloy was experimentally investigated using, uniaxial compression, uniaxial tensile, simple shear and plane strain tests in three orthogonal material directions at RT and at one strain rate (10^{-3} s^{-1}). In addition, compression and tension behavior of the alloy was determined in one direction of the material at three temperatures (RT, 150 °C and 400 °C) and three strain rates (10^{-3} s^{-1}, 10^{-2} s^{-1} and 10^{-1} s^{-1}).

In a first step, the experimental results at RT and at low strain rate (10^{-3} s^{-1}) revealed distortion of the yield surface associated with the tension–compression asymmetry (SD effect) and the anisotropic hardening. The anisotropy in compression was more pronounced than in tension. These features were well captured by an elasto–plastic constitutive law based on the macroscopic orthotropic yield criterion CPB06 adapted to hcp metals. The validation of the criterion was carried out on notched round bars involving different initial stress triaxiality and on compression tests on elliptical cross–section specimens, both tests involving multiaxial strain fields and large deformations. The load displacement curves and displacement/strain fields measured by 3D–DIC were correlated to the predictions of the FE simulations. Different material parameter sets of the yield criterion were obtained depending on the sets of experimental data used in the identification. The assessment of these material parameter sets demonstrated that the results closer to experimental measurements are obtained with the set identified with the higher number of tests including the following:

- The yield locus shape evolution through interpolation between surfaces associated to different plastic work.
- The definition of identical shear behavior in the 3 orthogonal planes when only one experiment is available.
- The inverse identification of compression tests involving inhomogeneous strain fields due to the plastic anisotropy and friction.

In a second step, the experimental data obtained at moderate temperatures up to 400 °C and at a range of strain rates between 10^{-3} and 10^{-1} s^{-1} revealed:

- Strong effect of the temperature on the yield stress.
- A rapidly decrease of the stress level with the increase of the temperature for all the investigated strain rates.
- A linear increase of the yield stress with the strain rate at RT and 150 °C.
- A weak strain rate influence on the yield stress at 400 °C.
- The hardening rate is different in tension and in compression (SD effect) and it varies with the temperature.
- Weak SD effect at 400 °C.

These data were used to identify two models:

1. Isotropic thermo–elasto–viscoplastic approach based on the Norton–Hoff (NH) viscoplastic constitutive law with isotropic von Mises yield locus.
2. Anisotropic thermo–elastoplastic approach based on the orthotropic yield criterion proposed by Cazacu et al., 2006 (CPB06).

The NH model accurately fitted the experimental strain and strain rate hardening of monotonic tests on TA6V, but only for the type of loading and material direction used for its identification (in this case, uniaxial tensile in LD direction). This result is due to the fact that the model takes into account neither the SD effect nor the anisotropic behavior of the alloy. On the other hand, the results obtained with the CPB06 model show a better experimental correlation than the NH model predictions, for all the range of temperatures investigated. This observation is attributed to the ability of the CPB06 model to capture the SD effect and distortion of the anisotropic yield surface of the TA6V. However, this model does not take into account the change of yield surface with the strain rate. Due to this fact, its accuracy is limited to the strain rate range chosen for its identification, as well as to the strain rate sensitivity of the alloy. The predictions of both models were also assessed using the load–displacements curves and the evolution of the shape of complex specimens (several initial triaxilities with axial and radial load, e.g. V–notch, central holed round bars, compression with barreling, etc). One concludes that the CPB06 shows a good and higher accuracy on the

6.1. Conclusions

predictions of TA6V mechanical behavior than the NH model. If one has no access to an elasto–visco–plastic anisotropic model, it seems better to neglect viscosity than anisotropy for low strain rates.

6.2. Perspectives

The simplest version of Cazacu model with one linear transformation was used in this thesis. Nevertheless, increasing the number of transformations could provide even higher flexibility to the model (Gilles et al., 2011).

Future work must be performed in order to develop a constitutive model able to reproduce the evolution of the yield surface with strain rate, temperature, strain path changes and cyclic behavior as kinematic hardening was found significant (Appendix C of Chapter 4). This model could be identified at high strain rate range [$1s^{-1}$ to 10^{+3} s^{-1}] (Fig. 6.1) and high temperatures to be further applied to simulate the FBO in a turbojet, allowing a comparison and validation of the simplified currently used models.

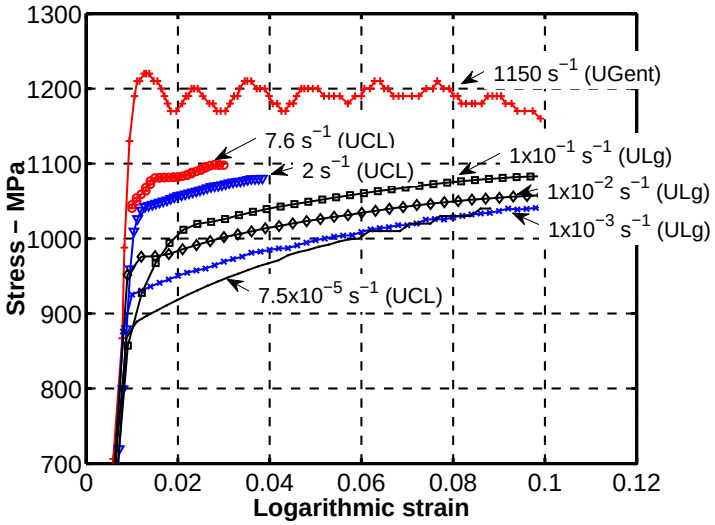

Figure 6.1. Tensile true stress-strain curves of TA6V (same batch) at LD direction and several strain rates. UCL results retrieved from Lecarme, 2013, UGent results from Peirs, 2012.

Furthermore, the effect of damage should be further investigated to predict fracture and an increased accuracy of the load and shape predictions even closer to the onset of fracture of TA6V components (Appendix D of this Chapter gather some porosity measurement results showing some discrepancy at fracture but a quite good agreement on the scale of initial porosity and on the fact that porosity is very localized near the fracture as demonstrated also by Clément, 2010). Extended Gurson model to anisotropic yield locus like the one developed by Ben Bettaïeb et al., 2011 could be tested, however, the strength differential effect will be neglected as long as this model relies on Hill yield locus. A more complex damage approach is indeed required. Nevertheless, the fact that the applied non-coupled damage approach was able to reproduce the loads and shapes near fracture seems to confirm the primal assumption that damage in this material has a slow development even after necking and increases very locally and quickly just before fracture. Although the model validations were done for specimens at the verge of failure, the fact that CPB06 provides reasonable predictions, gives an indication of the importance of correctly capturing the characteristics of the plastic flow.

Improvements regarding the experimental methods at elevated temperatures are suggested for further material identifications. Tensile test could be performed by using high temperatures extensometers (up to 1200 °C) inside the three-zone heating furnaces to acquire more accurate axial displacement measurements. The furnace should be adapted with side entry cut-out for the extensometers. Measurement data are transmitted from the specimen through the furnace to the extensometer via two light and flexible ceramic fiber cords. The reader could refer to http://www.epsilontech.com/ for features of the devices and to Mohamed et al., 2013, Uma Maheshwera Reddy Paturi, 2014, for applications examples.

A tool to obtain constant strain rate for compression and tension tests with universal testing machine was developed in this thesis in order to accurately determine the hardening response of the TA6V. For instance, compression tests performed at 150 °C and at a constant die speed targeting 10^{-3} s^{-1}showed 11% of stress error (10 MPa at 0.05 axial strain) comparing to the tests performed at a constant strain rate and identical temperature. Galán López, 2014 demonstrated that tests performed at constant sample temperature are also required for the accuracy of the stress. The temperature increase (due to heat generation) of the sheet TA6V tensile samples tested in

air (Fig. 6.2a) influences the stress hardening response due to the thermal softening (Fig. 6.2b). For instance, the maximum temperature increase at $8x10^{-5}$ s^{-1} is 1.8 °C. This leads a negligible error equal to 0.5% on the yield stress comparing to the stress obtained in a test performed at controlled temperature (in fluid). This observation obtained by Galán López, 2014 allows assuming that experiments performed at strain rates lower or equal to $8x10^{-5}$ s^{-1} can be considered as isothermal. Nevertheless, non-negligible stress error equal to 7% (15MPa at 0.05 of axial strain) was found for the tests performed at $6.7x10^{-4}$ s^{-1}. Therefore, not only constant strain rate must be guaranteed for accurate stress-strain curves but also isothermal conditions. The temperature controlled tests is suggested for future experimental tests on TA6V by using a refrigerator system that controls the temperature of a fluid (refrigerant) circulating in the surrounding of the sample.

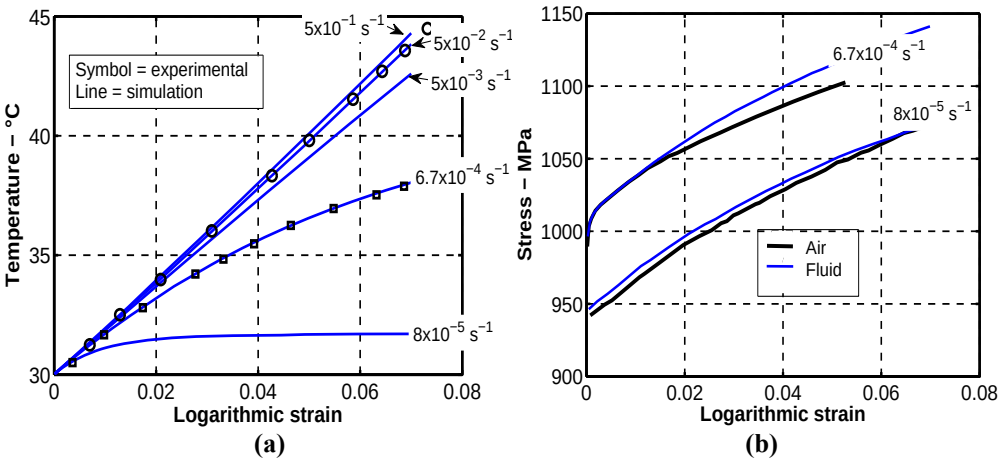

Figure 6.2. Experimental and numerical results (JC model) of tensile tests of sheet TA6V retrieved from Galán López, 2014 (a) Temperature increase of the samples during the tests. (b) Thermal softening observed in experimental true stress-strain curves of tests performed in air and in fluid.

DIC could also be applied in tension and compression tests at high temperature. In this case the furnace should be adapted with a window through its wall with the purpose of imaging the specimen surface. However, new difficulties than the ones discussed in this thesis appear. For instance, the image distortion produced by the window which has been reduced by using sapphire glass (Lyons at al., 1996). Correlation problems due to the

radiation of the sample are limited by using blue lights and optical passband filters (Bing Pan et al., 2010, 2012.). Other problems should be investigated, as paint ductility, paint adherence to the specimen and surface oxidation of the samples.

6.3. Appendix D. Measurements of porosity

Nucleation stage of voids seems an important event for TA6V damage prediction (Lecarme, 2013). The initial porosity on the TA6V alloy studied here is 0.003% according to ULg measurements obtained by optical microscopy and 0% obtained by microtomography (Lecarme, 2013). For a sheet TA6V alloy (Peirs, 2012), the initial porosity obtained by optical microscopy is 0.05%.

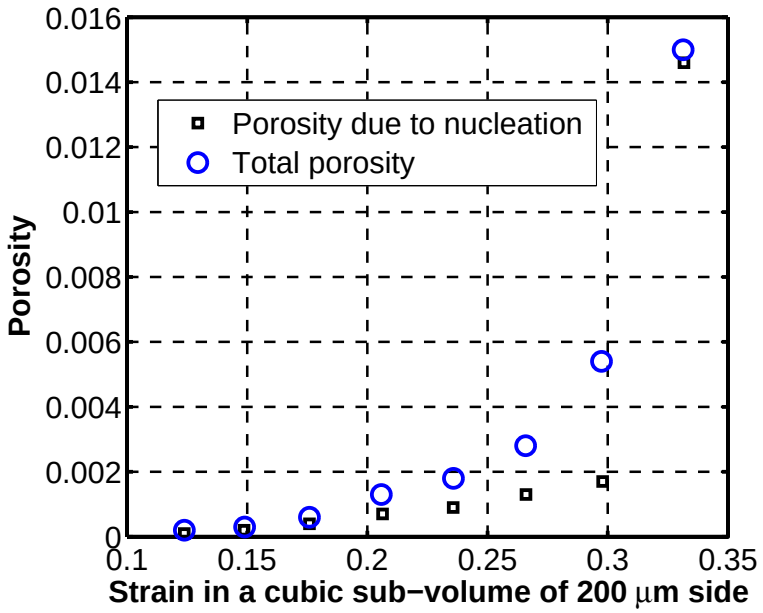

Figure D.1. Porosity fraction of notch specimen R1 measured in a cubic sub-volume (200μm side) by microtomography (Lecarme, 2013).

The information at fracture, gathered hereafter in ULg, underlines the difficulty to obtain reliable data as the accuracy strongly depends on the area concerned to define an average porosity. Porosity measurements at fracture are performed by polishing the longitudinal sections of fractured U-

6.3. Appendix D. Measurements of porosity

notch specimens (Figs. D.3 and D.4). The measurements were performed by H. Paydas (A&M Department, University of Liège) and statistical post-treatment scripts were developed by Bouffioux and Guzman (MS²F, ULg).

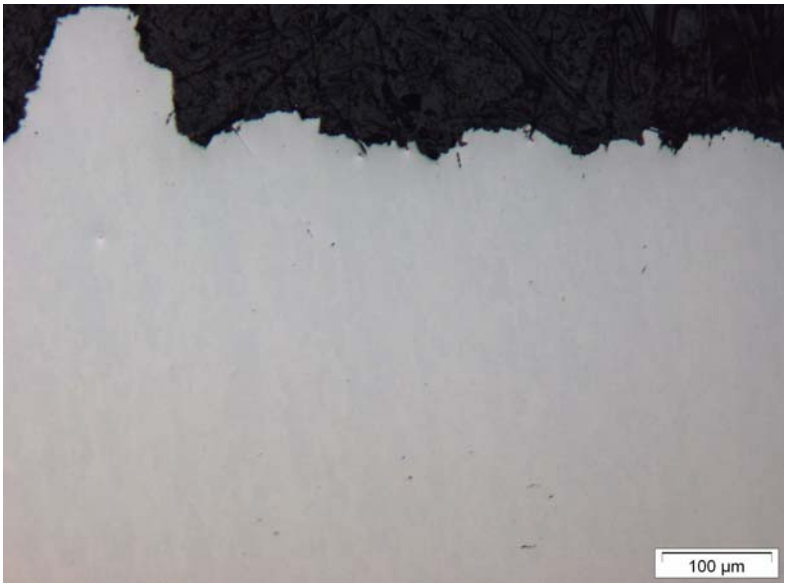

(a)

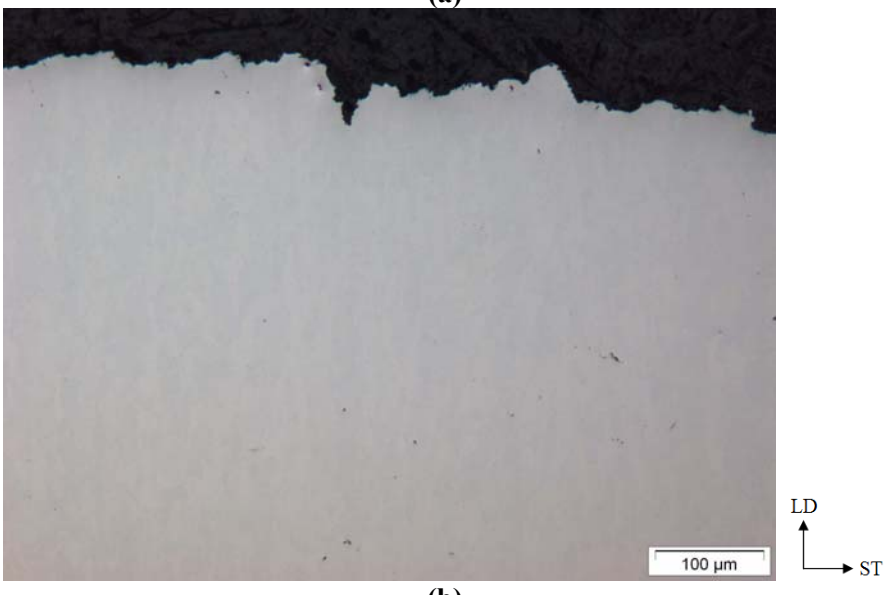

(b)

Figure D.3. Polished surface of specimen geometry R1.5 (Figure 4.9). Scattering is observed between sample identified as (a) ST2 and (b) ST3.

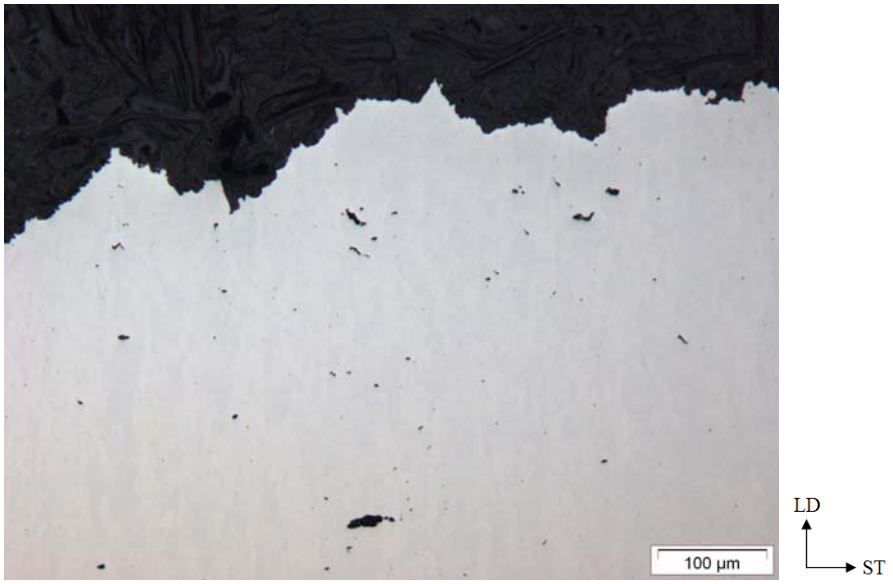

(a)

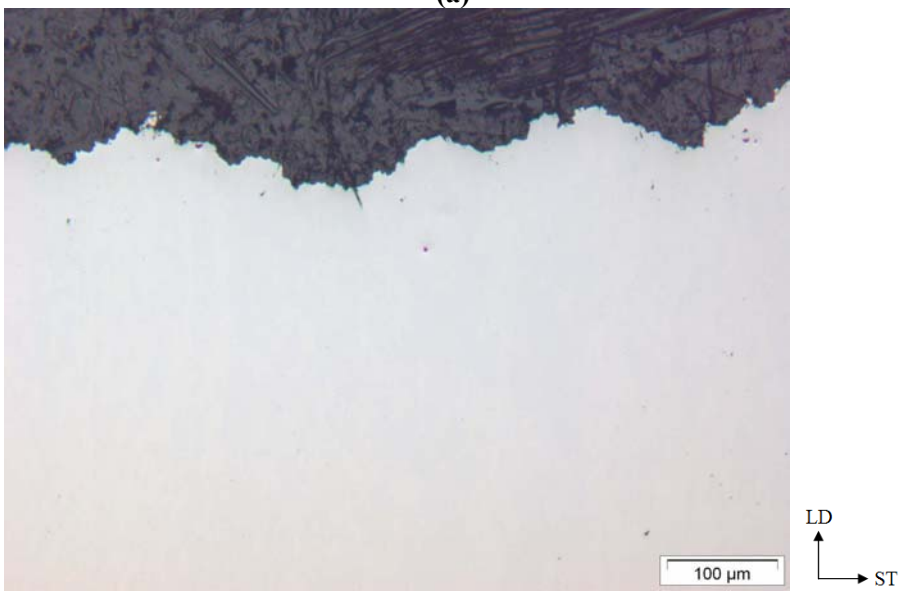

(b)

Figure D.4. Polished surface of specimen geometry R5 (Figure 4.9). Scattering is observed between sample identified as (a) ST10 and (b) ST12

6.3. Appendix D. Measurements of porosity

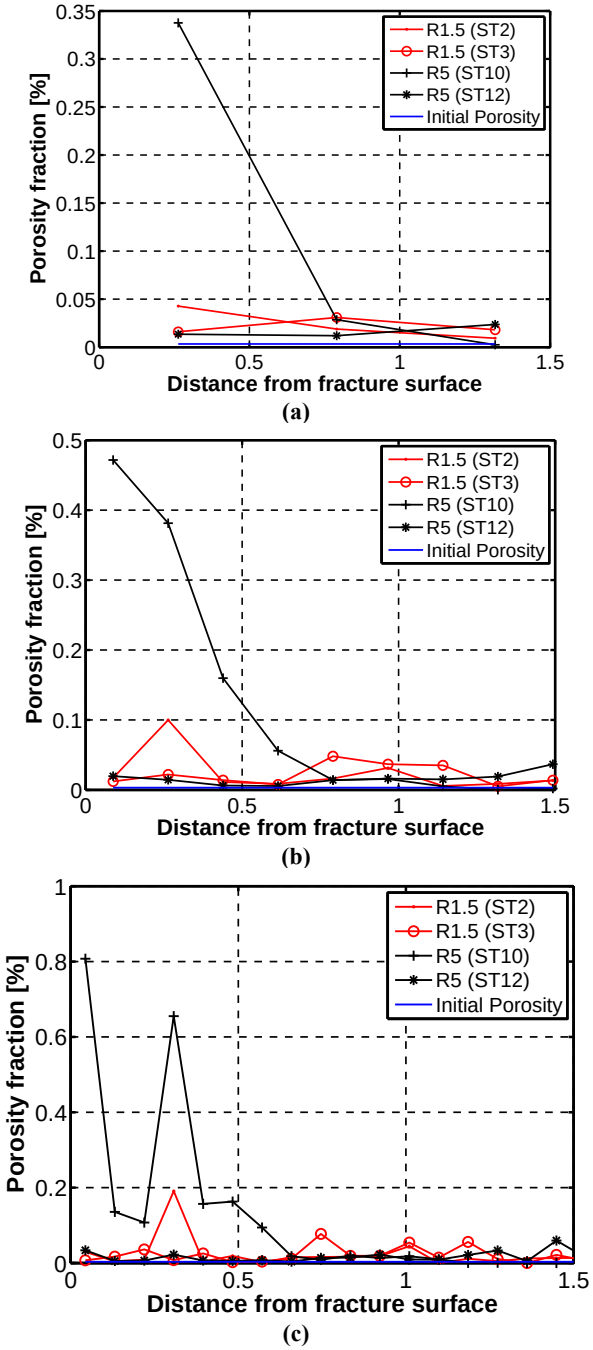

Figure D.5. Porosity fraction (%) results of measurements averages on layers of (a) 526µm, (b) 175µm and (c) 88µm.

In table D.1 the initial T_0 and final T_f values of triaxiality for R1.5 and R5 samples associated with Figure D.3(c) are defined. Table D.2. presents some data available in the literature. This small literature review on porosity level at rupture for TA6V show how difficult it is to get reliable measurements. Clearly further investigations are required to identify damage models on such data.

Table D.1. Porosity (volume fraction of voids) at fracture for notch specimens geometry R1.5 and R5 (Figure 4.9) aligned with the LD direction.

Tensile test	Initial triaxiality T_0	Triaxiality at fracture T_f	Porosity at fracture (layer 88μm) ± Std. Dev.
Notch R1.5	0.8	1.2	0.0002±0.0001
Notch R5	0.57	0.93	0.004±0.005

Table D.2. Porosity at fracture available in the literature.

Test	Initial triaxiality T_0	Triaxiality at fracture T_f	Porosity at fracture (layer 88μm)
Sheet tensile (Peirs, 2012)	0.33	-	0.006 to 0.007 (layer 25-50μm)
Round bar tensile (Peirs, 2012)	0.33	-	0.02
Notch R1 (Lecarme, 2013)	1	1.26	0.015 (cubic sub-volume 200μm side)

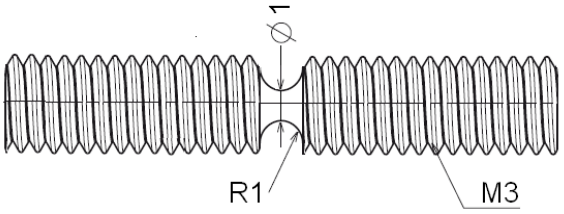

Figure D.2. Geometry of the Notch R1 (Lecarme, 2013) aligned with the TD direction.

6.4. References

Bing Pan, Dafang Wu, Yong Xia, 2010. High-temperature deformation field measurement by combining transient aerodynamic heating simulation system and reliability-guided digital image correlation. Optics and Lasers in Engineering 48, 841-848.

Bing Pan, Dafang Wu, and Liping Yu, 2012. Optimization of a three-dimensional digital image correlation system for deformation measurements in extreme environments, Applied Optics 51, 4409-4419.

Clément, N., 2010. Phase transformations and mechanical properties of the Ti-5553 beta-metastable titanium alloy. PhD thesis. Université catholique de Louvain, Belgium.

Galán López, J., 2014. Crystal plasticity based modelling of the strain rate dependent mechanical behaviour of Ti-6Al-4V. PhD thesis, Ghent University, Belgium.

Gilles, G., Hammami, W., Libertiaux, V., Cazacu, O., Yoon, J.H., Kuwabara, T., Habraken, A.M., Duchêne, L., 2011. Experimental characterization and elasto-plastic modeling of the quasi-static mechanical response of TA-6Al-4V at room temperature. International Journal of Solids and Structures 48, 1277-1289.

Lecarme, L., 2013. Viscoplasticity, damage and fracture of Ti–6Al–4V. PhD thesis. Université catholique de Louvain, Belgium.

Lyons, J. S., Liu, J. and Sutton, M.A., 1996. High-Temperature Deformation Measurements Using Digital-Image Correlation. Experimental Mechanics 36, 64-70.

Mohamed, A.M.A., Samuel, F.H., Saleh Al kahtani, 2013. Microstructure, tensile properties and fracture behavior of high temperature Al–Si–Mg–Cu cast alloys. Materials Science and Engineering: A 577, 64-72.

Uma Maheshwera Reddy Paturi, Suresh Kumar Reddy Narala, Rajdeep Singh Pundir, 2014. Constitutive flow stress formulation, model validation

and FE cutting simulation for AA7075-T6 aluminum alloy. Materials Science and Engineering: A 605, 176-185.

Peirs, J., 2012. Experimental characterisation and modelling of the dynamic behaviour of the titanium alloy Ti6Al4V. PhD thesis, Ghent University, Belgium.